

## Department of Precision and Microsystems Engineering

### Observations of the quasi-steady aerodynamic model of the Atalanta project for additional velocity conditions

Jayesh Balaji Kottiswaran

Report no : 2023.050  
Coach : Dr.ir. JFL (Hans) Goosen  
Professor : Dr.ir. JFL (Hans) Goosen  
Specialisation : PME  
Type of report : Master Thesis  
Date : 25/07/2023



---

# Observations of the quasi-steady aerodynamic model of the Atalanta project for additional velocity conditions

---

MASTER OF SCIENCE THESIS

For obtaining the degree of Master of Science in Mechanical Engineering at Delft  
University of Technology

*Submitted By:*

Jayesh Balaji Kottiswaran (5320062)

*Thesis Committee:*

Dr.ir. JFL (Hans) Goosen

Dr. Abel-John Buchner

July 25, 2023



# Acknowledgements

Working on this research topic was an arduous, yet fulfilling experience which involved a lot of challenges. It has been an unforgettable experience and I am incredibly grateful to all the people who made this journey possible. Their support and guidance have been of immense help to me in making this research work possible.

First and foremost, I extend my wholehearted gratitude to my supervisor Dr. ir. Hans Goosen, for his invaluable guidance and supervision. Being the only supervisor for my work, his contributions were of utmost importance for the completion of this work. His scientific attitude and broad knowledge of various topics made me comfortable approaching a multidisciplinary research question that required a lot of additional knowledge of aerodynamics. His constant presence and the regular meetings were vital in the smooth progress of this work for which I am forever grateful. Furthermore, I am thankful to Professor Abel-John Buchner for accepting the last-minute invite to be a part of my graduation committee.

I would like to express my gratitude to my parents and my brother for their never-ending moral support throughout my Masters program. Their support and well wishes were of great help that made me feel comfortable in tough situations. Finally, I would like to thank my friends for all their support and happy memories which were immense in completing this work and my Masters program.

I would like to conclude this section by mentioning a quote that resonated with me throughout this endeavor:

*"The important thing is not to stop questioning. Curiosity has its own reason for existing."*  
- Albert Einstein



# Abstract

This research work presents the observations of the updated quasi-steady aerodynamic model of the Atalanta project, a flapping wing Micro Air Vehicle (MAV) project, for additional velocity conditions. The main focus of this research work is to update the existing quasi-steady model of Q.Wang[1] developed for hovering conditions since its performance under additional velocity conditions remains unexplored. This work thus examines the influence of the additional velocities on the computed aerodynamic loads such as lift, drag, and also the influence on the passive pitching motion.

To incorporate the additional velocity into the quasi-steady model, the resultant translational velocity is computed by the vector addition of the kinematic velocity of the wing and the additional velocity. This is done by transforming the additional velocity in the inertial frame of reference to the co-rotating frame of reference, followed by the proper vector addition of the translational velocity components to compute the resultant translational velocity to be used in the aerodynamic load calculations.

Observations reveal that the generated aerodynamic lift and drag, and the passive pitching motion vary depending on the orientation and the magnitude of the additional velocity with respect to the kinematic motion of the wing, and that the significance of influence of the additional velocity magnitude depends on the flapping frequency and the elastic hinge stiffness. The results observed are analyzed to understand the influence of various additional velocity conditions on the computed aerodynamic loads and the passive pitching motion.

The updated model provides valuable insights into the behaviour of lift, drag, and passive pitching motion under various additional velocity conditions which can be used as a basis for approaching the solution of forward flight. These observations contribute to a better understanding of the aerodynamic quasi-steady model of the Atalanta project and pave the way for future research and experimental validation of the model.

Keywords: Aerodynamic quasi-steady model, Frame of reference, Lift, Drag, Passive pitching motion



# Contents

<b>1. Introduction to the Atalanta Project</b>	<b>1</b>
1.1. Inspiration from insects and flapping wing flight	1
1.2. Utilization of resonance	2
1.3. Introduction to Flapping wing Micro Air Vehicle (FwMAV)	2
1.4. Body and wing structure of Atalanta project	2
<b>2. Literature Review</b>	<b>5</b>
2.1. Aerodynamics of the Atalanta Project	5
2.1.1. Introduction to the aerodynamics of a flapping wing flight	5
2.1.2. Kinematic description of flapping wing stroke cycle	5
2.2. Quasi-steady aerodynamic model of Q. Wang <sup>[1]</sup>	8
2.2.1. Aerodynamic load equations and Passive Pitching Motion	9
2.2.2. Aerodynamic modelling of the wing using Blade element method	10
2.2.3. Validation of Q. Wang's quasi-steady aerodynamic model for hovering conditions	11
2.3. Changes required in using the same quasi-steady model for forward flight	12
2.3.1. Differences between hovering and forward flight	12
2.3.2. Major works on the changes in the quasi-steady model for forward flight conditions and their discussions	13
2.4. Conclusions from literature retrieval	13
2.5. Research Question	14
<b>3. In-depth understanding of Q. Wang's quasi-steady model</b>	<b>15</b>
3.1. Input Parameters and Kinematic motions	15
3.2. Angle of attack and aerodynamic load equations	15
3.2.1. Angle of attack	16
3.3. Center of pressure, and coefficients of lift, drag, and force	16
3.3.1. Translation-induced loads	17
3.3.2. Rotation-induced loads	17
3.3.3. Loads due to the coupling between translation and rotation of the wing	17
3.3.4. Added mass loads	18
3.4. Passive pitching motion	19
<b>4. Assumptions made while updating the quasi-steady model</b>	<b>21</b>
4.1. Same prescribed sweeping motion and no heaving motion	21
4.2. Wing root is fixed in the inertial frame of reference	21
4.3. Wing parameters used for the observations	22
<b>5. Updated quasi-steady aerodynamic model</b>	<b>23</b>
5.1. Explicit velocity terms in equations	23
5.2. Updating load equations for additional velocities	24
5.2.1. Updated translation-induced loads	24
5.2.2. Updated coupling-loads	25
5.2.3. Updated passive pitching function	26
5.2.4. Proper vector addition	26
5.3. Calculation of results at each strip along the wingspan	26
<b>6. Verification of the updated model</b>	<b>31</b>
6.1. Conformity with Q. Wang equations for hovering conditions	31
6.1.1. Zero additional velocity case	31
6.1.2. Very small magnitudes of additional velocities	33
6.2. Logical patterns of observed results	35

6.3. Verifying results with literature conclusions . . . . .	37
<b>7. Observations in additional velocity conditions</b>	<b>41</b>
7.1. Observations on average lift and drag produced . . . . .	42
7.2. Global peak lift and drag observations . . . . .	44
7.3. Observations on passive pitching motion changes . . . . .	47
7.4. Observations on the elastic hinge stiffness dependence . . . . .	49
7.5. Observations on the influence of flapping frequency . . . . .	52
7.6. Observations on translational force and translational velocities . . . . .	56
7.7. Observations along wingspan strips . . . . .	58
7.8. Observations on computational time . . . . .	59
<b>8. Discussions</b>	<b>61</b>
8.1. Discussions on the power calculations . . . . .	61
8.2. Discussions on optimal pitching axis . . . . .	62
<b>9. Conclusions and Recommendations</b>	<b>63</b>
9.1. Conclusions . . . . .	63
9.2. Limitations of the updated model . . . . .	64
9.3. Recommendations . . . . .	64
<b>A. Appendix</b>	<b>67</b>
A.1. Different ways to compute center of pressure, and coefficients of lift, drag, and force . . . . .	67
A.2. Global peak lift and drag graphs . . . . .	67
A.3. Passive pitching motion variation graphs . . . . .	72
A.4. Influence of elastic hinge stiffness graphs . . . . .	73
A.5. Influence of flapping frequency graphs . . . . .	75

# Abbreviations

<b>MAV</b> Micro Air Vehicle . . . . .	1
<b>UAV</b> Unmanned Air Vehicle . . . . .	1
<b>FwMAV</b> Flapping wing Micro Air Vehicle . . . . .	2
<b>LE</b> Leading Edge . . . . .	16
<b>TE</b> Trailing Edge . . . . .	16
<b>BEM</b> Blade Element Momentum . . . . .	8
$C_L$ Coefficient of Lift . . . . .	16
$C_D$ Coefficient of Drag . . . . .	16
$C_F$ Coefficient of Force . . . . .	16



# List of Symbols

Symbol	Quantity	Unit
$\phi$	Sweeping angle	rad
$\dot{\phi}$	Sweeping angular velocity	rad/s
$\ddot{\phi}$	Sweeping angular acceleration	rad/s <sup>2</sup>
$\theta$	Heaving angle	rad
$\dot{\theta}$	Heaving angular velocity	rad/s
$\ddot{\theta}$	Heaving angular acceleration	rad/s <sup>2</sup>
$\eta$	Pitching angle	rad
$\dot{\eta}$	Pitching angular velocity	rad/s
$\ddot{\eta}$	Pitching angular acceleration	rad/s <sup>2</sup>
$x_i$	Inertial frame x-axis	-
$y_i$	Inertial frame y-axis	-
$z_i$	Inertial frame z-axis	-
$x_c$	Co-rotating frame x-axis	-
$y_c$	Co-rotating frame y-axis	-
$z_c$	Co-rotating frame z-axis	-
$\omega_c$	Angular velocity in co-rotating frame	rad/s
$\alpha_c$	Angular acceleration in co-rotating frame	rad/s <sup>2</sup>
$v_c$	Translational velocity in co-rotating frame	m/s
$a_c$	Translational acceleration in co-rotating frame	m/s <sup>2</sup>
$r$	Position vector of a point along pitching axis	m
$R_\eta$	Rotation matrix about pitching axis	-
$R_\theta$	Rotation matrix about heaving axis	-
$R_\phi$	Rotation matrix about sweeping axis	-
$R_{all}$	Combined (total) Rotation matrix	-

Contents

Symbol	Quantity	Unit
$e_{z_i}$	Unit vector in $z_i$ direction	-
$e_{y_\theta}$	Unit vector in $y_\theta$ direction	-
$e_{x_\eta}$	Unit vector in $x_\eta$ direction	-
AOA	Angle of Attack	rad
$v_{x_c}$	Translational velocity in $x_c$ axis	m/s
$v_{y_c}$	Translational velocity in $y_c$ axis	m/s
$v_{z_c}$	Translational velocity in $z_c$ axis	m/s
$\omega_{x_c}$	Angular velocity about $x_c$ axis	rad/s
$\omega_{y_c}$	Angular velocity about $y_c$ axis	rad/s
$\omega_{z_c}$	Angular velocity about $z_c$ axis	rad/s
$\alpha_{x_c}$	Angular acceleration about $x_c$ axis	rad/s <sup>2</sup>
$\alpha_{y_c}$	Angular acceleration about $y_c$ axis	rad/s <sup>2</sup>
$\alpha_{z_c}$	Angular acceleration about $z_c$ axis	rad/s <sup>2</sup>
$\hat{d}_{cp}^{trans}$	Chordwise Center of Pressure location	-
$C_L^{trans}$	Translational Lift Coefficient	-
$C_D^{trans}$	Translational Drag Coefficient	-
$C_{F_{y_c}}^{trans}$	Translational Resultant Force Coefficient	-
AR <sub>eff</sub>	Effective Aspect Ratio	-
$c$	Chord Length	m
$dx_c$	Spanwise strip width	m
$dz_c$	Chordwise strip width	m
$\rho^f$	Fluid density	kg/m <sup>3</sup>
$F_{y_c}^{trans}$	Translation-induced Force in $y_c$ axis	N
$\tau_{x_c}^{trans}$	Translation-induced Torque about $x_c$ axis	Nm
$\tau_{z_c}^{trans}$	Translation-induced Torque about $z_c$ axis	Nm
$F_{y_c}^{rot}$	Rotation-induced Force in $y_c$ axis	N
$\tau_{x_c}^{rot}$	Rotation-induced Torque about $x_c$ axis	Nm
$\tau_{z_c}^{rot}$	Rotation-induced Torque about $z_c$ axis	Nm

Symbol	Quantity	Unit
$C_D^{rot}$	Drag Rotational Damping Coefficient	-
$F_{y_c}^{coup}$	Coupling Force in $y_c$ axis	N
$\tau_{x_c}^{coup}$	Coupling Torque about $x_c$ axis	Nm
$\tau_{z_c}^{coup}$	Coupling Torque about $z_c$ axis	Nm
$F_{y_c}^{am}$	Added Mass Force in $y_c$ axis	N
$\tau_{x_c}^{am}$	Added Mass Torque about $x_c$ axis	Nm
$\tau_{z_c}^{am}$	Added Mass Torque about $z_c$ axis	Nm
$M$	Matrix of added mass coefficients	-
$\tau_{x_c}^{applied}$	Applied Torque about $x_c$ axis	Nm
$\tau_{x_c}^{aero}$	Total aerodynamic Torque about $x_c$ axis	Nm
$\tau_{x_c}^{iner}$	Inertial Torque about $x_c$ axis	Nm
$\tau_{x_c}^{drive}$	Inertial drive Torque about $x_c$ axis	Nm
$k_\eta$	Elastic hinge stiffness	Nm/rad
$v_{c,add}^{corot}$	Additional translational velocity in co-rotating frame	m/s
$v_{c,add}^{iner}$	Additional translational velocity in inertial frame	m/s
$v_{x_c,add}$	Additional translational velocity in $x_c$ axis	m/s
$v_{y_c,add}$	Additional translational velocity in $y_c$ axis	m/s
$v_{z_c,add}$	Additional translational velocity in $z_c$ axis	m/s
$v_{y_c,res}$	Resultant translational velocity in $y_c$ axis	m/s
$v_{z_c,res}$	Resultant translational velocity in $z_c$ axis	m/s
$v_{c,res}$	Resultant translational velocity in co-rotating frame	m/s
$v_{c,add,res}$	Resultant additional velocity in co-rotating frame	m/s
$\hat{d}$	local-chord-normalized distance from leading edge to pitching axis	m
$\hat{d}_r$	$\hat{d}$ at wing root	m
$\hat{d}_t$	$\hat{d}$ at wing tip	m



# List of Tables

6.1. Average lift and drag produced for very small magnitudes of additional velocities . . . . .	35
6.2. Average lift produced during the kinematic cycle for increasing additional velocities in the inertial y-axis . . . . .	38
7.1. Average lift and drag produced for increasing additional velocities in the inertial y-axis . .	43
7.2. Average lift and drag produced for increasing additional velocities in the inertial z-axis . .	44
7.3. Average lift and drag produced for 3m/s additional velocity oriented in both the inertial y-axis and z-axis . . . . .	44
7.4. Peak lift/ drag ratios for increasing additional velocities in the inertial y-axis and z-axis .	47
7.5. Peak lift/ drag ratios for 3m/s additional velocity in both the inertial y-axis and z-axis . .	47
7.6. Average lift and drag produced for flapping frequency of 20 Hz . . . . .	56
7.7. Average lift and drag produced for flapping frequency of 25 Hz . . . . .	56
7.8. Average lift and drag produced for flapping frequency of 30 Hz . . . . .	56



# List of Figures

1.1.	Current state of the Atalanta project . . . . .	1
1.2.	Illustration of Direct and Indirect drive mechanisms in insects <sup>[2]</sup> . . . . .	2
1.3.	Body and wing structure of the Atalanta project <sup>[2]</sup> . . . . .	3
2.1.	Four phases of a flapping wing stroke <sup>[3]</sup> . . . . .	6
2.2.	Visualisation of three Euler angles <sup>[2]</sup> . . . . .	7
2.3.	Three successive rotations <sup>[1]</sup> . . . . .	7
2.4.	Euler angles and frames of references <sup>[1]</sup> . . . . .	8
2.5.	Decomposition of total aerodynamic load <sup>[1]</sup> . . . . .	10
2.6.	Blade element method of the wing <sup>[1]</sup> . . . . .	11
2.7.	Comparison of lift, drag and aerodynamic torque about the pitching axis <sup>[1]</sup> . . . . .	11
2.8.	Comparison of passive pitching motion of Q.Wang <sup>[1]</sup> with the model of Whitney & Wood <sup>[4]</sup> . . . . .	12
3.1.	Flowchart of functions . . . . .	19
5.1.	Comparison of Translational force in $y_c$ axis for the two methods for additional 3 m/s in inertial y axis . . . . .	27
5.2.	Comparison of Translational force in $y_c$ axis for the two methods for additional 0.5 m/s in inertial y axis . . . . .	28
5.3.	Comparison of Translational force in $y_c$ axis for the two methods for additional 5 m/s in inertial y axis . . . . .	28
6.1.	Total lift vs Time comparison for zero additional velocity case . . . . .	32
6.2.	Total drag vs Time comparison for zero additional velocity case . . . . .	32
6.3.	Angle of Pitching Motion vs Time comparison for zero additional velocity case . . . . .	33
6.4.	Lift comparison for very small additional velocities . . . . .	33
6.5.	Drag comparison for very small additional velocities . . . . .	34
6.6.	Pitching Angle comparison for very small additional velocities . . . . .	34
6.7.	Translational force in $y_c$ comparison for various additional velocities in inertial y-axis . . . . .	36
6.8.	Translational force in $y_c$ comparison for various additional velocities in inertial z-axis . . . . .	36
6.9.	More lift during downstroke when additional velocity increases . . . . .	37
6.10.	More lift during downstroke when opposite additional velocities . . . . .	38
6.11.	More drag during downstroke when opposite additional velocities . . . . .	39
7.1.	Kinematic cycle with a rectangular wing <sup>[1]</sup> . . . . .	41
7.2.	Prescribed sweeping motion angle . . . . .	42
7.3.	Lift and Drag vs Time for hovering condition . . . . .	45
7.4.	Lift and Drag vs Time for additional 3 m/s in inertial y-axis . . . . .	46
7.5.	Pitching Angle differences for additional velocity in inertial y-axis . . . . .	48
7.6.	Pitching Angle differences for additional velocities in opposite directions in inertial y-axis . . . . .	48
7.7.	Angular velocity variations for additional velocity conditions . . . . .	49
7.8.	Pitching angle comparison for different $k_\eta$ for hovering condition . . . . .	50
7.9.	Pitching angle comparison for $k_\eta$ of 7 e-04 Nm/rad . . . . .	51
7.10.	Pitching angle comparison for $k_\eta$ of 8.5 e-04 Nm/rad . . . . .	51
7.11.	Pitching angle comparison for $k_\eta$ of 10 e-04 Nm/rad . . . . .	52
7.12.	Lift produced for different flapping frequencies in hovering condition . . . . .	53
7.13.	Drag produced for different flapping frequencies in hovering condition . . . . .	53
7.14.	Pitching angles for different flapping frequencies in hovering condition . . . . .	54
7.15.	Lift vs time for flapping frequency of 25 Hz . . . . .	55
7.16.	Lift vs time for flapping frequency of 30 Hz . . . . .	55

List of Figures

7.17. Changes in the rate of change of translational force . . . . .	57
7.18. Translational force for an additional velocity of 5.75 m/s in inertial y-axis . . . . .	58
7.19. Translational force differences illustration along the wingspan strips . . . . .	58
8.1. Power consumed in hovering condition[1] . . . . .	61
A.1. Lift and Drag vs Time for additional 0.5 m/s in inertial y-axis . . . . .	68
A.2. Lift and Drag vs Time for additional 3 m/s in inertial y-axis . . . . .	68
A.3. Lift and Drag vs Time for additional 5 m/s in inertial y-axis . . . . .	69
A.4. Lift and Drag vs Time for additional 0.2 m/s in inertial -z-axis . . . . .	69
A.5. Lift and Drag vs Time for additional 2 m/s in inertial -z-axis . . . . .	70
A.6. Lift and Drag vs Time for additional 3 m/s in inertial -z-axis . . . . .	70
A.7. Lift and Drag vs Time for additional 3 m/s oriented 25% to the inertial y-axis . . . . .	71
A.8. Lift and Drag vs Time for additional 3 m/s oriented 37% to the inertial y-axis . . . . .	71
A.9. Lift and Drag vs Time for additional 3 m/s oriented 53% to the inertial y-axis . . . . .	72
A.10.Lift and Drag vs Time for additional 3 m/s oriented 65% to the inertial y-axis . . . . .	72
A.11.Pitching angle comparison for increasing additional velocity in inertial y-axis . . . . .	73
A.12.Pitching angle comparison for various orientations of 3 m/s additional velocity in inertial y-axis . . . . .	73
A.13.Pitching angle comparison for $k_\eta$ of 7 e-04 Nm/rad for 5 m/s in inertial y-axis . . . . .	74
A.14.Pitching angle comparison for $k_\eta$ of 8.5 e-04 Nm/rad for 5 m/s in inertial y-axis . . . . .	74
A.15.Pitching angle comparison for $k_\eta$ of 10 e-04 Nm/rad for 5 m/s in inertial y-axis . . . . .	75
A.16.Drag vs Time for flapping frequency of 25 Hz . . . . .	75
A.17.Drag vs Time for flapping frequency of 30 Hz . . . . .	76

# 1. Introduction to the Atalanta Project

The steady rise in the use of unmanned aerial vehicles has led to exploring the possibilities of using Micro Air Vehicle (MAV), and the advancements in the fields of miniaturization of technologies such as electronics have led to the possibility of these MAVs. MAVs have several advantages, of which the advantages in the fields of drones and surveillance are paramount. The Atalanta project is also a MAV project aimed at developing an autonomous MAV. The Atalanta project is a multi-disciplinary project, where several domains such as mechanics, actuation, control, aerodynamics etc., must be researched in order to obtain the ultimate goal. Extensive work still has to be done in all domains to reach the ultimate goal of the project.

The project is aimed at several applications such as indoor surveillance, rescue operations etc., For these applications, human safety is paramount, hence it makes more sense to employ MAVs such as the Atalanta project. For such applications, MAVs can reach small spaces which the small Unmanned Air Vehicle (UAV)s might struggle to. Figure 1.1 shows the present state of the Atalanta project, which is the result of the previous works.

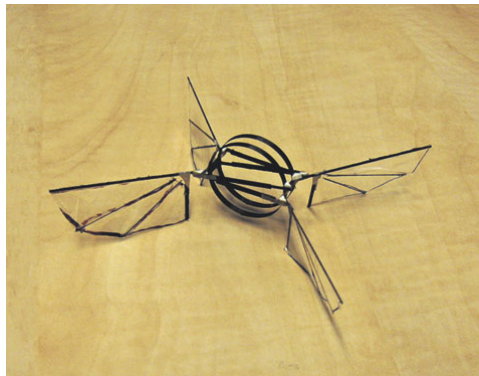


Figure 1.1.: Current state of the Atalanta project

## 1.1. Inspiration from insects and flapping wing flight

Aimed as a surveillance project, the ability to achieve hovering and slow-moving flight is important in the Atalanta project. Thus insects are the major source of inspiration, because of their ability to hover, their slow-moving flight and also the transition between them. Insects use flapping wing flight, because, compared to fixed wing flight, flapping wing flight is better suited for the above-mentioned conditions of hovering and slow-moving flight. This is primarily due to the aerodynamic differences between fixed-wing flight and flapping-wing flight. The aerodynamics of fixed-wing flight primarily states that the body has to be traveling with a certain velocity to generate the required lift. But flapping wing aerodynamics is based on the unsteady flow of air which does not directly involve the velocity of the body, thus making hovering and slow-moving flight possible.

In insects, the Flapping wing motion is achieved by various methods, which are mainly divided into two sections.<sup>[2]</sup>

- Direct-drive mechanism:  
In this mechanism, the muscles directly drive the wing, and there is no deformation of the thorax region to produce the flapping frequency and amplitude. Figure 1.2(a) shows that the activation of muscle fibers directly controls wing motion.
- Indirect-drive mechanism:  
In this mechanism, the muscles deform the thorax region and the thorax deformation activates

the wings which produce the required flapping frequency and amplitude. Figure 1.2(b) shows that the muscle activation deforms the thorax region, which in turn activates the wing to produce the required motion.

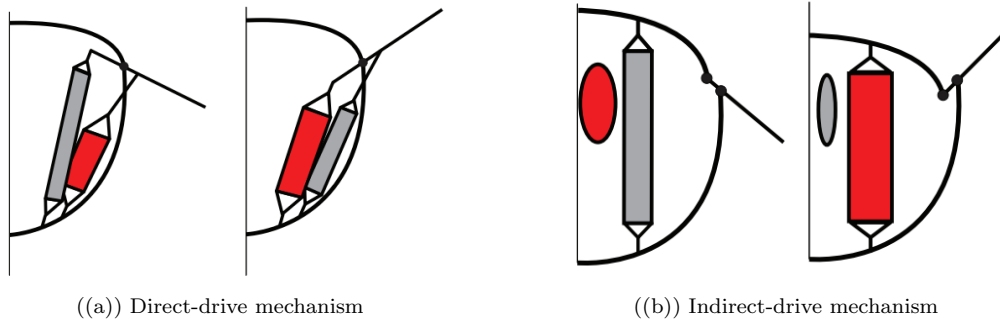


Figure 1.2.: Illustration of Direct and Indirect drive mechanisms in insects<sup>[2]</sup>

## 1.2. Utilization of resonance

The resonant properties that indirect-drive insects exhibit help to reduce the inertial cost of wing movement.<sup>[2]</sup> Weis-Fogh<sup>[5]</sup> showed that most insects have an elastic system to reduce the energetic cost of wing movement and that this elastic system serves as an efficient spring to achieve resonance. The Atalanta project takes inspiration from the indirect-drive mechanism, since in this mechanism, resonance is employed by the insects to deform the thorax region, and the wing-thorax structure acts as the compliant mechanism to activate the wings. Resonance in insects helps in producing efficient flight because resonance produces the required flapping motion by using less energy. Resonance results in resonant amplitude amplification, and thus by the use of a compliant system, the required flapping amplitude is obtained by using the least amount of power. Thus utilization of resonance in the Atalanta project serves in reducing the overall power required to produce the desired flapping motion.

## 1.3. Introduction to Flapping wing Micro Air Vehicle (FwMAV)

Flapping wing Micro Air Vehicle (FwMAV)s are a subset of MAVs, which use flapping wing motion for their flight, inspired by insects. Several projects have been done on FwMAVs, with varied methods of wing actuation methods and actuator technologies. Several previous works include The Lipca powered flapping-wing MAV<sup>[6]</sup>, The Harvard fly<sup>[7]</sup>, Caltech Microbat<sup>[8]</sup>, Vanderbilt University<sup>[9]</sup>, etc., each employing a different type of actuator mechanism, such as Piezoelectric actuators, Electroactive polymer actuators, Electromagnetic actuators, Shape memory alloy actuators, etc. The selection of the type of actuator depends on various factors such as complexity, number of joints, flapping frequency, flapping angle, and control etc., All of these actuators have their own advantages and disadvantages and depending on the choice, the required control method varies.

Of these types, the Atalanta project uses a linear electromagnetic actuator, the main reason being the ease of controlling a linear actuator, done by the use of a control circuit. A conclusion derived from observing various FwMAV projects is that a good option for the design of the wing flapping mechanism is a low complexity compliant mechanism powered by a linear actuator technology.<sup>[2]</sup>

## 1.4. Body and wing structure of Atalanta project

The current structure of the Atalanta project is based on the work of Caspar Bolsman<sup>[2]</sup>, where he designed the body structure and the wing placement. The basic conceptual idea is to design a body (thorax) region that deforms compliantly. The wings are attached to the body, and the compliant deformation of the wing and body structure produces the required flapping motion. Several concepts were designed and analyzed by Bolsman, which can be classified on the following ideas:

#### 1.4. BODY AND WING STRUCTURE OF ATALANTA PROJECT

1. Number of wings
2. Placement of wings on the body and the type of joints
3. Number of rings used in the body structure.

From the analysis done for the various concepts, a final design was generated which consists of a two-ring structure as the body and four wings are attached to the body by means of a compliant elastic connection.

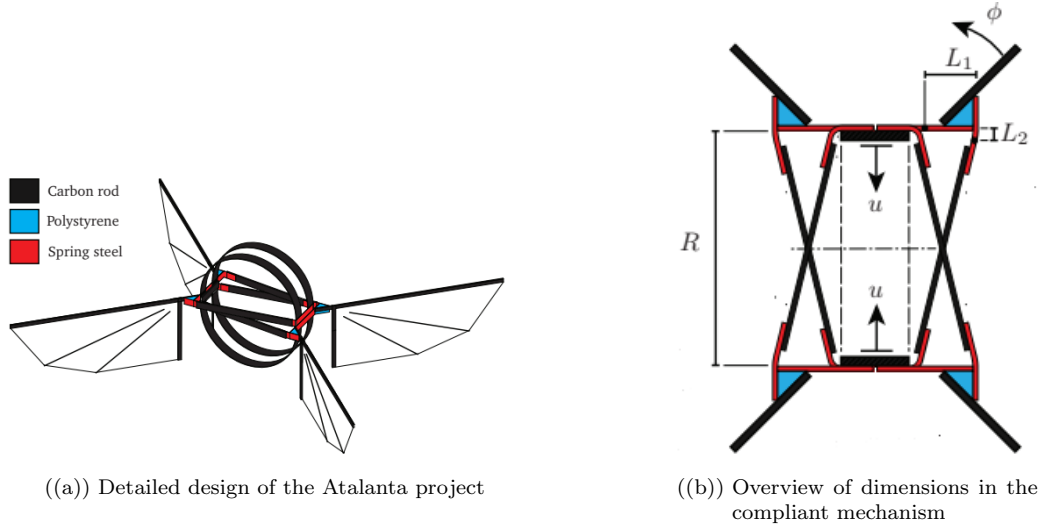


Figure 1.3.: Body and wing structure of the Atalanta project<sup>[2]</sup>

A linear actuator is used in the project, and it is placed inside the two-ring body structure. The linear actuator produces the bending of the ring structure. This linear motion is converted to the rotation of the wings by the compliant movement of the elastic connection. Figure 1.3(a) depicts the detailed design of the current state of the Atalanta project and the elastic connection of wings to the body. Figure 1.3(b) represents the various dimensions involved in the compliant mechanism of wing-thorax structure. 'u' represents the linear input of the actuator, ' $\phi$ ' represents the output angle of rotation of wings (sweeping angle), 'L1' and 'L2' represents the effective centers of the compliant links which defines the input-output relationship.

Atalanta project utilises passive pitching for producing the required pitching angles. Thus the elastic connection is to be of a certain pitching stiffness in order to produce the required motions.



## 2. Literature Review

### 2.1. Aerodynamics of the Atalanta Project

The initial stages of the literature review involved going through various previous works in the Atalanta project, which included the works of C.T. Bolsman<sup>[2]</sup>, W. Veerhoek et al.<sup>[3]</sup>, H.J. Peters<sup>[10]</sup>, R. Diekerhof<sup>[11]</sup> and Q. Wang<sup>[1]</sup>, to get an idea of the varied domains of work done. From this search, the domain of Aerodynamics was narrowed down as the topic to work on, because of the domain being complex and the work of Q. Wang<sup>[1]</sup> having an obvious continuation. This section consists of an introduction to the aerodynamics of a flapping wing flight, and a brief explanation of the quasi-steady aerodynamic model of Q. Wang for hovering conditions.

#### 2.1.1. Introduction to the aerodynamics of a flapping wing flight

The aerodynamics of a flapping wing flight is characterised by the unsteady flow of fluid surrounding the wings. The flapping motion results in a large geometrical angle of attack, which would stall conventional translating wings. This explains that the lift production in flapping-wing flight is based on different mechanisms compared to fixed-wing translating flight. The unsteady flow generated by flapping wings follows a cyclic nature. A brief explanation of the mechanisms that aid in the lift production in flapping-wing flight, and make flapping-wing flight possible is explained below.

1. **Leading edge vortex:** When a flapping wing translates through a fluid, a vortex occurs on the leading edge of the wing, and forms on top of the wing. As the wing continues its translation, the vortex grows in size and the high velocities in the vortex create a low pressure region on top of the wing which aids in lift generation. Leading edge vortex is the major contributor to the lift generation of flapping wings. Several studies have proven that the leading edge vortex remains stable until the wing changes its phase of kinematic stroke.
2. **Rotational circulation:** This mechanism states that the high rotational speeds associated with the flapping wings cause low pressure zones which aid in lift generation. This effect is predominantly present when the pitching velocities are very high, which happens during stroke reversal.
3. **Wake capture:** The vortex that was shed at the end of the previous stroke comes into contact with the following stroke, which causes unsteadiness and in turn aids in lift generation.
4. **Added mass effects:** This effect states that there exists a region of influence of fluid surrounding the wing which travels together with the wing during the translation phases. This region of fluid effectively increases the effective mass/ inertia of the wing, which can aid in lift generation. The order of added mass can be higher than the mass of the wing itself since generally the mass of the wings in flapping flight are very light.

#### 2.1.2. Kinematic description of flapping wing stroke cycle

##### Four strokes of a flapping motion:

The wing stroke in a flapping motion has to be kinematically described in order to generate analytical equations to describe the motion and to predict the loads generated from the wing stroke. Thus an understanding of the different phases in a flapping wing stroke is needed as the initial step. The four phases in a flapping motion are:

1. **Upstroke:** The phase that happens when the wing translates upwards and backwards.
2. **Pronation:** The stroke reversal phase wherein the wing changes from an upstroke to a downstroke motion.

3. **Downstroke:** The phase that happens when the wing translates downward and forward.
4. **Supination:** The stroke reversal phase wherein the wing changes from a downstroke to an upstroke motion.

Figure 2.1 schematically depicts the four phases in a flapping-wing motion.

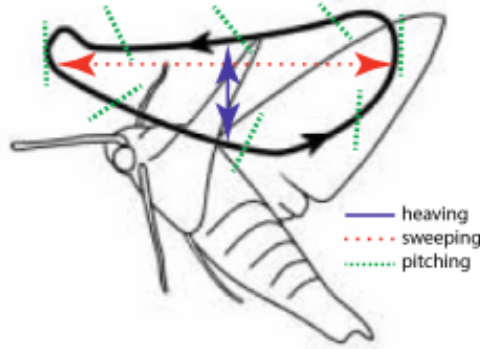


Figure 2.1.: Four phases of a flapping wing stroke<sup>[3]</sup>

#### Frames of references and Euler angles:

These four phases of the flapping motion are generally a combination of wing translation and rotation, which then can be divided into yaw, pitch, and roll. Four frames of reference are involved to describe three rotations, an inertial frame, a co-rotating frame, and two intermediate frames of reference. The inertial frame of reference is the global frame from where the successive rotations take place. Three successive rotations which happen to start with respect to the inertial frame are:

1. **Sweeping motion (yaw):** The rotation about the inertial z-axis ( $z_i$ ). It is defined by the Euler angle  $\phi$ , which is the sweeping angle. This is the first rotation that happens with respect to the inertial frame of reference, leading to an intermediate heaving frame of reference.
2. **Heaving motion (roll):** The rotation about the intermediate heaving frame y-axis ( $y_\theta$ ). It is defined by the Euler angle  $\theta$ , which is the heaving angle. This rotation leads to an intermediate pitching frame of reference, which is twice rotated with respect to the inertial frame of reference.
3. **Pitching motion (pitch):** The rotation about the intermediate pitching frame x-axis ( $x_\eta$ ). It is defined by the Euler angle  $\eta$ , which is the pitching angle. This leads to the co-rotating frame which catches all three successive rotations about the inertial frame of reference. This is the frame of reference where all load equations are computed.

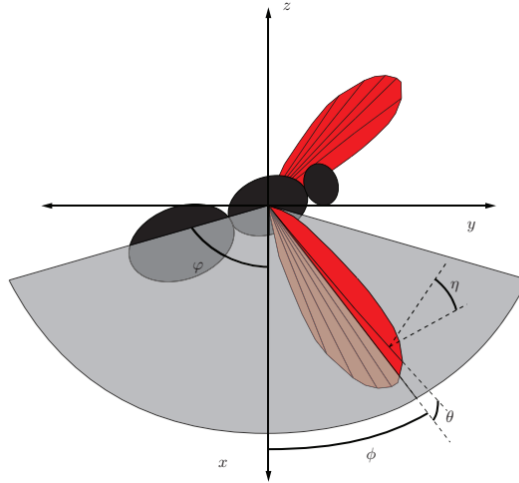


Figure 2.2.: Visualisation of three Euler angles<sup>[2]</sup>

These three rotations describe the three Euler angles used in the model. Thus the flapping motion can be quantified using three Euler angles: sweeping angle  $\phi$ , heaving angle  $\theta$ , and pitching angle  $\eta$ .<sup>[1]</sup> Figure 2.3 illustrate visually the four frames of references employed.

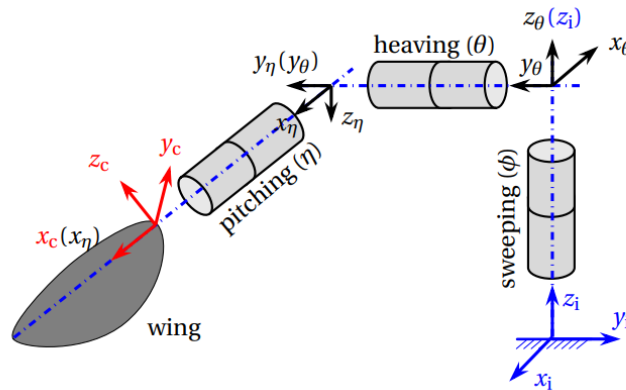
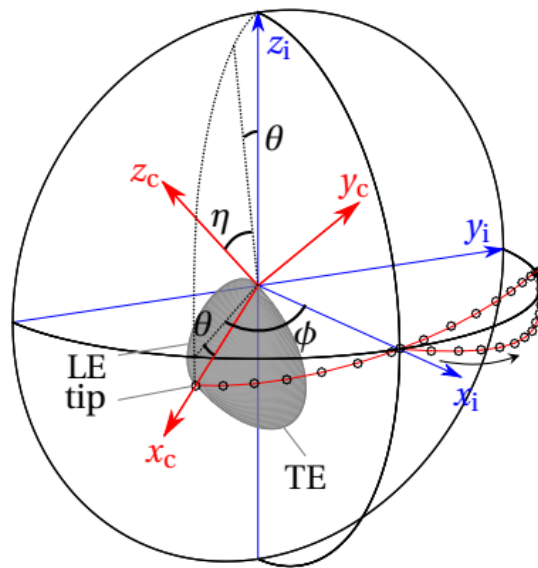


Figure 2.3.: Three successive rotations<sup>[1]</sup>

The Euler angles during flapping motion can be demonstrated in a semi-sphere constructed in the inertial frame, as shown in Figure 2.4.<sup>[1]</sup> It can be seen that  $\phi$  is the angle between the  $x_i$  axis and the projection of the  $x_c$  axis on the stroke plane,  $\theta$  is the angle between the  $x_c$  axis and its projection on the stroke plane, and  $\eta$  is the angle between the  $z_c$  axis and the plane that is perpendicular to the stroke plane and parallel to the  $x_c$  axis.<sup>[1]</sup> With these Euler angles, three successive rotations, i.e., the sweeping, heaving, and pitching motion, can be formulated.<sup>[1]</sup>

Figure 2.4.: Euler angles and frames of references<sup>[1]</sup>

## 2.2. Quasi-steady aerodynamic model of Q. Wang<sup>[1]</sup>

Extensive research in the field of flapping-wing aerodynamics has led to a wide range of modeling methods, which can broadly be divided into two categories: Experimental models and Numerical models. Of all the different available models, the previous work of Q. Wang<sup>[1]</sup> uses the Quasi-steady aerodynamic model, which uses the Blade Element Momentum (BEM) theory to compute the aerodynamic forces and torques on the wing. This is primarily due to the model being computationally efficient, making it possible to couple with it an optimization algorithm.

A quasi-steady aerodynamic model is a type of analytical model that assumes that at any instance of time, the system (flow) is assumed to be in a steady state, so the transient loads on the flapping wing are equivalent to those for steady motion at the same instantaneous translational velocity, angular velocity and angle of attack. Thus, the aerodynamic forces and torques at any instance are dependent only on the instantaneous motion of the body surface. As a result, the time dependence of the aerodynamic loads arises from the time-varying kinematics.

Q. Wang has worked on the quasi-steady aerodynamic model of the Atalanta project, for hovering conditions. In his work, to analytically predict the unsteady aerodynamic loads on flapping wings, it is presumed that:

1. The flow is incompressible, i.e., the fluid density is regarded as a constant.
2. The wing is a rigid, flat plate.
3. The resultant aerodynamic force acting on the wing is perpendicular to the chord during the entire stroke.
4. A quasi-steady state is assumed for an infinitesimal duration.

The quasi-steady aerodynamic model in his work is constructed in the co-rotating frame in order to facilitate the application of the BEM method, explained in Section 2.2.2, while the lift and drag are quantified in the inertial frame. Therefore the model requires the flapping velocity and acceleration in the co-rotating frame. This is done by transforming the sweeping and heaving motion from their corresponding frames to the co-rotating frame where pitching happens, by the Euler angles and frames of references used as explained in Subsection 2.1.2. The equations for the angular velocity and angular

acceleration in the co-rotating frame are given by,

$$\omega_c = R_\eta^T R_\theta^T R_\phi^T \dot{\phi} e_{z_i} + R_\eta^T R_\theta^T \dot{\theta} e_{y_\theta} + R_\eta^T \dot{\eta} e_{x_\eta} = \begin{bmatrix} \dot{\eta} - \dot{\phi} \sin\theta \\ \dot{\theta} \cos\eta + \dot{\phi} \cos\theta \sin\eta \\ \dot{\phi} \cos\eta \cos\theta - \dot{\theta} \sin\eta \end{bmatrix} \quad (2.1)$$

$$\alpha_c = \dot{\omega}_c = \begin{bmatrix} \ddot{\eta} - \ddot{\phi} \sin\theta - \dot{\phi} \dot{\theta} \cos\theta \\ \ddot{\theta} \cos\eta \sin\eta + \ddot{\phi} \cos\theta \sin\eta + \dot{\theta} \dot{\phi} \cos\eta - \dot{\eta} \dot{\theta} \sin\eta + \dot{\phi} (\dot{\eta} \cos\eta \cos\theta - \dot{\theta} \sin\eta \sin\theta) \\ \ddot{\phi} \cos\eta \cos\theta - \ddot{\theta} \sin\eta - \dot{\eta} \dot{\theta} \cos\eta - \dot{\phi} (\dot{\eta} \cos\theta \sin\eta + \dot{\theta} \cos\eta \sin\theta) \end{bmatrix} \quad (2.2)$$

These equations for angular velocity ' $\omega_c$ ' in Equation 2.1 and angular acceleration ' $\alpha_c$ ' in Equation 2.2 are used to calculate the translational velocity and acceleration of a point in the pitching axis, which are then used to compute the load equations on the wing. The translational velocity ' $v_c$ ' and acceleration ' $a_c$ ' are given by,

$$v_c = \omega_c \times r \quad (2.3)$$

$$a_c = \alpha_c \times r + \omega_c \times v_c \quad (2.4)$$

where ' $r$ ' represents the position vector of a point along the pitching axis.

$R_\eta$ ,  $R_\theta$  and  $R_\phi$  in the equation 2.1 represent the rotation matrices about the pitching axis, heaving axis and sweeping axis respectively. These rotation matrices are,

$$R_\eta = \begin{bmatrix} 1 & 0 & 0 \\ 0 & \cos\eta & -\sin\eta \\ 0 & \sin\eta & \cos\eta \end{bmatrix}, R_\theta = \begin{bmatrix} \cos\theta & 0 & \sin\theta \\ 0 & 1 & 0 \\ -\sin\theta & 0 & \cos\theta \end{bmatrix}, R_\phi = \begin{bmatrix} \cos\phi & -\sin\phi & 0 \\ \sin\phi & \cos\phi & 0 \\ 0 & 0 & 1 \end{bmatrix} \quad (2.5)$$

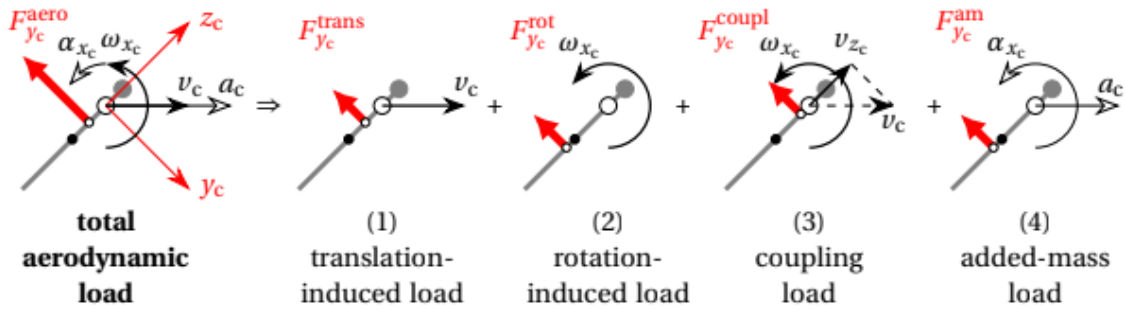
Thus the combined rotation matrix that represents all three successive rotations would be,

$$R_{all} = R_\phi * R_\theta * R_\eta \quad (2.6)$$

### 2.2.1. Aerodynamic load equations and Passive Pitching Motion

The two major sections in the work of Q. Wang<sup>[1]</sup> are the calculation of the aerodynamic load equations and the calculation of the passive pitching motion. Instead of computing the total aerodynamic load as a single term, the total load is separated into four parts: translation-induced load, rotation-induced load, load due to the coupling between the wing translation and rotation, and load due to the added-mass effects. This is because it is nontrivial to analytically formulate the total aerodynamic load in a single term because of the unsteadiness of the fluid surrounding flapping wings.<sup>[1]</sup>

Of the above four loads, the first three loads are the pressure loads induced by the translation and/or rotational velocities, and the fourth load is due to the energy dissipation or absorption by the fluid. For all four individual loads, separate equations are set up for the resultant forces and torques. Thus for each individual load, the load equations consist of both force computation and torque computation, where the force is computed along the  $y_c$  axis, and the torque computation is done about the respective axis of rotation, which are the  $x_c$  and  $z_c$  axes. After computing the individual loads, the total aerodynamic load on the wing is computed by the sum of these individual loads. The decomposition of total aerodynamic loads on a flapping wing is depicted in Figure 2.5.


 Figure 2.5.: Decomposition of total aerodynamic load<sup>[1]</sup>

Q. Wang works on computing the passive pitching motion for a specified sweeping and heaving motion in his work. The pitching motion is passive in nature in the Atalanta project, and also in most of the insects [2], [12], [13], and the passive pitching motion depends on the stiffness of the elastic hinge at the wing root. As explained, pitching motion is the rotation about the  $x_c$  axis of the co-rotating frame. Thus to compute the passive pitching motion of the wing, the torque generated about the  $x_c$  axis from all four individual loads is used, and this constitutes the aerodynamic torque  $\tau_{x_c}^{aero}$ . The equation of motion of the wing pitching is generated, which is solved to find the passive pitching motion. The idea of generating the equation of motion is, since the moment of inertia of the wing is constant in the co-rotating frame, the addition of the applied torque and the inertial torque should be zero. A detailed explanation of the individual loads is given in Chapter 3

#### Wagner Effect:

The Wagner effect is a principle in aerodynamics that describes the increase in lift experienced by a body as its speed approaches or exceeds the speed of sound in the surrounding medium, usually air. For the study of aerodynamics of insect flights, the Wagner effect is generally ignored due to the rapidly formed LEV as a result of high angle of attacks over the entire stroke and low Reynolds numbers.<sup>[1]</sup> Thus the decision to include the Wagner effect is made on the Reynolds number value and the type of wing motion.

In the work of Qi Wang, if the Wagner effect is to be included, all the circulatory loads will be multiplied by an approximate formula of Wagner's function given by Jones<sup>[14]</sup>

$$\Phi(t^*) = 1 - 0.165e^{-0.0455t^*} - 0.335e^{-0.300t^*} \quad (2.7)$$

where  $t^*$  is a non-dimensional quantity defined as the number of semi-chords the wing has traveled.<sup>[1]</sup> This equation is taken from the work of Q.Wang<sup>[1]</sup> In this thesis work for updating the model for additional velocity conditions, the Wagner effect is not included.

### 2.2.2. Aerodynamic modelling of the wing using Blade element method

As explained, the work of Q.Wang<sup>[1]</sup> uses the BEM with the quasi-steady aerodynamic model. The wing is discretized into a small number of strips, and in each strip, the load equations are computed, and the total load on the wing is computed by the summation of the individual strip loads. All four individual loads and the passive pitching motion calculation use the BEM. A visual representation of the BEM employed is given in Figure 2.6

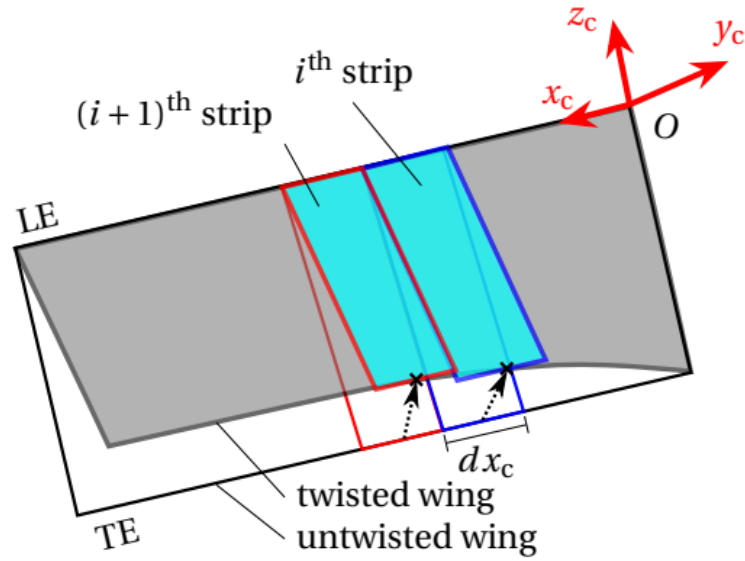


Figure 2.6.: Blade element method of the wing<sup>[1]</sup>

The width is exaggerated in the depiction in Figure 2.6, but the idea is explained where the wing is discretized into a small number of spanwise strips ( $dx_c$ ), and the load calculation is done on each individual strip.  $i$  in Figure 2.6 represents the number of the strip, and  $dx_c$  represents the width of each strip in the  $x_c$  direction. Accuracy and computational time increase when the width of each strip decreases. For the computation of rotation-induced loads, in addition to the spanwise strips, the wing is also discretized into chordwise strips ( $dz_c$ ).

### 2.2.3. Validation of Q. Wang's quasi-steady aerodynamic model for hovering conditions

The validation of Q. Wang's model for simple cases shows good correlation between calculated and measured values of lift, drag, and aerodynamic torque about the pitching axis, illustrated in Figure 2.7

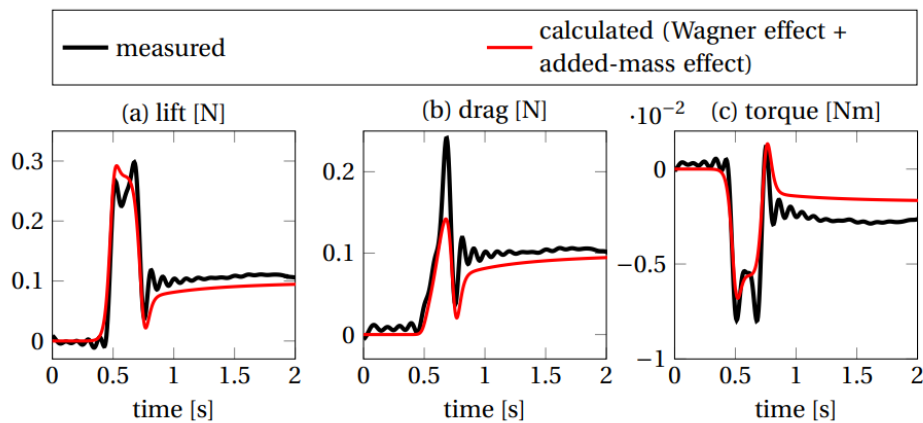


Figure 2.7.: Comparison of lift, drag and aerodynamic torque about the pitching axis<sup>[1]</sup>

The work also validates the passive pitching motion produced by comparing the calculated values of Euler angles to the measured values of Euler angles for a kinematic stroke. Figure 2.8 shows the correlation between measured and calculated passive pitching motions.

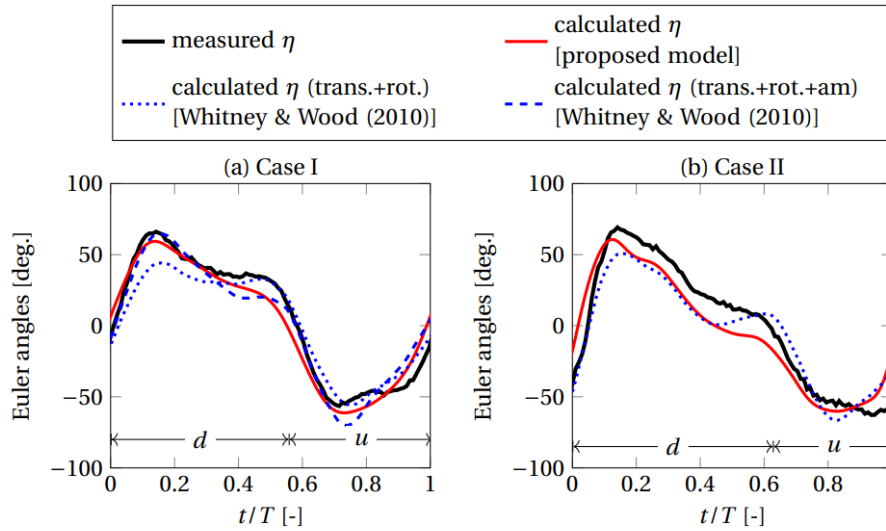


Figure 2.8.: Comparison of passive pitching motion of Q.Wang<sup>[1]</sup> with the model of Whitney & Wood<sup>[4]</sup>

From the validation of this model, it is concluded that this model can be used to predict the aerodynamic loads on a wing, the passive pitching motion, and also can be used to design and optimize a flapping wing for hovering conditions.

## 2.3. Changes required in using the same quasi-steady model for forward flight

### 2.3.1. Differences between hovering and forward flight

Understanding the important differences between hovering condition and forward flight condition of flapping wing motion is important for updating the quasi-steady aerodynamic model for additional velocity conditions. Several studies have analysed the differences between the two conditions, where the major differences can be summarised as:

1. In insects, the major difference between the two conditions is the geometric shape of the kinematic stroke. In hovering, most of the insects produced a kinematic stroke with a symmetric motion profile, thus the aerodynamic forces and pitching moment during both upstroke and downstroke are identical.<sup>[15]</sup> But in forward flight, the kinematic stroke is asymmetric in such a way that the wing in downstroke produces most of the lift force, enough to stay airborne.<sup>[15]</sup>
2. For forward flight, studies show that the amount of lift and thrust forces produced is sensitive to the flapping conditions such as flapping frequency, flapping amplitude, and flow velocity etc., Results from [16] indicate that the thrust increases with flapping frequency. The average thrust value increases with respect to the flapping frequency, like a quadratic function and the trends do not change in different angles of attacks. An increase in wind tunnel speed and flow angle of attack leads to a reduction in thrust value and increases the lift component.<sup>[16]</sup> The lifting force due to flapping will increase with an increase in flapping amplitude and flapping frequency.<sup>[17]</sup> Also from this study, the cruise speed is found as a function of the flapping frequency for various angles of attack.
3. From the study of [15], it is found that the change of the advance ratio inflicts on the underlying physics of the Leading Edge Vortex attachment.<sup>[15]</sup> This implies the implicit difference between the aerodynamics of hovering and forward flight.
4. While setting up the analytical equations, forward velocity (additional velocity) should be included as a parameter, either a dependent or free parameter, in the flight equations. This is not the case while setting up the analytical equations for hovering flight.

### 2.3.2. Major works on the changes in the quasi-steady model for forward flight conditions and their discussions

Several studies have been done in updating the quasi-steady aerodynamic model for forward flight, by accounting for the differences between hovering and forward flight. Of those, works of Jong-seob Han [15],[18] are of major importance in updating the quasi-steady model. His work focuses on insect-like flapping wings, thus implying the use of an asymmetric motion profile for the kinematic stroke in forward flight. Another major work is of Dickson and Dickinson [19]. A brief description of the major work are:

1. Dickson and Dickinson [19] indicate that the lift and drag coefficients, for a fixed angle of attack, are not constant for non-zero advance ratios, but rather vary in magnitude throughout the stroke. They show that the dependence of the lift and drag coefficients upon advance ratio and stroke position can be characterized effectively in terms of the tip velocity ratio - the ratio of the chordwise components of flow velocity at the wing tip due to translation and revolution. They introduce a modified quasi-steady model that is capable of incorporating the dependence of the force coefficients on the tip velocity ratio. [19]
2. In the work of [15], a quasi-steady model was developed for forward flight, by accounting for the differences in geometrical relationships of inclined stroke plane, induced flow, and effective angle of attack in order to suit for forward flight. This change in the geometrical relationship of kinematics was done because, an insect in forward flight not only changes the wing kinematics, but also the stroke plane and the body pitch. However, the quasi-steady model including such a geometrical relationship does not show a good agreement with the measurements, and the differences are gradually increased with respect to the advance ratio. This implies that the effects of the advance ratio brought on substantial changes in the underlying physics of the Leading Edge Vortex attachment. This also implies that the quasi-steady aerodynamic model should be compensated for, by including the advance ratio effect.
3. Work [18] is a continuation of the work of [15], where this model effectively compensated for the influences of advance ratio, and shows good moment estimation. This was done by rebuilding the correction factors of the potential and vortex force models,  $K_P$  and  $K_V$  as functions of advance ratio and angle of attack, where these correction factors are empirical. With this model, it was found that a lower value of the angle of attack during the downstroke would be an effective strategy for generating the required lift. In the upstroke phase, the added mass component played a major role in generating thrust. From the comparison of estimated and measured values of force and moment produced, it is concluded that this model can be used as an effective quasi-steady model for the forward flight of insect-like flapping motion [18].

## 2.4. Conclusions from literature retrieval

Major conclusions from the literature review include:

1. Regarding the aerodynamics of the Atalanta project, a quasi-steady aerodynamic model for hovering condition is developed by Q. Wang [1], which uses BEM theory and computes the total aerodynamic load by dividing it into four individual loads, which are, translation-induced load, rotation-induced load, coupling load, and added-mass load.
2. An important recommendation from Q. Wang's work [1] is that, for the study of forward flight, the contribution of the velocity of forward flight to the resultant translational velocity has to be included. This can be done by transforming the forward velocity from the inertial frame to the co-rotating frame and then adding this to the translational velocity  $v_c$ . [1] This recommendation is used as a major inspiration for this research work.
3. Q. Wang does not use any empirical variable to fit the model.
4. For insect-like flapping motion, i.e., the flapping motion that utilizes asymmetric kinematic profile of motion for forward flight, the updation of the quasi-steady aerodynamic model should follow the procedure of Han's work [18], where the correction factors  $K_P$  and  $K_V$  are rebuilt as functions of advance ratio and angle of attack. This model is a semi-empirical model meaning results from experimental tests are used in generating the model.

## 2.5. Research Question

The research gap pertaining to my project would be that, for the Atalanta project, the work on a quasi-steady aerodynamic model for forward flight conditions (additional velocity conditions) is yet to be done. This work would be a continuation of Q. Wang's work<sup>[1]</sup>, which deals with the quasi-steady model for hovering conditions. Another research gap found was that the works [19], [15], [18] that deal with the quasi-steady model for forward flight, all use an asymmetric kinematic profile for the flapping motion in order to mimic the motion produced by an insect. The fundamental differences of aerodynamics between symmetric and asymmetric kinematic profiles are studied in these works and the final result effectively produces a good model for the asymmetric profile. Since the Atalanta project uses a linear actuator to produce the required flapping motion and is aimed on minimizing the total power consumed, using an asymmetric kinematic profile during upstroke and downstroke phases is nearly impossible, because of the complex control of the linear actuator and the increased power requirement that are necessary for that. And, since the prescribed symmetric sweeping motion profile is to be used in the Atalanta project, can the results of works [19], [15], [18] be used to update the quasi-steady model for our project is another research gap that needs to be addressed.

Thus the research questions for my project, from the identified research gaps would be, how to update the quasi-steady aerodynamic model of Q. Wang for additional velocity conditions (mimicking forward flight conditions) by still using the prescribed sweeping motion produced by a linear actuator? What are the various observations made by incorporating the additional velocities into the updated quasi-steady aerodynamic model?

### 3. In-depth understanding of Q. Wang's quasi-steady model

Initial work included the choice of the general approach considered, to answer the research question. The main choice made was not to use any empirical variable in the updated model for additional velocity conditions, reasons being:

1. Q. Wang's work did not use any empirical variable in the quasi-steady model, to enable the model for application of shape and kinematics optimization.<sup>[1]</sup> Thus to continue the work on the aerodynamics of the Atalanta project, the update of Q. Wang's quasi-steady aerodynamic model to include additional velocities was also done without the use of any empirical variables.
2. The scope of this thesis project is not concerned with the experimental verification and correction of the aerodynamics of the Atalanta project, but rather focuses on the analytical methods to include the additional velocities in the load calculations.

Various analytical methods were analysed to update the quasi-steady model to include additional velocities. Thus the initial step was to understand the quasi-steady model of Q. Wang in detail. The high complexity of the model that uses multiple functions and equations required the need of breaking down the entire process into smaller steps. A brief description of the steps to understand the work of Q. Wang is included in this section.

#### 3.1. Input Parameters and Kinematic motions

Several input parameters were employed in Q. Wang's model, which is classified into vehicle parameters that include vehicle parameters such as the mass of the vehicle and the number of wings etc., morphological parameters that include parameters for wing description, kinematic parameters that include parameters for describing the kinematic strokes, control parameters that include parameters for discretization and optimization control, and constant parameters that include the constants such as fluid density and Young's Modulus of spring steel. These parameters are used in various functions to generate necessary inputs for the aerodynamic load and passive pitching calculation.

The morphology of the wing is described using three separate functions, namely WingShape function that describes the wing discretization, WingThicknessDistribution function that describes the wing thickness distribution all over the wing, and WingMassDistribution function that is used to compute the inertia matrix, added mass coefficient matrix and mass center of the wing. These three functions cumulatively describe the morphology of the wing, which is used in the analytical model.

The final section of input functions is the kinematic motions, which are the sweeping motion, the pitching motion and the heaving motion. Q. Wang's quasi-steady model uses a prescribed sweeping and heaving motion, while the passive pitching motion is solved for as explained in Section 3.4. The prescribed sweeping/ heaving motion takes in parameters such as flapping frequency in Hz, sweeping/ heaving amplitudes in rad, sweeping/ heaving offsets in rad, etc. The output of these prescribed motions are the sweeping/ heaving angle, angular velocity, and angular acceleration. For this thesis project, the prescribed motions are simple sinusoidal harmonic functions.

#### 3.2. Angle of attack and aerodynamic load equations

This Section explains the calculation of the angle of attack and the aerodynamic load equations, by briefly explaining the underlying concepts and the equations used.

### 3.2.1. Angle of attack

The angle of attack for a rigid wing model can be calculated by the inverse cosine function of the absolute value of the ratio of the translational velocity ' $v_{z_c}$ ' in the  $z_c$  axis, and the translational velocity ' $v_c$ ' in the co-rotating frame,<sup>[1]</sup> given by the equation,

$$AOA = \arccos(|v_{z_c}/v_c|) \quad (3.1)$$

This can further be simplified by expanding  $v_{z_c}$  and  $v_c$  based on their definition, which is given by,

$$v_{z_c} = x_c * \omega_{y_c} \quad (3.2)$$

$$v_c = x_c * \sqrt{\omega_{y_c}^2 + \omega_{z_c}^2} \quad (3.3)$$

where  $x_c$  is the coordinate of a point along the  $x_c$  axis. Thus the angle of attack can be simplified for hovering condition as,

$$AOA = \arccos(|\omega_{y_c}/\sqrt{\omega_{y_c}^2 + \omega_{z_c}^2}|) \quad (3.4)$$

This angle of attack (AOA) is used in the model. If the real AOA is higher than  $\pi/2$ , then the Trailing Edge (TE) is taken as the Leading Edge (LE), and then the AOA becomes  $\pi - AOA$ , thus the angle of attack in the model is always less than  $\pi/2$ . This angle of attack is used in the calculation of the center of pressure, lift coefficients and force coefficients.

### 3.3. Center of pressure, and coefficients of lift, drag, and force

The model of Q. Wang<sup>[1]</sup> calculates the center of pressure, lift coefficients and force coefficients in different ways depending on the requirements and the complexity required in the model. The different ways employed to calculate the center of pressure value are either an analytical method, a method from the work of Dickson et.al.,<sup>[20]</sup> or a method from the work of Han et.al.,<sup>[21]</sup>. The two different ways that were employed to calculate the Coefficient of Lift ( $C_L$ ), Coefficient of Drag ( $C_D$ ), and Coefficient of Force ( $C_F$ ) were a State-space method from Taha et.al.,<sup>[22]</sup> and a method that uses empirical force coefficients. All these different methods that were employed in Q. Wang's model<sup>[1]</sup> is explained in the appendix section. But in this research work, for computing the center of pressure, the analytical method was used, and to calculate the coefficients of lift, drag, and force, the State-space method from Taha et.al.,<sup>[22]</sup> is used. The used equations to compute these values are,

$$\hat{d}_{cp}^{trans} = (0.5/90) * AOA/\pi * 180 \quad (3.5)$$

$$C_L^{trans} = \pi * AR_{eff} * \sin(2 * AOA)/(2 + \sqrt{AR_{eff}^2 + 4}) \quad (3.6)$$

$$C_D^{trans} = C_L^{trans} * \tan(AOA) \quad (3.7)$$

$$C_D^{trans} = 2 * \pi * AR_{eff} * (\sin(AOA))^2/(2 + \sqrt{AR_{eff}^2 + 4}) \quad (3.8)$$

$$C_{F_{y_c}}^{trans} = C_L^{trans}/\cos(AOA) \quad (3.9)$$

$$C_{F_{y_c}}^{trans} = 2 * \pi * AR_{eff} * \sin(AOA)/(2 + \sqrt{AR_{eff}^2 + 4}) \quad (3.10)$$

where Equations 3.8 and 3.10 are expanded equations of Equations 3.7 and 3.9 respectively.

### 3.3.1. Translation-induced loads

The translation of the wing produced primarily due to the sweeping motion causes the translation-induced load. The load equations employ the lift coefficient and the translational force coefficients calculated from the angle of attack, given by Equations 3.5, 3.6, 3.8, and 3.10. The translation-induced loads are subdivided into three which are, the wing translation-induced force  $F_{y_c}^{trans}$  in the  $y_c$  axis, the torques about the  $x_c$  axis, ' $\tau_{x_c}^{trans}$ ', and  $z_c$  axis, ' $\tau_{z_c}^{trans}$ ', of the co-rotating frame due to translation. The equations for these three load equations are given by,

$$F_{y_c}^{trans} = -sgn(\omega_{z_c})(1/2)\rho^f(\omega_{y_c}^2 + \omega_{z_c}^2)C_{F_{y_c}}^{trans} \int_0^R x_c^2 c dx_c \quad (3.11)$$

$$\tau_{x_c}^{trans} = \begin{cases} -sgn(\omega_{z_c})(\rho^f/2)(\omega_{y_c}^2 + \omega_{z_c}^2)C_{F_{y_c}}^{trans}(\hat{d}_{cp}^{trans} - \hat{d}) \int_0^R x_c^2 c^2 dx_c, & \text{when } \omega_{y_c} \leq 0 \\ -sgn(\omega_{z_c})(\rho^f/2)(\omega_{y_c}^2 + \omega_{z_c}^2)C_{F_{y_c}}^{trans}(1 - \hat{d}_{cp}^{trans} - \hat{d}) \int_0^R x_c^2 c^2 dx_c, & \text{when } \omega_{y_c} > 0 \end{cases} \quad (3.12)$$

and,

$$\tau_{z_c}^{trans} = -sgn(\omega_{z_c})(\rho^f/2)(\omega_{y_c}^2 + \omega_{z_c}^2)C_{F_{y_c}}^{trans} \int_0^R x_c^3 c dx_c \quad (3.13)$$

In all equations given in this work, ' $x_c$ ' represent the position of the strip along the wingspan, and does not indicate the  $x_c$  axis. It is important to understand the influence of translational velocity  $v_c$  in the calculation of the above load equations. For translation-induced loads, the squared value of the translational velocity  $v_c$  is used for the calculations, where  $v_c$  is given in Equation 3.3.

### 3.3.2. Rotation-induced loads

When a wing rotates about an arbitrary axis in a medium, it experiences distributed loads, which leads to rotation-induced loads. To calculate this load using BEM, the wing has to be discretized into chordwise strips, and the resultant rotation-induced force is calculated by integrating the load on each infinitesimal area over the entire wing surface. The rotation induced loads are divided into three, which are the force ' $F_{y_c}^{rot}$ ' in the  $y_c$  axis due to rotation, and torques about  $x_c$  and  $z_c$  axes, which are  $\tau_{x_c}^{rot}$  and  $\tau_{z_c}^{rot}$  respectively. These equations are given by,

$$F_{y_c}^{rot} = (\rho^f/2)\omega_{x_c}|\omega_{x_c}|C_D^{rot} \int_0^R \int_{\hat{d}_{c-c}}^{\hat{d}c} z_c|z_c| dz_c dx_c \quad (3.14)$$

$$\tau_{x_c}^{rot} = -(\rho^f/2)\omega_{x_c}|\omega_{x_c}|C_D^{rot} \int_0^R \int_{\hat{d}_{c-c}}^{\hat{d}c} |z_c|^3 dz_c dx_c \quad (3.15)$$

and,

$$\tau_{z_c}^{rot} = (\rho^f/2)\omega_{x_c}|\omega_{x_c}|C_D^{rot} \int_0^R \int_{\hat{d}_{c-c}}^{\hat{d}c} z_c|z_c|x_c dz_c dx_c \quad (3.16)$$

where  $C_D^{rot}$  is the rotational damping coefficient. During stroke reversals,  $C_D^{rot}$  is equal to the translational drag coefficient  $C_D^{trans}$ .<sup>[1]</sup> For rotation-induced loads, there is no direct dependence of the translational velocity  $v_c$  for the load calculation.

### 3.3.3. Loads due to the coupling between translation and rotation of the wing

Although the translation and rotation-induced loads have been modelled analytically and separately, Sane and Dickinson [23] reported higher resultant force than just adding the translation and rotation components. This additional force is explained by the coupling-induced loads. The coupling between the translation and rotation can be explained by the projection of translational velocity on the  $z_c$  axis,

i.e.  $v_{z_c}$  on the circulation produced by wing rotation.<sup>[1]</sup> The resulting coupling-induced load equations are given by the equations,

$$F_{y_c}^{coup} = \begin{cases} \pi\rho^f\omega_{x_c}\omega_{y_c} \left[ \int_0^R ((3/4) - \hat{d})c^2x_c dx_c + \int_0^R (1/4)c^2x_c dx_c \right], & \text{when } \omega_{y_c} \leq 0 \\ \pi\rho^f\omega_{x_c}\omega_{y_c} \left[ \int_0^R (\hat{d} - (1/4))c^2x_c dx_c + \int_0^R (1/4)c^2x_c dx_c \right], & \text{when } \omega_{y_c} > 0 \end{cases} \quad (3.17)$$

$$\tau_{x_c}^{coup} = \begin{cases} \pi\rho^f\omega_{x_c}\omega_{y_c} \left[ \int_0^R ((3/4) - \hat{d})((1/4) - \hat{d})c^3x_c dx_c + \int_0^R (1/4)((3/4) - \hat{d})c^3x_c dx_c \right], & \text{when } \omega_{y_c} \leq 0 \\ \pi\rho^f\omega_{x_c}\omega_{y_c} \left[ \int_0^R (\hat{d} - (1/4))((3/4) - \hat{d})c^3x_c dx_c + \int_0^R (1/4)((1/4) - \hat{d})c^3x_c dx_c \right], & \text{when } \omega_{y_c} > 0 \end{cases} \quad (3.18)$$

and,

$$\tau_{z_c}^{coup} = \begin{cases} \pi\rho^f\omega_{x_c}\omega_{y_c} \left[ \int_0^R ((3/4) - \hat{d})c^2x_c^2 dx_c + \int_0^R (1/4)c^2x_c^2 dx_c \right], & \text{when } \omega_{y_c} \leq 0 \\ \pi\rho^f\omega_{x_c}\omega_{y_c} \left[ \int_0^R (\hat{d} - (1/4))c^2x_c^2 dx_c + \int_0^R (1/4)c^2x_c^2 dx_c \right], & \text{when } \omega_{y_c} > 0 \end{cases} \quad (3.19)$$

As explained in this section, these load calculations directly depend on the translational velocity  $v_{z_c}$  in the  $z_c$  axis, given by Equation 3.2

### 3.3.4. Added mass loads

When the flapping wing reciprocates, the accelerated fluid surrounding the fluid imposes a reaction on the flapping wings. This reaction is modelled as the added mass loads, which are modelled by the added mass coefficients multiplied by the acceleration of the flapping wings. The matrix of the added mass coefficients is expressed as<sup>[1]</sup>,

$$M = \begin{bmatrix} m_{22} & m_{24} \\ m_{42} & m_{44} \end{bmatrix} = (\pi/4)\rho^f c^2 \begin{bmatrix} 1 & c((1/2) - \hat{d}_0) \\ c((1/2) - \hat{d}_0) & (1/32)c^2 + c^2((1/2) - \hat{d}_0)^2 \end{bmatrix} \quad (3.20)$$

With this added mass coefficient matrix, the added mass loads are calculated by,

$$[F_{y_c}^{am} \quad \tau_{x_c}^{am}]^T = - \int_0^R M [a_{y_c} \quad \alpha_{x_c}]^T dx_c \quad (3.21)$$

where,  $a_{y_c}$  is the translational acceleration in the  $y_c$  direction, and  $\alpha_{x_c}$  is the rotational acceleration about the  $x_c$  direction. On expanding the equation 3.21, we get separate load equations for  $F_{y_c}^{am}$ ,  $\tau_{x_c}^{am}$  and  $\tau_{z_c}^{am}$ , given by the equations

$$F_{y_c}^{am} = -((\alpha_{z_c} + \omega_{x_c}\omega_{y_c})(\pi/4)\rho^f \int_0^R c^2x_c dx_c) - (\alpha_{x_c}(\pi/4)\rho^f \int_0^R c^3((1/2) - \hat{d})dx_c) \quad (3.22)$$

$$\tau_{x_c}^{am} = -((\alpha_{z_c} + \omega_{x_c}\omega_{y_c})(\pi/4)\rho^f \int_0^R c^3((1/2) - \hat{d})x_c dx_c) - (\alpha_{x_c}(\pi/4)\rho^f \int_0^R c^4((1/32) + ((1/2) - \hat{d})^2)dx_c) \quad (3.23)$$

$$\tau_{z_c}^{am} = -((\alpha_{z_c} + \omega_{x_c}\omega_{y_c})(\pi/4)\rho^f \int_0^R c^2x_c^2 dx_c) - (\alpha_{x_c}(\pi/4)\rho^f \int_0^R c^3((1/2) - \hat{d})x_c dx_c) \quad (3.24)$$

The contribution of these individual loads is added up corresponding to respective forces and torques, to calculate the total loads in the co-rotating frame of the wing. To realize these forces in the inertial frame, the combined rotation matrix of the three successive rotations, mentioned in Equations 2.5 and 2.6, is used to transform the forces from the co-rotating frame to the inertial frame. The forces in the inertial frame provide information on the lift and drag.

### 3.4. Passive pitching motion

As explained in Section 2.2.1, the passive pitching motion is computed in the quasi-steady model for a prescribed sweeping and heaving motion, by setting up an equation of motion that states that sum of the applied torque and the inertial torque should be zero. The applied torque  $\tau_{x_c}^{applied}$  consists of the elastic torque and the aerodynamic torque. The aerodynamic torque is the addition of all torques about the  $x_c$  axis. These would be the torques given in Equations 3.12, 3.15, 3.18, and 3.23. Thus the total aerodynamic torque would be given by,

$$\tau_{x_c}^{aero} = \tau_{x_c}^{trans} + \tau_{x_c}^{rot} + \tau_{x_c}^{coup} + \tau_{x_c}^{am} \quad (3.25)$$

The inertial torque  $\tau_{x_c}^{iner}$  on  $x_c$  axis can be divided into the term  $-I_{x_c x_c} \ddot{\eta}$  and the inertial drive torque  $\tau_{x_c}^{drive}$ . The inertial drive torque  $\tau_{x_c}^{drive}$  can be expressed as,

$$\begin{aligned} \tau_{x_c}^{drive} = I_{x_c x_c} [ & (1/2)\dot{\phi}^2 \cos^2 \theta \sin(2\eta) - (1/2)\dot{\theta}^2 \sin(2\eta) + 2\dot{\phi}\dot{\theta} \cos \theta \cos^2 \eta + \ddot{\phi} \sin \theta ] \\ & + I_{x_c z_c} [ \ddot{\theta} \sin \eta + (1/2)\dot{\phi}^2 \sin(2\theta) \sin \eta - \ddot{\phi} \cos \theta \cos \eta + 2\dot{\phi}\dot{\theta} \sin \theta \cos \eta ] \end{aligned} \quad (3.26)$$

The resulting equation of motion that is solved to generate the passive pitching motion is,

$$I_{x_c x_c} \ddot{\eta} + k_{\eta} \eta = \tau_{x_c}^{aero} + \tau_{x_c}^{drive} \quad (3.27)$$

This equation of motion governs the passive pitching motion of the flapping wings. An ode solver is used to solve the resulting Lagrangian equation, to solve for the pitching motion angle and angular velocity. The pitching motion angular acceleration is computed by differentiating the computed pitching angular velocity. The components of the moment of inertia matrix used in Equations 3.26, and 3.27 are computed from the wing mass distribution of the wing. The computed passive pitching motion is used as input for computing the load equations.

Thus the sequence of running the model would be first reading all the required parameters, computing the passive pitching motion, and then computing the aerodynamic loads. The following schematic represents the sequence of flow of the various functions involved in the model.

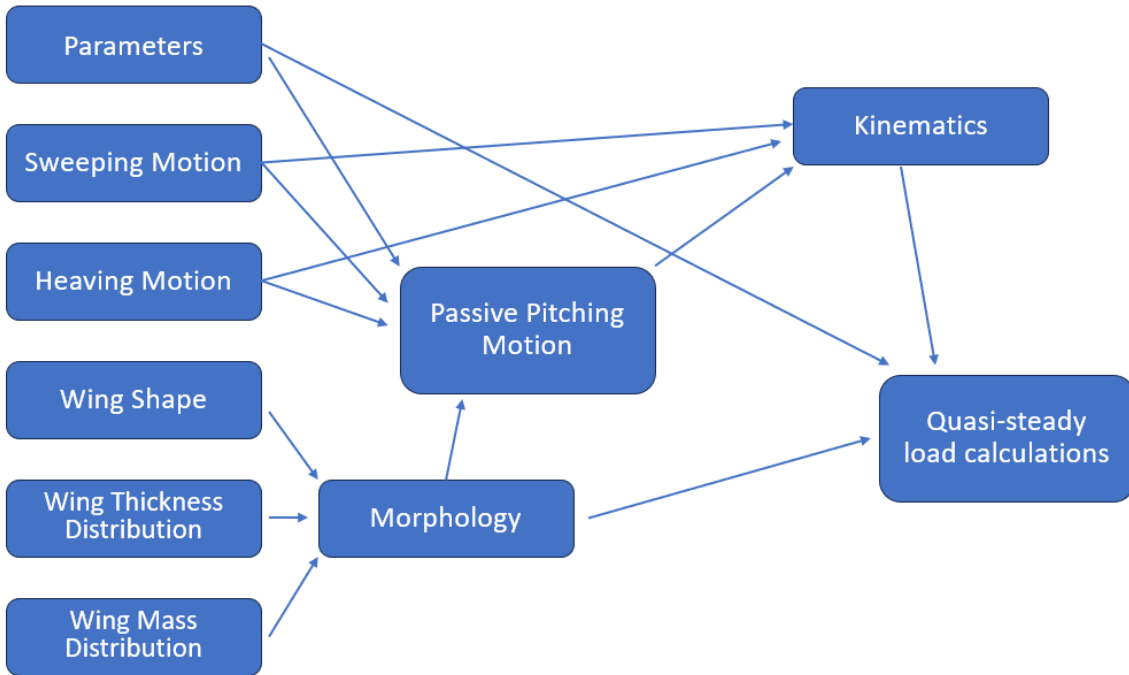


Figure 3.1.: Flowchart of functions



## 4. Assumptions made while updating the quasi-steady model

The high complexity of the quasi-steady aerodynamic model used by Q. Wang[1] for hovering conditions which uses multiple inputs, functions, and variables, as depicted in Figure 3.1 makes updating the model for additional velocity conditions a complicated process that requires making some assumptions for the initial update. This thesis work focuses on updating the load equations and angle of attack equations of the quasi-steady model to include additional velocities. Some assumptions were made depending on the complexity of the assumed function and whether the assumed function deviates from the core scope of this project. This updated model assumes a simple wing shape, which is rectangular, and assumes that the prescribed sweeping motion remains the same. Also, the wing is assumed to be a rigid one, which is then used to compute the morphology parameters of the wing required. The updated model does not use empirical variables to fit the equations. This section describes the assumptions made and the reason for making those assumptions.

### 4.1. Same prescribed sweeping motion and no heaving motion

The existing quasi-steady model of Q. Wang uses prescribed sweeping and heaving motion and computes the passive pitching motion as explained in Section 3.4. In the updated model, the same prescribed sweeping motion is considered which has an amplitude of  $(60/180) * \pi$  rad, and the vertical offset of the sweeping angle is set as 0 rad. A prescribed sweeping motion is assumed since the Atalanta project uses a linear actuator to produce the sweeping motion, and since forward flight parameters such as the power required from the actuator, and the thrust produced are not studied in this work, the same prescribed motion is assumed for the sweeping motion. Section 7.6 in Chapter 7 describes the effect of additional velocities on the computed resultant translational velocities changes between the phases of the kinematic cycle, thus gives insights on the induced stroke acceleration differences between the phases, as explained in Section 9.2. Thus this work serves as an initial step to work on calculating the change of sweeping motion (sweeping motion acceleration), which in turn affects the setting up of the angular velocities which influence the load calculations. This work assumes that there is no heaving motion from the kinematics of the wing. The reason behind this is that this assumption makes the problem simple to understand the variations of the load calculations compared to the hovering condition for various additional velocity conditions.

These assumptions do not make the approach of updating the aerodynamic load equations of the quasi-steady model conceptually wrong but rather serve as the initial step for the final quasi-steady model that optimizes all the kinematic motions.

### 4.2. Wing root is fixed in the inertial frame of reference

The wing root is assumed to be fixed in the inertial frame in this research work. This is done in order to analyze the loads that are generated on the wing when it does not move along with the inflow velocity. This assumption also follows the work of Q. Wang[1], where in his work too the wing root was not moving in the inertial frame. Thus the resultant velocity on the wing was only concerned with the velocity components  $v_{y_c}$  and  $v_{z_c}$ , implying that the wing root was fixed in the inertial frame and thus there was no velocity in the  $x_c$  axis of the co-rotating frame.

### 4.3. Wing parameters used for the observations

For almost all the observations made in this work, the flapping frequency is used as 30 Hz and the elastic stiffness of the hinge is used as  $10 \text{ e-}04 \text{ N/m}$ . These were the upper limits of the values used in the work of Q.Wang[1]. The reason for using a fixed flapping frequency and elastic hinge stiffness is to make getting the observations and analyzing them simple, thus the focus can be only on analyzing the aerodynamic result variations due to additional velocities and neglecting the flapping frequency and elastic hinge stiffness dependencies.

As explained, a rectangular wing is used in this model to reduce the complexities. The spanwise strip width, ' $dx_c$ ' is kept as a constant which is  $5 \text{ e-}04 \text{ m}$ , and the width of the chordwise strip, ' $dz_c$ ' is  $2 \text{ e-}04 \text{ m}$ . The mass of the wing is also kept constant, with a value of  $5 \text{ e-}05 \text{ kg}$ . The density of the wing is used as  $60 \text{ kg/ m}^3$  and the effective aspect ratio, ' $AR_{\text{eff}}$ ' is 2.5. These values were not assumed randomly, but the same values used in the work of Q.Wang[1]. These values are constant in all the observations made in this work, except for the sections 7.4 and 7.5, where the influence of the elastic hinge stiffness on the computed passive pitching motion and the influence of flapping frequency on aerodynamic loads respectively are studied individually, meaning both the flapping frequency and the elastic hinge stiffness are not varied simultaneously. Future work may involve the study of varying these constant parameters in the updated model.

## 5. Updated quasi-steady aerodynamic model

The main goal of this thesis project is to update the quasi-steady aerodynamic model for additional velocity conditions. The complexity of this research question requires a proper understanding of the present quasi-steady aerodynamic model, as explained in Chapter 3. A decision was made to update the model by explicitly using the translational velocity or its components in the angle of attack and aerodynamic load equations, thus additional velocities can be added to compute the results. As explained in Section 3, the translation-induced and coupling loads are updated, while changes in results of rotation-induced and added mass effects are due to the implicit changes of angular velocities. A detailed explanation of the steps for updating the model is explained in this section.

The first approach considered was to convert the angular velocities to linear velocities at each strip along the wingspan, using the relation between them given by Equation 2.3. The main idea behind this approach was that all load equations as used in Q. Wang's function explicitly use angular velocities. This approach was dismissed quickly because of the naivety of considering the existence of one-to-one mapping between angular and linear velocities when computing the linear velocities by the inverse of the cross product of angular velocities. Computing the linear velocities by the inverse of the cross product of angular velocities does not lead to a unique solution for all cases.

The main reason for the rejection of this approach is that this approach does not fully utilize the mechanics of setting up the load equations by Q. Wang's method. From a proper understanding of the load equations, it is evident that the load equations utilize translational velocity or its components, and that recalculation of the same translational velocity from the angular velocities was wrong and unnecessary, but proper use of translational velocity relations and equations was needed. This was a crude initial approach that was quickly rejected for the said reasons and not many proceedings were done for this approach.

### 5.1. Explicit velocity terms in equations

The decided final approach to update the model makes use of the proper definition of load equations and angle of attack of Q. Wang's quasi-steady aerodynamic model, that is the use of the proper definition of each component of, and total translational velocity  $v_c$  in the appropriate load equations as explained in Section 3.2.1 and Equations 3.2 and 3.3. Thus the initial step was to update the angle of attack and the load equations to explicitly contain the required translational velocity components and then additional translational velocity can be added to compute the results. The rotation-induced load equations and added mass load equations remain the same since these load equations do not explicitly contain translational velocity components, evident from Section 3.3.2 and Chapter 3.3.4. The updated equations to explicitly include velocity terms would then become,

Translation induced loads:

$$F_{y_c}^{trans} = -sgn(\omega_{z_c})(1/2)\rho^f C_{F_{y_c}}^{trans} \int_0^R v_c^2 c dx_c \quad (5.1)$$

$$\tau_{x_c}^{trans} = \begin{cases} -sgn(\omega_{z_c})(\rho^f/2)C_{F_{y_c}}^{trans}(\hat{d}_{cp}^{trans} - \hat{d}) \int_0^R v_c^2 c^2 dx_c, & \text{when } \omega_{y_c} \leq 0 \\ -sgn(\omega_{z_c})(\rho^f/2)C_{F_{y_c}}^{trans}(1 - \hat{d}_{cp}^{trans} - \hat{d}) \int_0^R v_c^2 c^2 dx_c, & \text{when } \omega_{y_c} > 0 \end{cases} \quad (5.2)$$

$$\tau_{z_c}^{trans} = -sgn(\omega_{z_c})(\rho^f/2)C_{F_{y_c}}^{trans} \int_0^R v_c^2 x_c c dx_c \quad (5.3)$$

Coupling loads:

$$F_{y_c}^{coup} = \begin{cases} \pi \rho^f \omega_{x_c} \left[ \int_0^R ((3/4) - \hat{d}) c^2 v_{z_c} dx_c + \int_0^R (1/4) c^2 v_{z_c} dx_c \right], & \text{when } \omega_{y_c} \leq 0 \\ \pi \rho^f \omega_{x_c} \left[ \int_0^R (\hat{d} - (1/4)) c^2 v_{z_c} dx_c + \int_0^R (1/4) c^2 v_{z_c} dx_c \right], & \text{when } \omega_{y_c} > 0 \end{cases} \quad (5.4)$$

$$\tau_{x_c}^{coup} = \begin{cases} \pi \rho^f \omega_{x_c} \left[ \int_0^R ((3/4) - \hat{d}) ((1/4) - \hat{d}) c^3 v_{z_c} dx_c + \int_0^R (1/4) ((3/4) - \hat{d}) c^3 v_{z_c} dx_c \right], & \text{when } \omega_{y_c} \leq 0 \\ \pi \rho^f \omega_{x_c} \left[ \int_0^R (\hat{d} - (1/4)) ((3/4) - \hat{d}) c^3 v_{z_c} dx_c + \int_0^R (1/4) ((1/4) - \hat{d}) c^3 v_{z_c} dx_c \right], & \text{when } \omega_{y_c} > 0 \end{cases} \quad (5.5)$$

$$\tau_{z_c}^{coup} = \begin{cases} \pi \rho^f \omega_{x_c} \left[ \int_0^R ((3/4) - \hat{d}) c^2 v_{z_c} x_c dx_c + \int_0^R (1/4) c^2 v_{z_c} x_c dx_c \right], & \text{when } \omega_{y_c} \leq 0 \\ \pi \rho^f \omega_{x_c} \left[ \int_0^R (\hat{d} - (1/4)) c^2 v_{z_c} x_c dx_c + \int_0^R (1/4) c^2 v_{z_c} x_c dx_c \right], & \text{when } \omega_{y_c} > 0 \end{cases} \quad (5.6)$$

The angle of attack equation has to be set up to contain explicit velocity components as well to capture the effects of additional velocities. The simplified equation of angle of attack, given by equation 3.4 is used in Q. Wang's model mainly because of computational efficiency, and the fact that the angle of attack remains the same along the wingspan strips for the hovering case. But for additional velocity conditions, the proper full definition of the angle of attack that uses translational velocity and its components, given by Equation 3.1 has to be used to include additional velocities. Thus the updated model uses the equation 3.1 to compute the angle of attack. This equation would be referred to as the updated angle of attack equation in the further sections.

## 5.2. Updating load equations for additional velocities

The next step would be to account for the additional velocities in the equations by modifying the translational velocities  $v_c$  and  $v_{z_c}$  to include both velocities from kinematics and additional velocities. Velocities from kinematics are given by Equations 3.2 and 3.3. Additional velocity is specified in the inertial frame, and it is transformed into the co-rotating frame by using the inverse of the total rotation matrix given by Equation 2.6. Thus the additional velocity in the co-rotating frame is given by Equation 5.7.

$$v_{c,add}^{corot} = inv(R_{all}) * v_{c,add}^{iner} \quad (5.7)$$

where  $v_{c,add}^{corot}$  represents the additional translational velocity in the co-rotating frame, and  $v_{c,add}^{iner}$  represents the additional translational velocity in the inertial frame. The  $v_{c,add}^{corot}$  equation in 5.7 contains the components  $v_{x_c,add}$ ,  $v_{y_c,add}$ , and  $v_{z_c,add}$  in their respective axes. Thus using these additional velocity components, the resultant velocity on the wing is recomputed in the co-rotating frame.

### 5.2.1. Updated translation-induced loads

The translation-induced loads utilize the translational velocity  $v_c$  in the load equation, thus the updated resultant velocity should include  $v_{c,add}^{corot}$  in the resultant velocity calculation. Understanding Equation 3.3 in detail shows that the translational velocity  $v_c$  is the resultant of the components  $v_{y_c}$  and  $v_{z_c}$ . This is because the wing is fixed to the root, thus the co-rotating frame does not move about the  $x_c$  axis, and thus the velocity in the  $x_c$  axis does not contribute to the resultant velocity equation. The same is assumed in this thesis work, where the co-rotating frame does not move about the  $x_c$  axis. The translational velocity  $v_c$  is represented by the equation

$$v_c = \sqrt{v_{y_c}^2 + v_{z_c}^2} \quad (5.8)$$

where  $v_{y_c}$  and  $v_{z_c}$  are given by the equations

$$v_{y_c} = x_c * \omega_{z_c} \quad v_{z_c} = x_c * \omega_{y_c} \quad (5.9)$$

Thus for additional velocity conditions, the components  $v_{y_c,add}$  and  $v_{z_c,add}$  have to be added to  $v_{y_c}$  and  $v_{z_c}$  to compute the resultant translational velocity  $v_{c,res}$ , given by the equation

$$v_{c,res} = \sqrt{(v_{y_c} + v_{y_c,add})^2 + (v_{z_c} + v_{z_c,add})^2} \quad (5.10)$$

where,

$$v_{y_c,res} = v_{y_c} + v_{y_c,add} \quad (5.11)$$

$$v_{z_c,res} = v_{z_c} + v_{z_c,add} \quad (5.12)$$

The sign of the translation-induced load equations depends on the sign of  $\omega_{z_c}$  in the model of Q. Wang. But the main idea behind this is that the sign of these load equations depends on the sign of the velocity in the  $y_c$  axis since this value determines the sign of the translation-induced load. For additional velocity conditions, it is imperative to use the sign of  $v_{y_c,res}$  instead of the sign of  $\omega_{z_c}$  because this ensures that the load equations have correct signs across the wingspan strips according to the motion of the wing that includes the additional velocity. Moreover, the choice in Equation 5.14 for the translational torque about  $x_c$  has to be based on the sign of  $v_{z_c,res}$  to capture the effects of the additional velocities.

Thus the updated translation-induced loads become,

$$F_{y_c}^{trans} = -sgn(v_{y_c,res})(1/2)\rho^f C_{F_{y_c}}^{trans} \int_0^R v_{c,res}^2 c dx_c \quad (5.13)$$

$$\tau_{x_c}^{trans} = \begin{cases} -sgn(v_{y_c,res})(\rho^f/2)C_{F_{y_c}}^{trans}(\hat{d}_{cp}^{trans} - \hat{d}) \int_0^R v_{c,res}^2 c^2 dx_c, & \text{when } v_{z_c,res} \leq 0 \\ -sgn(v_{y_c,res})(\rho^f/2)C_{F_{y_c}}^{trans}(1 - \hat{d}_{cp}^{trans} - \hat{d}) \int_0^R v_{c,res}^2 c^2 dx_c, & \text{when } v_{z_c,res} > 0 \end{cases} \quad (5.14)$$

$$\tau_{z_c}^{trans} = -sgn(v_{y_c,res})(\rho^f/2)C_{F_{y_c}}^{trans} \int_0^R v_{c,res}^2 x_c c dx_c \quad (5.15)$$

### 5.2.2. Updated coupling-loads

For coupling loads, the load equations depend on the translational velocity in the  $z_c$  axis, as explained in section 3.3.3. Thus  $v_{z_c,res}$  is used instead of  $v_{z_c}$  in the load equations, given by the equation,

$$v_{z_c,res} = v_{z_c} + v_{z_c,add} \quad (5.16)$$

The condition for the choice of the equation for the coupling loads in Q. Wang's model is the sign of  $\omega_{y_c}$ . But as in the translation-induced loads, the main idea here is to use the sign of  $v_{z_c}$  to make the choice. Thus for additional velocity conditions, the sign of  $v_{z_c,res}$  has to be taken as the condition for making the choice of the equation for coupling loads.

The resulting coupling load equations would then become,

$$F_{y_c}^{coup} = \begin{cases} \pi\rho^f\omega_{x_c} \left[ \int_0^R ((3/4) - \hat{d})c^2 v_{z_c,res} dx_c + \int_0^R (1/4)c^2 v_{z_c,res} dx_c \right], & \text{when } v_{z_c,res} \leq 0 \\ \pi\rho^f\omega_{x_c} \left[ \int_0^R (\hat{d} - (1/4))c^2 v_{z_c,res} dx_c + \int_0^R (1/4)c^2 v_{z_c,res} dx_c \right], & \text{when } v_{z_c,res} > 0 \end{cases} \quad (5.17)$$

$$\tau_{x_c}^{coup} = \begin{cases} \pi\rho^f\omega_{x_c} \left[ \int_0^R ((3/4) - \hat{d})((1/4) - \hat{d})c^3 v_{z_c,res} dx_c + \int_0^R (1/4)((3/4) - \hat{d})c^3 v_{z_c,res} dx_c \right], & \text{when } v_{z_c,res} \leq 0 \\ \pi\rho^f\omega_{x_c} \left[ \int_0^R (\hat{d} - (1/4))((3/4) - \hat{d})c^3 v_{z_c,res} dx_c + \int_0^R (1/4)((1/4) - \hat{d})c^3 v_{z_c,res} dx_c \right], & \text{when } v_{z_c,res} > 0 \end{cases} \quad (5.18)$$

$$\tau_{z_c}^{coup} = \begin{cases} \pi\rho^f\omega_{x_c} \left[ \int_0^R ((3/4) - \hat{d})c^2 v_{z_c,res} x_c dx_c + \int_0^R (1/4)c^2 v_{z_c,res} x_c dx_c \right], & \text{when } v_{z_c,res} \leq 0 \\ \pi\rho^f\omega_{x_c} \left[ \int_0^R (\hat{d} - (1/4))c^2 v_{z_c,res} x_c dx_c + \int_0^R (1/4)c^2 v_{z_c,res} x_c dx_c \right], & \text{when } v_{z_c,res} > 0 \end{cases} \quad (5.19)$$

### 5.2.3. Updated passive pitching function

Since the passive pitching motion takes into account the torque about the  $x_c$  axis, and that the translation-induced loads and coupling-loads are updated for additional velocity conditions, the updated torque equations for  $\tau_{x_c}^{trans}$  and  $\tau_{x_c}^{coup}$  (given by Equations 5.14 and 5.18) have to be used while computing the aerodynamic torque  $\tau_{x_c}^{aero}$ , which is necessary for setting up the equation of motion of passive pitching motion, given in 3.27. The updated passive pitching function also uses the updated angle of attack equations. The process of setting up the equation of motion and the lagrangian equation, and the use of the ode solver remain the same as in the hovering condition.

### 5.2.4. Proper vector addition

The incorporation of the additional velocities in the calculation of the resultant velocities should be done with proper vector addition. The method used in this thesis updates the model by adding the kinematic velocities  $v_{y_c}$  and  $v_{z_c}$  with additional velocities  $v_{y_c,add}$  and  $v_{z_c,add}$  to compute the resultant velocities  $v_{y_c,res}$  and  $v_{z_c,res}$ , which is then used to compute the resultant translational velocity  $v_{c,res}$ . This is explained in the equations 5.10, 5.11, and 5.12. Since the velocities  $v_{y_c}$ ,  $v_{z_c}$ ,  $v_{y_c,add}$ , and  $v_{z_c,add}$  are in the same frame of reference, and more importantly  $v_{y_c}$  and  $v_{y_c,add}$ , and  $v_{z_c}$  and  $v_{z_c,add}$  are in their respective same axis, there is no mismatch in the vector addition of these velocities.

The initial approaches considered to include the additional velocities in the model had the issue of the improper vector addition of velocities. A brief description of the previous approach considered and its problem with vector addition is explained in this section.

In the initial approach of updating the model, the resulting velocity is calculated by keeping the velocity from the kinematics and the additional velocity separate, instead of computing the resultant  $v_{y_c,res}$  and  $v_{z_c,res}$  velocities and then computing the resultant translation velocity  $v_{c,res}$ . This is explained by the following equation,

$$v_{c,res} = v_c + v_{c,add,res} \quad (5.20)$$

, where  $v_c$  is the translational velocity from the kinematics and  $v_{c,add,res}$  is the resultant translational velocity from the additional velocities, which are given by the equations,

$$v_c = \sqrt{v_{y_c}^2 + v_{z_c}^2} \quad v_{c,add,res} = \sqrt{v_{y_c,add}^2 + v_{z_c,add}^2} \quad (5.21)$$

Thus in the above approach, the translational velocities from kinematics and additional velocities are added up after finding their respective resultant velocities. This leads to the problem of these two resultant translational velocities not having the same direction, thus leading to the problem of vector addition. Thus this approach was not used in updating the model.

## 5.3. Calculation of results at each strip along the wingspan

The major update in the quasi-steady model is to compute the loads and the angle of attack at each strip along the wingspan, and the summation of all the individual strip loads gives the total loads acting on the wing. Even the model of Q. Wang[1] computes the aerodynamic loads at each strip, as is required by the BEM employed, several variables which were constant at all individual strips along the wingspan were taken out of the integration loop. This is evident from the equations referred to in Chapter 3, where variables such as the angular velocities and translational lift coefficient  $C_{F_{y_c}}^{trans}$  were taken out of the integration loop. But for additional velocity conditions, since at each strip, the ratio of the resultant velocities  $v_{z_c,res}$  and  $v_{c,res}$  differ, thus the analytical angle of attack, and hence the analytical coefficient of lift, drag, and force values as given by Equations 3.6, 3.7, and 3.9 is different at each strip along the wingspan. And as explained in Sections 5.1 and 5.2, the updated model uses the translational velocity variables explicitly in load equations, which vary at each strip along the wingspan. And since the angle of attack values influence the load calculations, the correct load equations at each strip can only be realized when computation is done at each strip with the new method, where all variables are taken inside the integration loop. Then the total load on the wing is the summation of all these individual loads and the total load is used for studying the global aerodynamic load characteristics. An example of an illustration where all variables are taken inside the integration loop is given by Equation 5.22. Equation 5.22 is

### 5.3. CALCULATION OF RESULTS AT EACH STRIP ALONG THE WINGSPAN

the same as Equation 5.13, but all variables are taken inside the integration loop. In the description of this section, the terminology 'updated method' refers to this case where all variables are inside the integration loop, and the terminology 'previous method' refers to the case where the variables are outside the integration loop except for the translational velocity, as in the equations in Section 5.2.

$$F_{y_c}^{trans} = - \int_0^R \text{sgn}(v_{y_c, res}) (1/2) \rho^f C_{F_{y_c}^{trans}} v_{c, res}^2 c dx_c \quad (5.22)$$

The difference in the ratio of the resultant velocities  $v_{z_c, res}$  and  $v_{c, res}$  is because the velocity from the kinematics of the wing is minimum at strips near the root and maximum at strips near the tip. Thus the presence of additional velocities has varied impact on the resultant velocities at various strips along the wingspan. This influences the analytical angle of attack, and in turn the load equations, thus the reason for computing individual strip loads by taking all variables inside the integration loop. The observations done along the wingspan explained in the section 7.7 explain in detail about the need for computing the individual calculations by the updated method. But to explain this basic premise, the effect of the translational force on the wing in the  $y_c$  axis is analyzed. A sample case studied is the inclusion of an additional velocity of 3 m/s in the inertial y-axis in the quasi-steady model. The resulting translational force in  $y_c$  axis,  $F_{y_c}^{trans}$  is calculated by two methods, where the previous method has the variables outside the integration loop and the updated method has all the variables inside the integration loop. The results are given in the following graph,

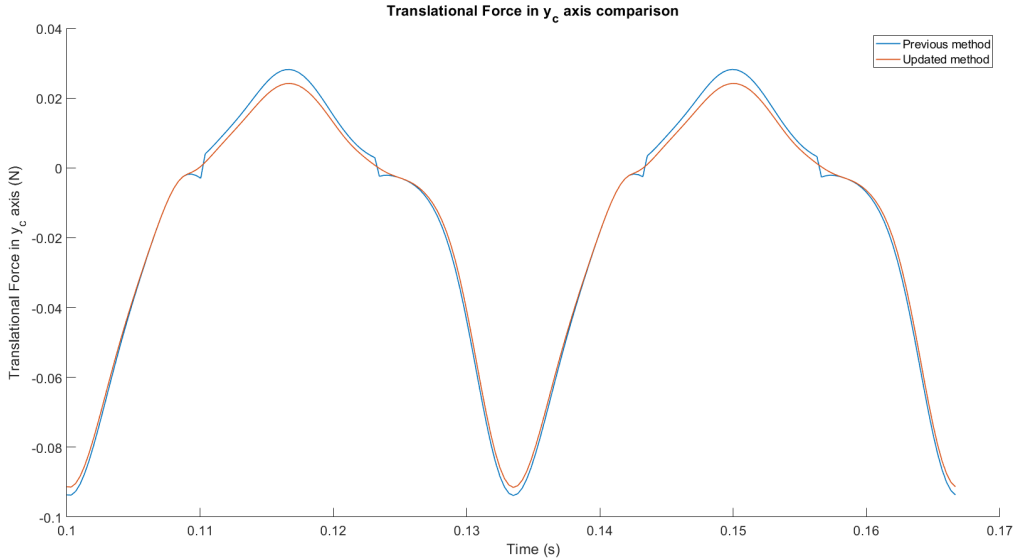


Figure 5.1.: Comparison of Translational force in  $y_c$  axis for the two methods for additional 3 m/s in inertial y axis

From the graph above (Figure 5.1), it is evident that the previous method is incorrect for additional velocity conditions, from the abrupt jumps it produces which is illogical for a physical result. Since the previous method does not account for the individual angle of attack and velocity changes at strips along the wingspan, the results produced show abrupt jumps. This method also overestimates the peak forces, which is again due to improper capture of individual strip load variations.

This effect increasingly worsens as the magnitude increases, since as the magnitude increases, the difference in the magnitude of the velocity  $v_{y_c, res}$  along the wingspan increases, which is explained in detail in the section 7.7. This case of abrupt jumps in the force value is very evident in the following graphs.

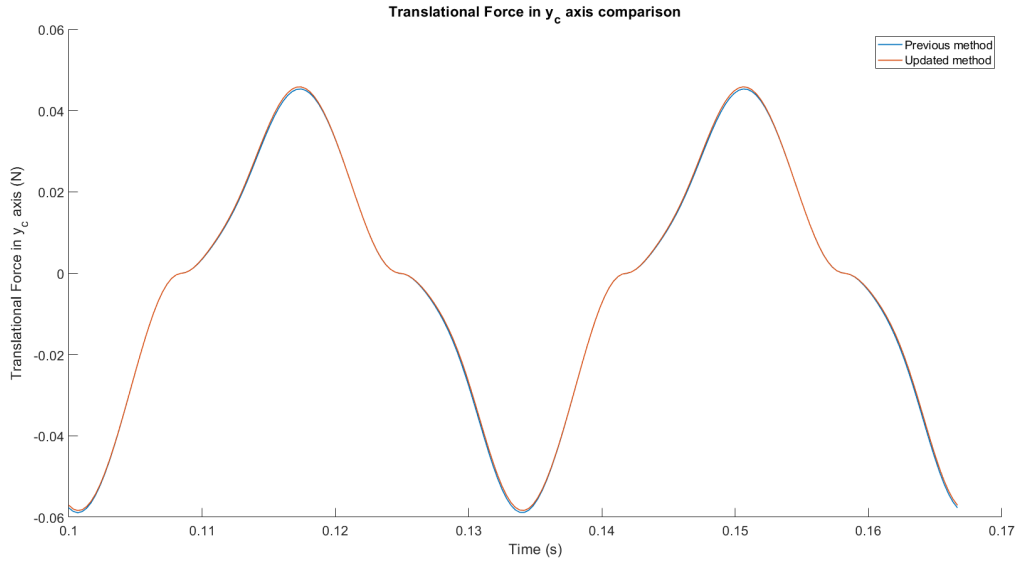


Figure 5.2.: Comparison of Translational force in  $y_c$  axis for the two methods for additional 0.5 m/s in inertial  $y$  axis

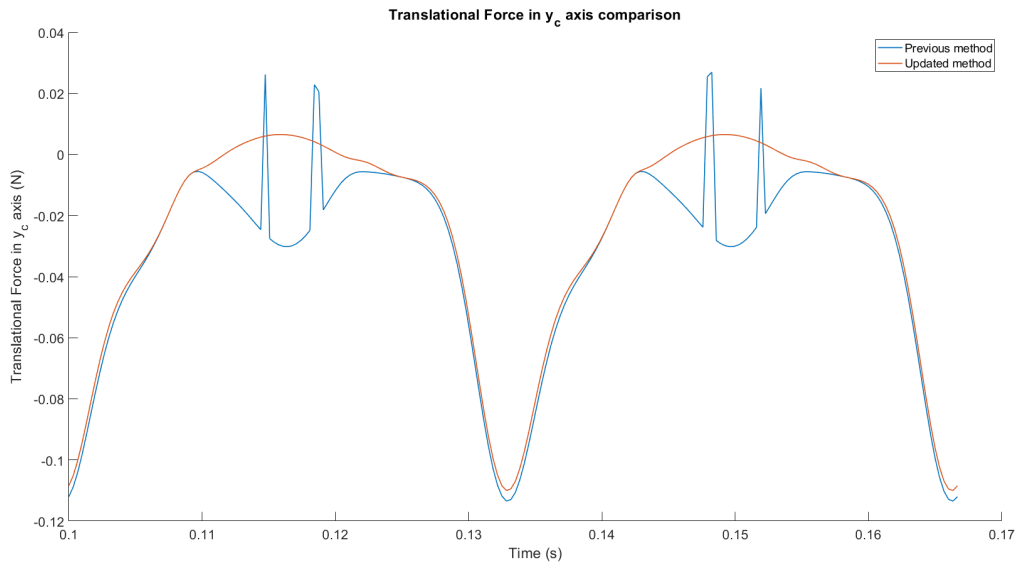


Figure 5.3.: Comparison of Translational force in  $y_c$  axis for the two methods for additional 5 m/s in inertial  $y$  axis

From the graphs 5.2 and 5.3, the necessity for computing individual strip load equations using the updated method is evident. For lower magnitudes of additional velocity, as in the graph 5.2, the previous method works just fine. But for higher magnitudes of additional velocity, as in the graph 5.3, the presence of abrupt jumps in force value is very prominent for the previous method. For the same higher magnitude of additional velocity, the updated method produces a physically meaningful force value that remains continuous throughout the cycle.

This effect is also present for additional velocities in different axes, as well as in all the load component calculations. The updated method gives a physically meaningful force result, where there are no abrupt jumps in force values during the kinematic cycle. Having abrupt jumps in aerodynamic load graphs implies that the result produced is meaningless, because all these aerodynamic loads are physical terms observed, and it is illogical to have abrupt jumps. Thus the updated model computes individual strip

### 5.3. CALCULATION OF RESULTS AT EACH STRIP ALONG THE WINGSPAN

loads and angles of attacks by calculating all the variables inside the integration loop, so the updated method accounts for the proper definition of all analytical equations in additional velocity conditions.



## 6. Verification of the updated model

The scope of this thesis project does not include validating the model with experimental results, thus verification of the updated model is done by comparing the results with the conclusions of related literature, and also the results are confirmed compared with the hovering case of Qi Wang. Also, the results are checked if the produced results provide logical patterns since the idea is that the hovering case has symmetric kinematic motion and force generation during both the strokes, and that when additional velocities are in opposite directions, the produced results should be mirrored, and for increasing magnitudes of additional velocity the produced results should vary according to the magnitude of the additional velocity. Thus this section discusses the various methods employed to affirm the correctness of the updated model.

### 6.1. Conformity with Q. Wang equations for hovering conditions

The working of the updated quasi-steady model can be confirmed by comparing the results and graphs of the updated model with the results and graphs of the Q. Wang model[1]. The main idea is, the updated model incorporates the additional velocities in the inertial frame and then uses them to compute the resultant translational velocity of the wing in the co-rotating frame, and thus when the additional velocities are zero, the updated model should compute the same aerodynamic results as in the hovering case. Moreover, the cases of very small magnitudes of additional velocities in any axes should not alter the results drastically compared to the hovering case, since the additional velocities are very small. Thus to summarize, conformity with Q. Wang equations for hovering conditions, to prove the validity of the updated model can be done in two steps.

1. For zero additional velocity case, the results of the updated model should exactly match the results of Q. Wang model
2. For very small magnitudes of additional velocities in any axes, the results of the updated model should not vary drastically compared to the hovering case.

#### 6.1.1. Zero additional velocity case

In this section, the case of zero additional velocity in the inertial frame is observed. Thus the resultant translational velocity of the wing in the co-rotating frame should be the same compared to the hovering case computed by Q. Wang. By comparing the graphs of various calculations of both models, it can be verified that both models produce the same results, but the updated model has way more computational time explained in section 7.8. The conformity of lift and drag produced, and the computed passive pitching motion is explained in this section since these observations are analyzed in detail in this thesis work.

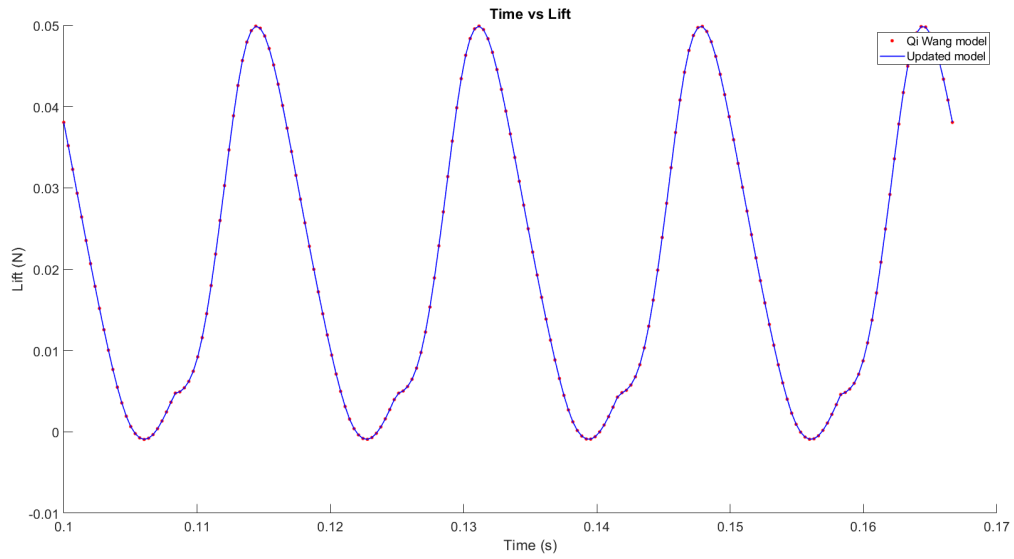


Figure 6.1.: Total lift vs Time comparison for zero additional velocity case

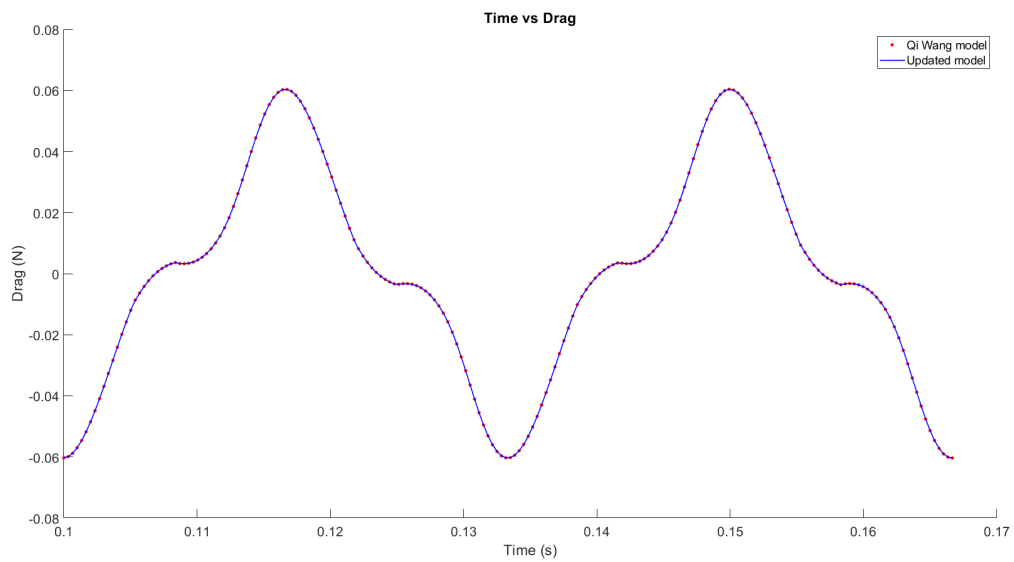


Figure 6.2.: Total drag vs Time comparison for zero additional velocity case

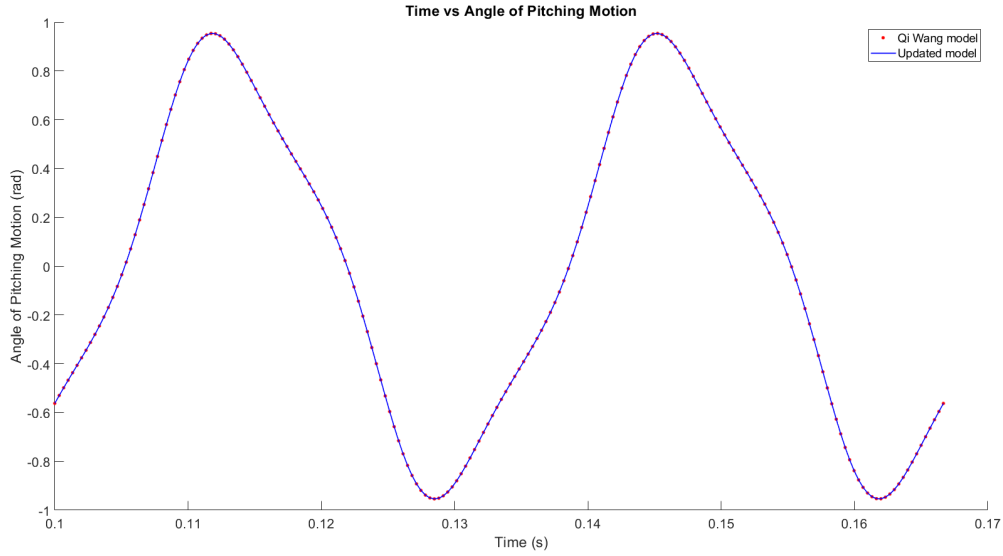


Figure 6.3.: Angle of Pitching Motion vs Time comparison for zero additional velocity case

### 6.1.2. Very small magnitudes of additional velocities

As mentioned, very small magnitudes of additional velocities should not alter the results drastically compared to the hovering case of Q. Wang. Observing the kinematic velocities produced, the maximum translational velocity in the co-rotating frame  $v_c$  is about 9.86 m/s, and the maximum mean translational velocity is about 5 m/s. Thus an additional velocity of 0.2 m/s in any direction should not affect the observed results since this additional velocity is about 4% of the maximum mean translational velocity. The observed results confirm this hypothesis. When the magnitude of the additional velocity is comparable to the velocity from the kinematics, then the results do vary and produce various observations explained in chapter 7

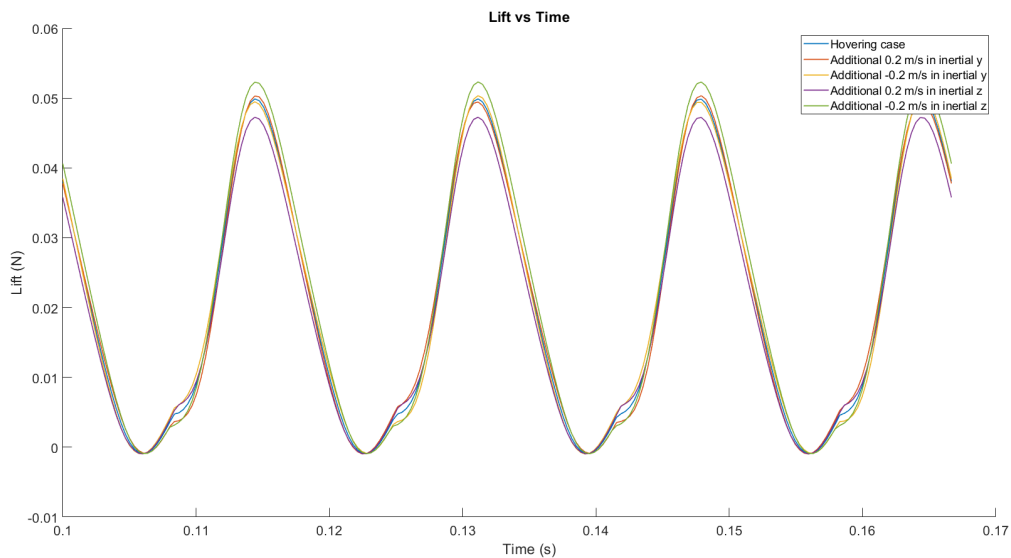


Figure 6.4.: Lift comparison for very small additional velocities

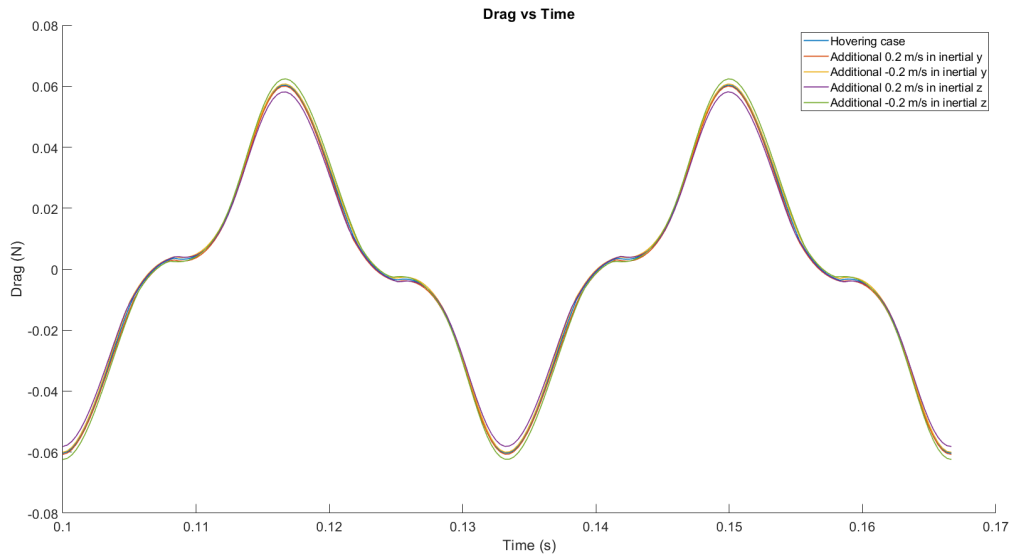


Figure 6.5.: Drag comparison for very small additional velocities

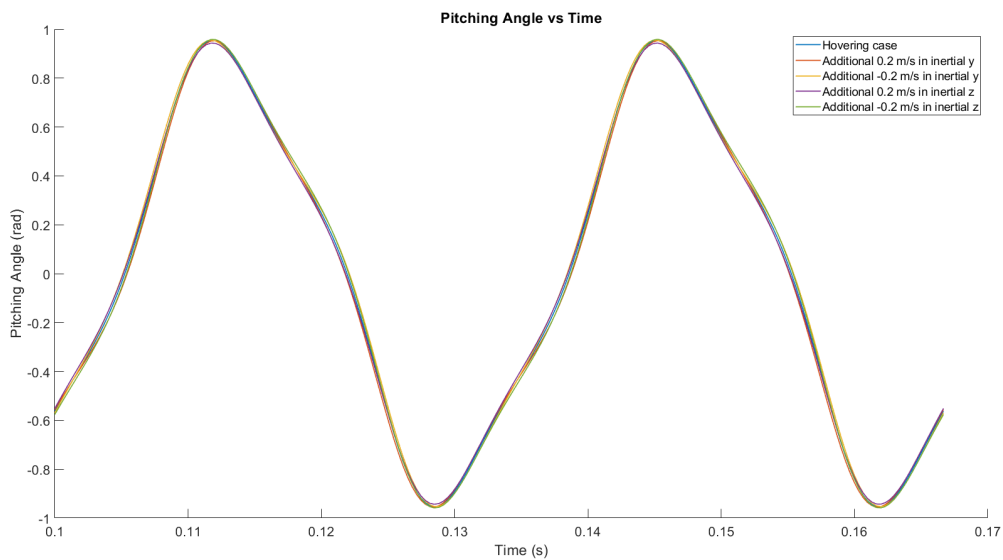


Figure 6.6.: Pitching Angle comparison for very small additional velocities

Observing the average lift and drag values produced for these small magnitudes of additional velocities, and comparing them with hovering conditions, it is evident that the results do not vary considerably. Table 6.1 illustrates this observation.

Average lift and drag values		
Additional velocity case	Average lift (N)	Average drag (N)
Hovering condition	0.0205	-3.0193 e-04
Additional velocity of 0.2 m/s in inertial y-axis	0.0206	-9.0437 e-04
Additional velocity of -0.2 m/s in inertial y-axis	0.0206	2.9999 e-04
Additional velocity of 0.2 m/s in inertial z-axis	0.0195	-2.9057 e-04
Additional velocity of -0.2 m/s in inertial z-axis	0.0216	-3.1213 e-04

Table 6.1.: Average lift and drag produced for very small magnitudes of additional velocities

## 6.2. Logical patterns of observed results

A logical affirmation of the observed results is done to ensure that the results produced by the updated model make sense for varied additional velocity cases. These include checking the asymmetry of results when the additional velocity is predominantly in the inertial y-axis, since this velocity opposes the symmetry of kinematic motion, leading to huge variations in the magnitude of the resultant velocity between the two strokes. Simultaneously, when the additional velocity is predominantly in the inertial x-axis or z-axis, the produced results are symmetric, signifying that these additional velocities do not affect the symmetry since these do not oppose the symmetry of sweeping, and thus the effect remains the same for both the strokes.

This effect of asymmetry is evident when observing the translational force variations when the additional velocity is purely in the inertial y-axis. This velocity case then increases the translational velocity in one stroke and reduces it in the other stroke depending on the direction of the additional velocity. But for additional velocities purely in the x or z-axis, the symmetry remains since the effect is the same during both strokes. This asymmetric effect is also observed in lift and drag production for additional velocities in the inertial y-axis, and this observation agrees with the conclusions of related literature, explained in section 6.3.

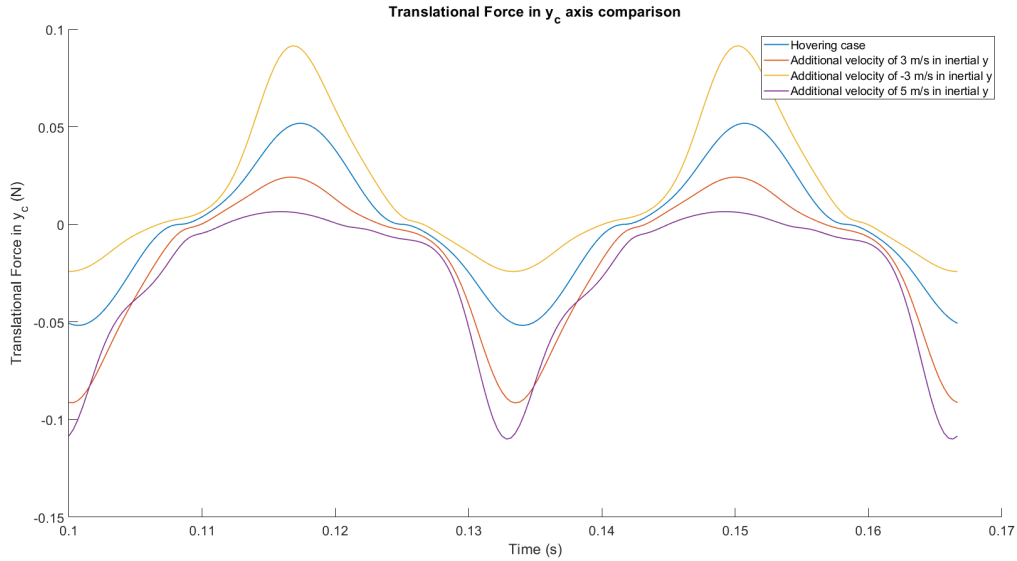


Figure 6.7.: Translational force in  $y_c$  comparison for various additional velocities in inertial y-axis

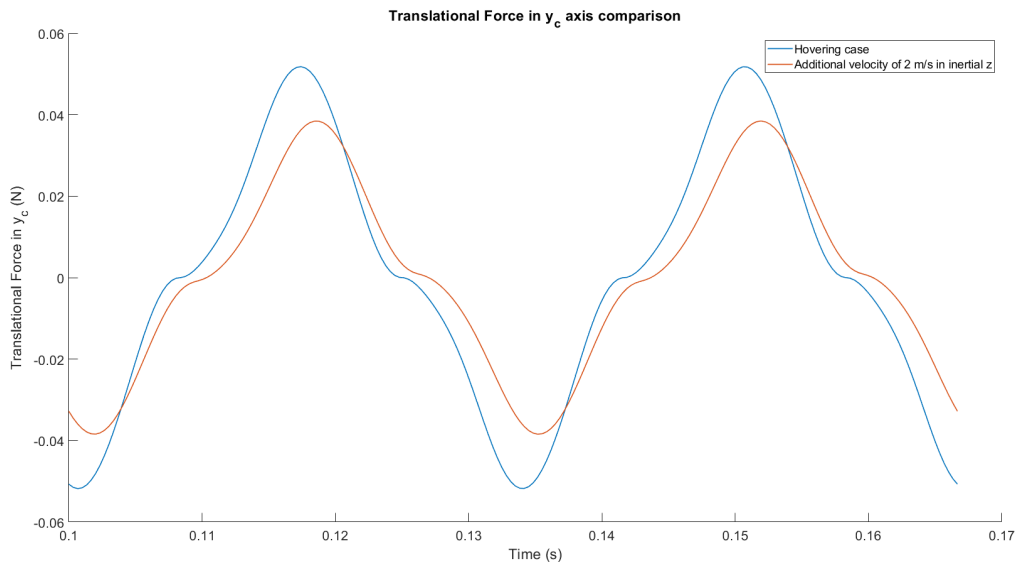


Figure 6.8.: Translational force in  $y_c$  comparison for various additional velocities in inertial z-axis

Figure 6.7 shows that for varying magnitudes of additional velocity in the inertial y-axis affects the resultant translational velocity, which thus affects the produced translational force in  $y_c$  axis, as a translational force in  $y_c$  is directly dependent on the translational velocity in the co-rotating frame. When the wing travels with the direction of the additional velocity, the additional velocity increases the resultant translational velocity, and the opposite happens during the other phase. It can also be seen that when the additional velocity is in the opposite direction, the translational force is higher in the other stroke, since now the phases of the kinematic cycle that travel with or against the additional velocity are switched.

It can be seen from figure 6.8 that when the additional velocity is purely in the inertial z-axis, the produced translational force in  $y_c$  axis is symmetric since this additional velocity affects the translational velocity in both the phases the same. This is the same for additional velocities purely in the inertial x-axis, also the observation of symmetry remains the same for lift and drag generations too. These observations of logical patterns of observed results are validated by looking at the average lift and drag produced for these said additional velocity conditions, given by Tables 7.1 and 7.2.

### 6.3. Verifying results with literature conclusions

Even though the updated model produces logical results as explained in section 6.2, it was imperative to affirm the results with some of the related literature conclusions. The starting idea of approaching this research problem was a suggestion in Q. Wang’s work that states that to study the forward flight (additional velocity conditions), the contribution of the velocity of forward flight (additional velocity) to the resultant translational velocity has to be included.<sup>[1]</sup> This can be done by transforming the forward velocity (additional velocity) from the inertial frame to the co-rotating frame and then adding this to the translational velocity  $v_c$ .<sup>[1]</sup> This idea is employed in this thesis work to update the quasi-steady model for additional velocity conditions. Thus the major conclusion of this research work is to affirm the validity of this recommendation by Q. Wang<sup>[1]</sup>.

Since this updated model observes the result changes of the aerodynamic loads when the kinematic cycle is with or against the additional velocity, and not explicitly uses whether the stroke is upstroke or downstroke in relation to the motion of the Atalanta project, it is very hard to find matching literature to compare the updated model. This is because this updated model does not consider the propulsion of the Atalanta project, thus it is not possible to assign which stroke is upstroke and which is downstroke, rather the model focuses on the relative directions of the kinematic velocities and additional velocities to compute the resultant velocities. But to compare with literature conclusion, an assumption is made in this section that, when the additional velocity is in a said direction, the wing is assumed to move in this direction, making the stroke with the direction of additional velocity the downstroke and the opposite stroke the upstroke. This also makes sense since downstroke is the forward stroke and upstroke is the backward stroke. Thus in this section to compare with literature conclusions, these terminologies are used. These assumptions for the terminologies are validated by the statement in the work of Han et.al.,<sup>[15]</sup> where it is stated that the wing in the upstroke may lose its own stroke velocity, and the wing in the downstroke gains both the enhanced stroke velocity and the aerodynamic forces.

The results of this updated model are compared with some literature conclusions to affirm the observations. The work of Han<sup>[15]</sup> states that as advance ratio increases, the wing in downstroke produces most of the lift force to stay afloat. This effect is observed in the updated model as well, where when the wing is in downstroke, the lift generated is much higher and the effect increases as the magnitude of the additional velocity in the inertial y-axis increases.

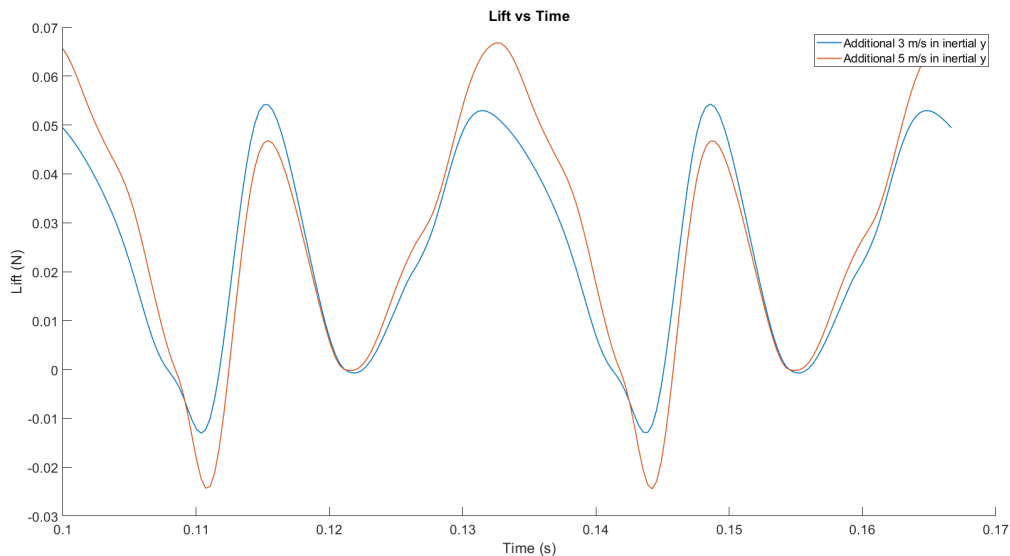


Figure 6.9.: More lift during downstroke when additional velocity increases

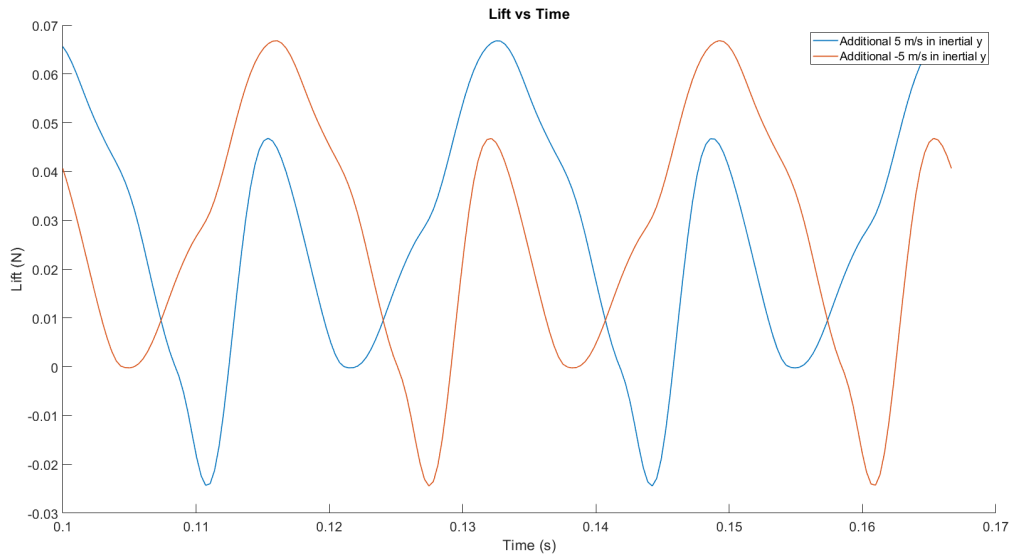


Figure 6.10.: More lift during downstroke when opposite additional velocities

In the above Figure 6.9, the second peak (around time interval 0.125 s to 0.14 s) represents the downstroke in this condition where the additional velocity is in the positive inertial y-axis. Clearly, it is evident that for higher magnitudes of additional velocity, the downstroke produces most of the lift, and for higher magnitudes of additional velocity, the peak lift in upstroke is not even the same as the weight of the wing, implying that the lift in downstroke is responsible to stay afloat, agreeing with the observation of Han<sup>[15]</sup>. Even for the comparatively lesser magnitude of the additional velocity (here, 3 m/s), the total lift produced during downstroke is higher than the lift from upstroke, compared to the hovering condition, evident from the area under the lift curve and prolonged production of lift during the downstroke. Moreover from figure 6.10, it is clear that when the same additional velocity is in the opposite direction, which means now the downstroke is shifted to the other stroke (the other peak), still the corresponding downstroke produces more lift, confirming that the model works fine for corresponding additional velocity conditions.

Average lift values during upstroke and downstroke		
Additional velocity case	Average lift during upstroke (N)	Average lift during downstroke (N)
Hovering condition (additional velocity of 0 m/s)	0.0205	0.0205
Additional velocity of 0.2 m/s	0.02	0.0208
Additional velocity of 0.5 m/s	0.0195	0.0214
Additional velocity of 3 m/s	0.0156	0.0319
Additional velocity of 5 m/s	0.0113	0.0411
Additional velocity of -3 m/s	0.0319	0.0157

Table 6.2.: Average lift produced during the kinematic cycle for increasing additional velocities in the inertial y-axis

This phenomenon of more lift production during the downstroke is more evident when looking at the average lift produced during upstroke and downstroke for increasing additional velocity conditions. From

### 6.3. VERIFYING RESULTS WITH LITERATURE CONCLUSIONS

the prescribed sweeping motion angle, the duration and timing of the two strokes are computed, and depending on the direction of the additional velocity in the inertial frame, the stroke may be identified as the upstroke or the downstroke as explained, i.e., when the kinematic velocities and additional velocity is in the same direction, it is downstroke and the upstroke being the opposite. The observed average lift produced during upstroke and downstroke for increasing magnitudes of additional velocity in the inertial y-axis is given in Table 6.2. It is evident from Table 6.2 that as the magnitude of the additional velocity increases, the average lift produced during downstroke increases confirming with the work of Han<sup>[15]</sup>.

The work of Faisal et.al.,<sup>[24]</sup> it is stated that the thrust/ weight ratio is higher during downstroke than upstroke, meaning more thrust in downstroke compared to upstroke for the same weight of the wing, and that the peak value is found at the midpoint of the stroke. This work does not study the thrust values on the wing, but since for stable flight, the thrust produced should be at least equal to the total drag so that the wing does not drift along with the additional velocity, and since this thesis works on additional velocity conditions and not forward flight propulsion, the minimum thrust can be assumed to be equal to the drag produced. The effect of more thrust (in our case drag) is also observed in the updated model, where during the downstroke, the drag is higher and hence the drag(thrust)/ weight ratio is also higher during the downstroke compared to the upstroke. The peak value also happens during the midpoint of the stroke, thus confirming the statements of Faisal et.al.,<sup>[24]</sup> The Figure 6.11 depicts these observations and also depicts that for additional velocity in the opposite direction, the corresponding downstroke produces more drag.

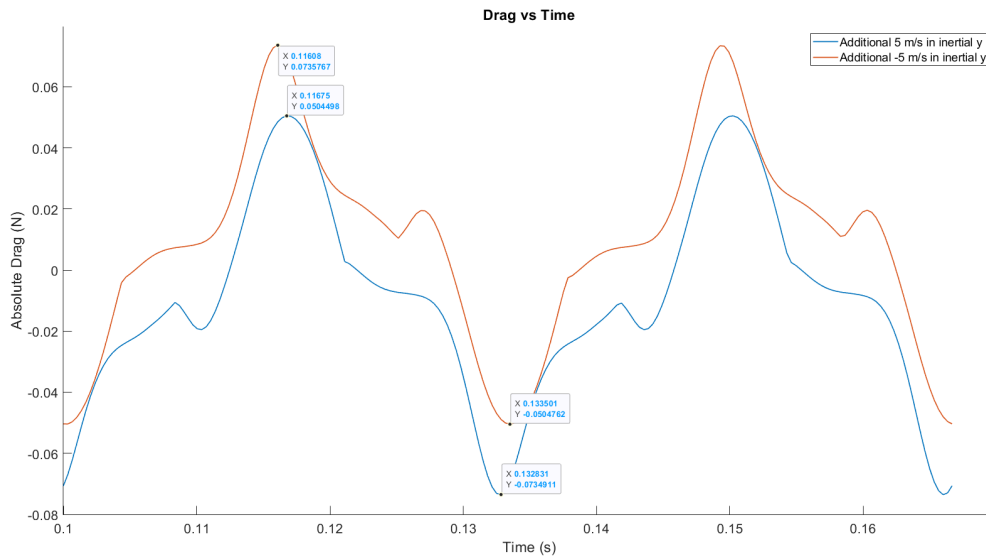


Figure 6.11.: More drag during downstroke when opposite additional velocities

In the work of Han et.al.,<sup>[15]</sup>, the blade element method is used in the quasi-steady aerodynamic model to compute the aerodynamic loads on the wing in forward flight conditions. It is stated in that work that each blade element has a different effective angle of attack along the continuously changed motion profiles.<sup>[15]</sup> This is the case in our updated quasi-steady aerodynamic model as well, since the influence of the additional velocity is different for blade strips along the wingspan, explained in Sections 5.3 and 7.7, where the analytical angle of attack is different for blade strips along the wingspan for additional velocity conditions.



## 7. Observations in additional velocity conditions

A plethora of observations can be obtained from the updated model for additional velocity conditions, ranging from observations in the global scale looking at the peak/ average lift and drag produced, to the observations along the wingspan looking at the force sign differences of strips along the wingspan. In this study, the observations done are classified into:

- Observations on average lift and drag produced
- Global peak lift and drag observations
- Observations on passive pitching motion changes
- Observations on the elastic hinge stiffness dependence on the passive pitching motion
- Observations on the influence of flapping frequency
- Observations on translational force and translational velocities
- Observations along the wingspan strips
- Observations on computational time

These varied observations were done because, for additional velocity conditions, multiple changes of results compared to the hovering condition were observed and thus it was important to observe varied results in order to sense the change of results and overall behavior of the system. But the main focus on the observations done is on the lift and drag produced for various additional velocity conditions, since these analysis on these observations are vital in understanding the possibility of forward flight for the Atalanta project. A detailed description of the various observations done in the updated model is explained in this section.

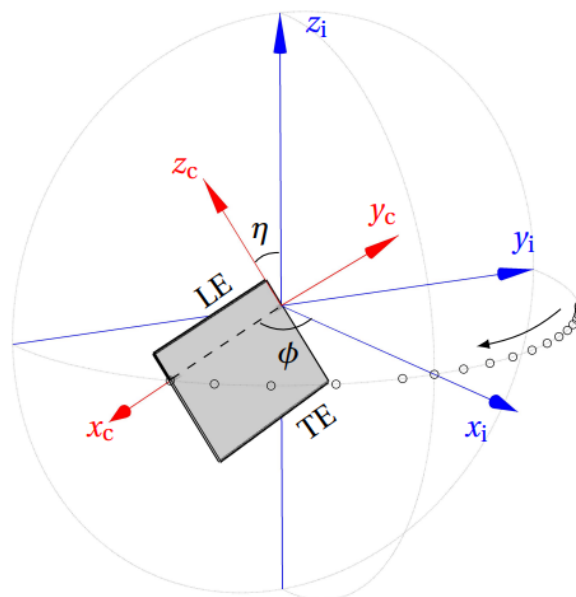


Figure 7.1.: Kinematic cycle with a rectangular wing<sup>[1]</sup>

Figure 7.1 represents the stroke cycle used in making all the observations using the updated model with the rectangular wing that is used. As explained in Section 4.1, there is no heaving motion in the kinematic cycle used for the observations, evident from Figure 7.1. The prescribed sweeping stroke can be visualized from the continuous dots in Figure 7.1, described by the sweeping angle  $\phi$ . The prescribed sweeping motion is sinusoidal in nature, and the resulting sweeping motion angle during the kinematic cycle is given by Figure 7.2.

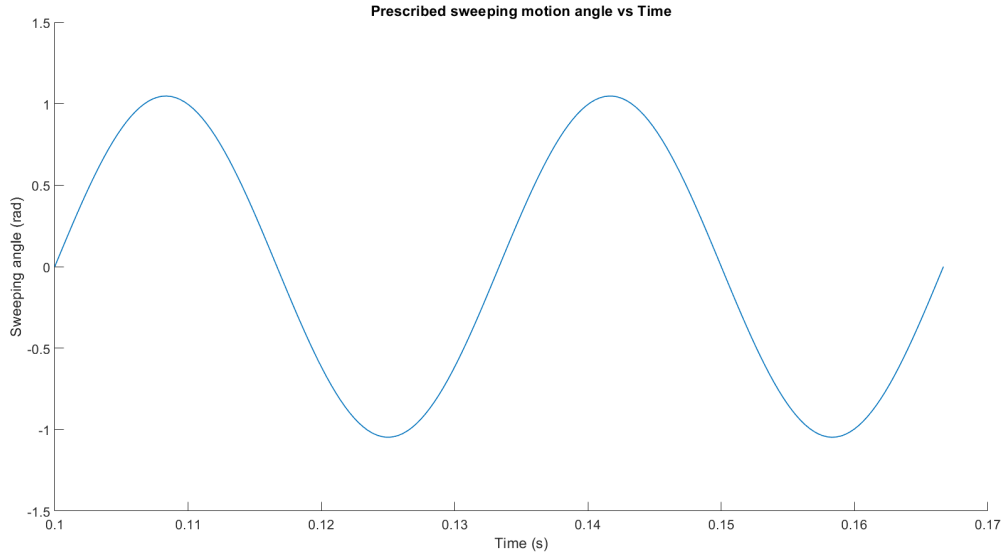


Figure 7.2.: Prescribed sweeping motion angle

From Figure 7.2, it can be deduced that the prescribed sweeping motion in the kinematic cycle used starts with an angle of 0 rad, meaning the wing is aligned with the inertial x-axis, ' $x_i$ ' which is represented in Figure 7.1. A positive slope of the values of the sweeping angle indicates an anti-clockwise rotation about the inertial z-axis ' $z_i$ ', and the sign of the kinematic velocity ' $v_{yc}$ ' in this sweeping phase has a positive sign. Thus the kinematic cycle used in these observations starts with half a stroke in the anti-clockwise direction about  $z_i$  axis, then a full stroke in the clockwise direction about  $z_i$  axis, then half a stroke in the anti-clockwise direction about  $z_i$  axis, reaching the initial sweeping position of 0 rad. This constitutes a single kinematic cycle, and in these observations, two consecutive kinematic cycles are used, and this is illustrated in Figure 7.2. These strokes resulting from the direction of rotation about  $z_i$  axis refer to the strokes of the sweeping motion or phases of the sweeping motion. It is to be noted that, the description in this Section uses the terms strokes and phases interchangeably, and it is important to note these terminology use. Also, this Section uses the terms, phases of the sweeping motion and the phases of the kinematic cycle interchangeably, meaning the phases of the kinematic cycle implicitly means the phases of the sweeping motion in the kinematic cycle. This terminology understanding is important when visualizing the phases of the kinematic cycle that is with or against the additional velocity direction.

This observations section makes use of additional velocities in different orientations in the inertial frame of reference. These are described as additional velocity in the inertial y-axis, or in the inertial z-axis, or oriented between the inertial y-axis and z-axis. As explained,  $y_i$  represents the inertial y-axis, and  $z_i$  represents the inertial z-axis. These can be visualized in Figure 7.1, where the sign of the arrows represents the positive direction of the corresponding axes. This is important for visualizing the additional velocity directions, and the interaction of the additional velocity with the kinematic velocity of the wing.

## 7.1. Observations on average lift and drag produced

Observations on the average lift and drag produced during the kinematic cycle give us information on the global force production by the wing under various additional velocity conditions and provide us insights

## 7.1. OBSERVATIONS ON AVERAGE LIFT AND DRAG PRODUCED

into possible forward flight possibilities. For the prescribed kinematic cycle explained at the beginning of this section, the average lift produced for the hovering condition is 0.0205 N and the average drag produced is  $-3.0193 \times 10^{-4}$  N. The average drag produced in the hovering condition is close to zero, because of the symmetric nature of the kinematic cycle and kinematic velocities, thus leading to identical drag production during both phases of the kinematic motion. The average lift produced in the hovering condition is not zero since both the phases of the kinematic cycle aid in lift production and neither negate the lift produced in the other phase. Figure 7.3 depicts the lift and drag produced for the hovering condition.

The presence of additional velocities should affect the average lift and drag produced in the observed kinematic cycle, since now the resultant velocities during the phases of the kinematic motion are not the same, thus leading to asymmetric drag and lift produced in both the phases, affecting the average drag and lift values. This is reflected in the updated model and the observations made are explained in this section.

Average lift and drag values		
Additional velocity case	Average lift (N)	Average drag (N)
Hovering condition (additional velocity of 0 m/s)	0.0205	$-3.0193 \times 10^{-4}$
Additional velocity of 0.2 m/s	0.0206	$-9.0437 \times 10^{-4}$
Additional velocity of 0.5 m/s	0.0206	-0.0018
Additional velocity of 3 m/s	0.024	-0.0078
Additional velocity of 5 m/s	0.0265	-0.01
Additional velocity of -3 m/s	0.024	0.0072

Table 7.1.: Average lift and drag produced for increasing additional velocities in the inertial y-axis

The presence of an additional velocity affects the average lift and/ or drag produced depending on the orientation of the additional velocity in the inertial frame. Table 7.1 shows that when the additional velocity is purely in the inertial y-axis, the average drag value is influenced the most and the average lift value is affected in a meager way. This is because the additional velocity purely in the inertial y-axis directly opposes or aids the kinematic velocities generated by the wing leading to highly asymmetric drag produced during the kinematic cycle. It is evident from Table 7.1 that the average drag increases for increasing magnitudes of additional velocity in the inertial y-axis. Another interesting observation is that, even though the average lift value for these additional velocity conditions does not vary much compared to the hovering condition, the average lift produced during the individual phases of the kinematic cycle is vastly different as the magnitude of the additional velocity increases, as shown in the Table 6.2. Thus the varying average lift produced during the individual phases of the kinematic cycle for additional velocity conditions should also be considered, even though the total average lift does not change much for additional velocities in the inertial y-axis.

When the additional velocity is purely in the inertial z-axis, the average lift value is influenced the most, since the lift technically means the force produced by the wing in the inertial z-axis, and thus additional velocity in the inertial z-axis affects the lift produced the most. For these additional velocity conditions, the average drag produced is almost the same as the hovering condition, since the additional velocity purely in the inertial z-axis does not affect the symmetric profile of wing kinematic motion. These observations are evident from the average drag and lift values observed and reported in Table 7.2

And when the additional velocity has components in both the inertial y-axis and z-axis, resulting from its orientation in the inertial frame, depending on the magnitude of the components in the respective axis directions, the average drag and lift values are affected accordingly. For an additional velocity of 3 m/s, depending on its orientation in the inertial frame the observed average lift and drag values

Average lift and drag values		
Additional velocity case	Average lift (N)	Average drag (N)
Hovering condition (additional velocity of 0 m/s)	0.0205	-3.0193 e-04
Additional velocity of -0.2 m/s	0.0216	-3.1213 e-04
Additional velocity of -2 m/s	0.0323	-3.6664 e-04
Additional velocity of -3 m/s	0.0403	-3.7143 e-04
Additional velocity of 2 m/s	0.0117	-1.9509 e-04

Table 7.2.: Average lift and drag produced for increasing additional velocities in the inertial z-axis

are listed in Table 7.3. Thus it can be concluded from the observations that, an additional velocity

Average lift and drag values		
Additional velocity of 3m/s	Average lift (N)	Average drag (N)
Purely in the inertial y-axis	0.024	-0.0078
Oriented 25° to the inertial y-axis	0.0298	-0.0071
Oriented 37° to the inertial y-axis	0.0326	-0.0058
Oriented 53° to the inertial y-axis	0.0358	-0.0039
Oriented 65° to the inertial y-axis	0.0379	-0.0027
Purely in the inertial -z-axis	0.0403	-3.7143 e-04

Table 7.3.: Average lift and drag produced for 3m/s additional velocity oriented in both the inertial y-axis and z-axis

purely in the inertial y-axis considerably affects the average drag, an additional velocity purely in the inertial z-axis considerably affects the average lift, and an additional velocity with components both in the inertial y-axis and z-axis depending on the magnitudes of the respected components the average drag and lift are affected.

## 7.2. Global peak lift and drag observations

A plethora of global observations can be done but this study focuses on the observations of lift and drag produced since these observations can be of great help in understanding the basics of approaching the solution for the problem of forward flight generation for the Atalanta project. The global peak lift and drag observations are done in this section to sense the effect of varied additional velocity conditions on the peak aerodynamic lift and drag produced.

The observations made on the peak lift/ drag ratio for varied additional velocity conditions provide interesting insights on the utilization of the optimum tilting angle of the Atalanta project that can be employed to achieve different peak lift/ drag ratios during the kinematic cycle. This is not the case in hovering conditions, where the peak lift/drag ratio remains the same for both phases of the kinematic motion.

## 7.2. GLOBAL PEAK LIFT AND DRAG OBSERVATIONS

For the hovering case, the peak lift/ drag ratio remains the same for both phases of the kinematic motion, both phases implying the clockwise and anti-clockwise rotation of the kinematic motion, because of the symmetric nature of the velocities generated from the kinematics, as evident from the Figure 7.3. It is to be noted that the drag depicted in these graphs are absolute values, thus no negative drag values in the graph.

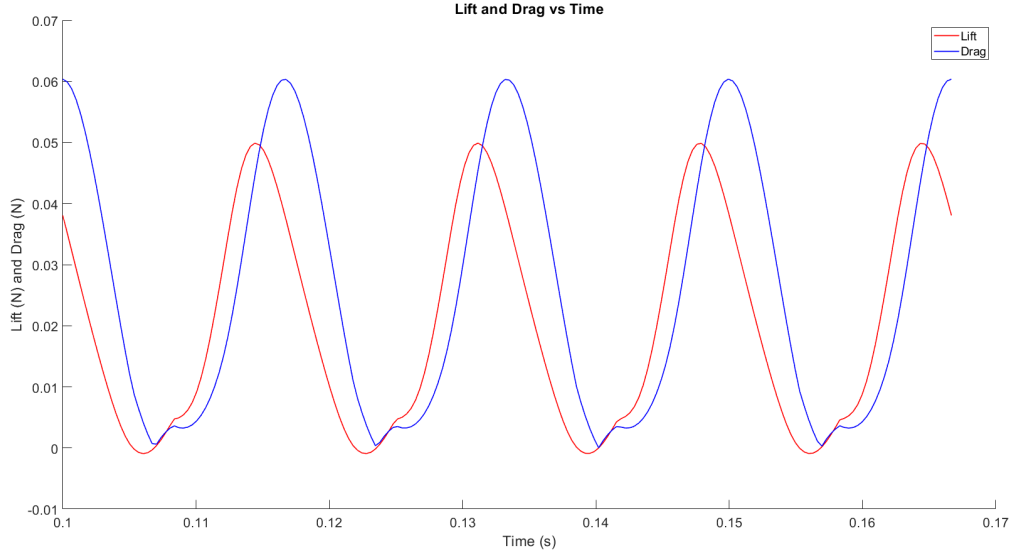


Figure 7.3.: Lift and Drag vs Time for hovering condition

For an additional velocity in the inertial y-axis, the peak lift/ drag ratios vary depending on whether the kinematic motion is against the incoming velocity or with the incoming velocity. This is because, during the kinematic motion when the wing travels along with the additional velocity, the drag observed to be produced is much more than the lift generated leading to the asymmetric peak lift/ drag ratio, even though the lift generated during this phase is also higher than that of the kinematic motion against the flow velocity. When the direction of the same additional velocity is reversed, the peak lift/ drag ratios are mirrored, as now the other phase of the kinematic motion makes the wing move along with the additional velocity. For an additional velocity of 3 m/s in the inertial y-axis, the peak lift/ drag ratio with the flow was 0.746, and against the flow was 0.936, implying more drag in one kinematic phase compared to the other, i.e., when the wing travels along with the additional velocity. Thus the inference when the additional velocity is purely in the inertial y-axis is that the peak lift/ drag is lower when with the flow, and higher when against the flow, but in both phases, the peak drag is more than the lift.

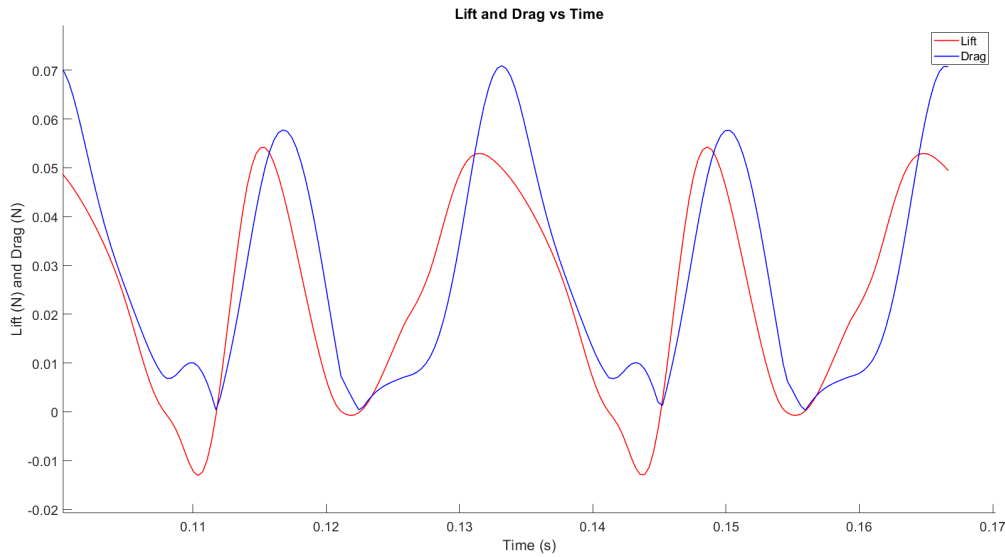


Figure 7.4.: Lift and Drag vs Time for additional 3 m/s in inertial y-axis

For an additional velocity in the inertial z-axis, the peak lift/ drag ratios during both phases of kinematic motion are symmetric, since this additional velocity does not asymmetrically affect the kinematics of the wing motion. For lesser magnitudes of additional velocities in the inertial z-axis, the peak lift/drag ratios are less than 1, but more than the hovering condition, meaning the peak lift produced during both phases keeps increasing compared to the drag. This follows the explanation in the section 6.1.2, wherein when the magnitudes of additional velocities are less compared to the kinematic velocities, the results observed are comparable to the hovering condition. For considerably high values of magnitudes, the peak lift produced during both strokes is more than the peak drag. For an additional velocity of -3 m/s in the inertial z-axis, the peak lift/ drag ratio is 1.0621 during both with and against the flow. These observations are well illustrated in Table 7.4

When the orientation of this additional velocity is changed in a way so that the velocity has components in both the y-axis and the z-axis, observations on the peak lift/ drag show that depending on the orientation, the phases of kinematic motion produce different peak lift/ drag ratios because of the varying influence of the 'y' and 'z' components of the additional velocity. Thus depending on the requirement, an optimum orientation can be found to suit the peak lift and drag produced from the kinematic cycle. For the same additional velocity of 3 m/s, and for a requirement to produce more drag in one phase of the kinematic cycle and more lift in the other phase of the kinematic cycle, the optimum orientation is observed to be at  $37^\circ$  to the inertial negative z-axis, where the peak lift/ drag ratio during one phase was 0.88 and during the other phase was 1.132, signifying more drag during one phase and more lift during the other. The optimum orientation depends on the magnitude of the incoming velocity and the requirement. These observations are given in Table 7.5

From Table 7.5 it is also observed that the influence of the z-component of the additional velocity on the peak lift/ drag ratio is higher when the wing is along the direction of additional velocity, meaning during this phase of kinematic motion, the orientation of the additional velocity in the inertial z-axis influences the lift production the most compared to the phase where the wing is against the additional velocity direction. As orientation in the negative z-axis increases, the peak lift produced during the phase along with the flow also increases, whereas the effects during the other phase are meager. The severity of this effect increases with an increase in the magnitude of incoming velocity. The observed lift and drag graphs for various orientations of an additional velocity of 3 m/s between the positive y-axis and the negative z-axis are included in the appendix.

Peak Lift/ Drag ratio		
Additional velocity case	Peak L/D against the flow	Peak L/D with the flow
Hovering condition (additional velocity of 0 m/s)	0.827	0.827
Additional velocity of 0.5 m/s in inertial y-axis	0.855	0.795
Additional velocity of 3 m/s in inertial y-axis	0.936	0.746
Additional velocity of -3 m/s in inertial y-axis	0.746	0.936
Additional velocity of -0.2 m/s in inertial z-axis	0.837	0.837
Additional velocity of -3 m/s in inertial z-axis	1.0621	1.0621

Table 7.4.: Peak lift/ drag ratios for increasing additional velocities in the inertial y-axis and z-axis

Peak Lift/ Drag ratio		
Additional velocity of 3m/s	Peak L/D against the flow	Peak L/D with the flow
Purely in the inertial y-axis	0.936	0.746
Oriented 25° to the inertial y-axis	0.86	0.957
Oriented 37° to the inertial y-axis	0.8566	1.0487
Oriented 53° to the inertial y-axis	0.88	1.132
Oriented 65° to the inertial y-axis	0.921	1.15
Purely in the inertial -z-axis	1.0621	1.0621

Table 7.5.: Peak lift/ drag ratios for 3m/s additional velocity in both the inertial y-axis and z-axis

### 7.3. Observations on passive pitching motion changes

As in the Q. Wang model, the updated model computes the passive pitching motion and uses prescribed sweeping and heaving motion. Thus the presence of the additional velocities should affect the computed passive pitching motion compared to the hovering condition, by influencing the computed total torque about the  $x_c$  axis. The observed results of the computed passive pitching motion for varied additional velocity cases are in accordance with the above statement, where depending on the magnitude and direction of the additional velocity, the passive pitching angle varies accordingly. This section discusses those observed changes in the passive pitching motion, for the flapping frequency of 30 Hz and elastic hinge stiffness of 10 e-04 Nm/rad.

The major observation is that additional velocity in the inertial y-axis affects the pitching motion angle when the wing changes its pitching stroke along with the direction of incoming additional velocity. Thus the additional velocity in the inertial y-axis makes the pitching motion asymmetric and this effect is

mirrored when the additional velocity is in the opposite direction. The observed asymmetric pitching motion exhibits a short interval of stalling when the pitching stroke reversal happens at the time the sweeping motion is along the additional velocity direction. This effect is observed to be increasing, when the magnitude of the additional velocity opposing the kinematic cycle in the inertial y-axis increases. This effect of temporary stalling of the passive pitching angle is shown in Figures 7.5 and 7.6.

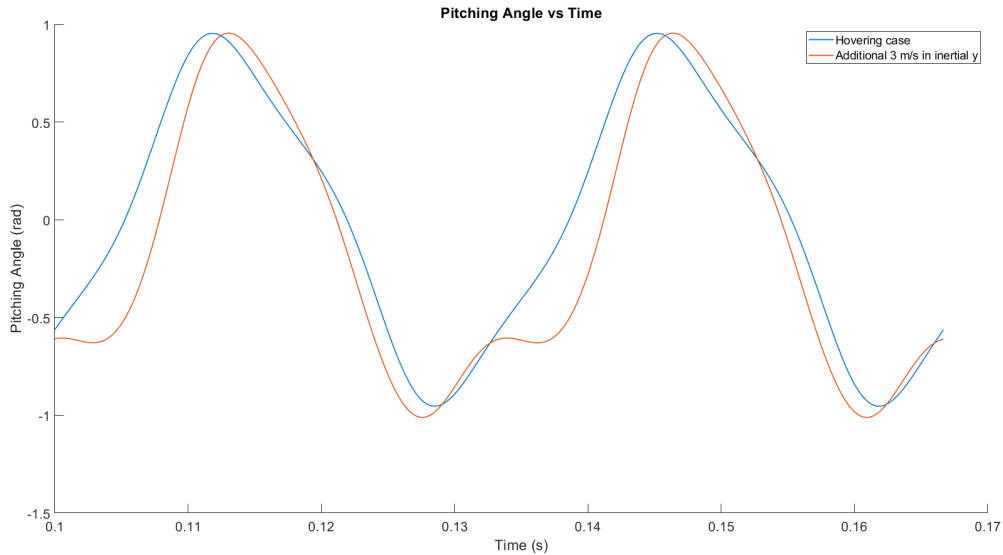


Figure 7.5.: Pitching Angle differences for additional velocity in inertial y-axis

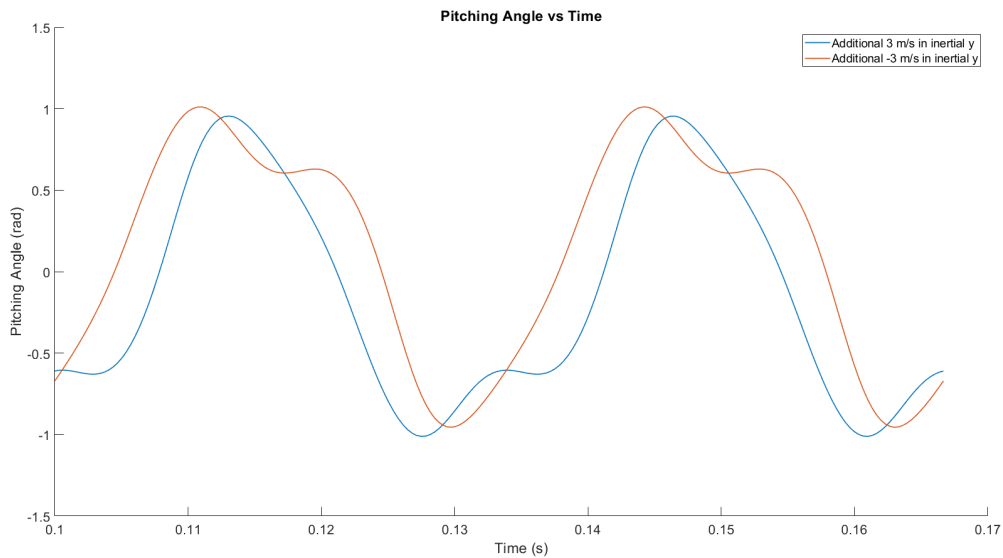


Figure 7.6.: Pitching Angle differences for additional velocities in opposite directions in inertial y-axis

A possible reason for this peculiar observation is deduced to be due to very high aerodynamic torques about the  $x_c$  axis at the time the passive pitching motion appears to stall. This affects the computation of the passive pitching motion which uses the equation of motion given by the Equation 3.27. This effect is also observed when the additional velocity is in the opposite direction, where now the total aerodynamic torque about the  $x_c$  axis is very high in the other phase of the kinematic cycle, thus leading to the observed stalling in the passive pitching motion.

This effect is also observed when looking at the angular velocity of the wing about the  $x_c$  axis, which is  $\omega_{x_c}$ . The angular velocity about  $x_c$  axis gives an indication of the pitching motion, since pitching is basically the rotation about the  $x_c$  axis, as explained in section 2.1.2. At the same instance where the passive pitching motion seems to stall,  $\omega_{x_c}$  is observed to be reducing in magnitude and approaching zero even though the passive pitching stroke has reversed, thus not following a continuous increase in magnitude after the change of pitching stroke as in the hovering condition but rather sudden decrease in magnitude of angular velocity indicating stalling. This reduction in the angular velocity after pitching stroke reversal is observed to stop at the same instance where the passive pitching motion seem to recover from the stalling. This observed effect in the angular velocity  $\omega_{x_c}$  is illustrated in the Figure 7.7

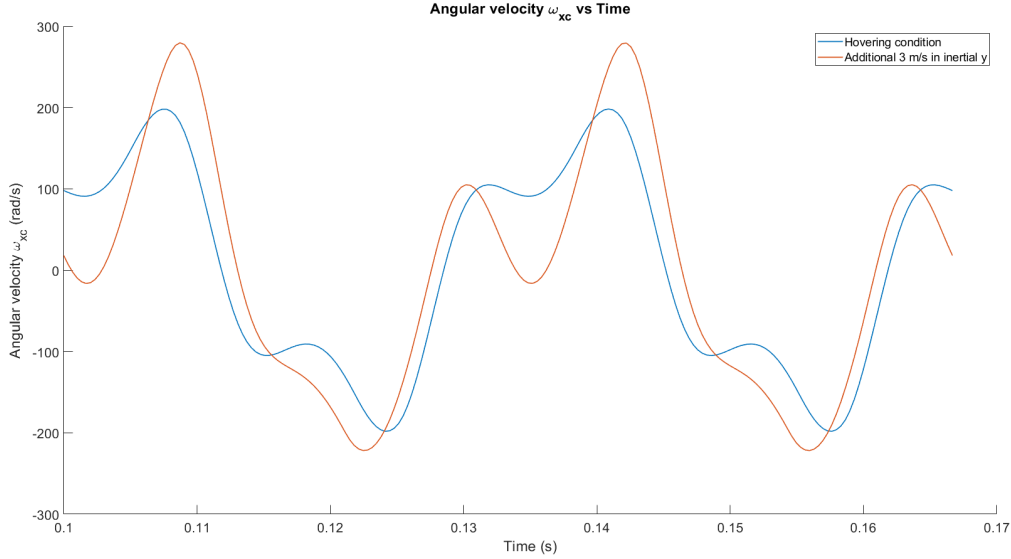


Figure 7.7.: Angular velocity variations for additional velocity conditions

When the same additional velocity of 3 m/s is oriented between the inertial y-axis and z-axis, depending on the component of the additional velocity in the inertial y-axis the effect of temporary stalling of pitching stroke is observed to reduce. This is due to the reduction of the magnitude of the additional velocity in the inertial y-axis when the additional velocity is oriented more to the inertial z-axis, which directly affects the angular velocity about  $x_c$  axis which affects the calculation of the passive pitching. Graphs that illustrate the comparison of pitching angle with the case of additional velocity purely in the inertial y-axis are added in the appendix section. Another interesting observation made is looking at the aerodynamic lift and drag produced during this period of temporary stalling. It is noted that the aerodynamic lift and drag produced during this time is higher compared to the hovering condition, when the temporary stalling of the pitching angle takes place, due to the wing travelling along with the additional velocity direction during this phase, and the pitching angle during this phase being close to maximum. This is evident from Figure 7.4.

Thus from these observations it is concluded that in the presence of additional velocities in the inertial y-axis, there appears to be a presence of temporary stalling in the pitching motion when the pitching stroke changes during the period at which the wing travels along with the direction of additional velocity. And it is noted that this effect is highly influenced by the choice of the elastic hinge stiffness, as explained in sections 7.4.

## 7.4. Observations on the elastic hinge stiffness dependence

Section 3.4 explains the influence of the elastic hinge stiffness, ' $k_\eta$ ' on the calculation of the passive pitching motion, where the elastic hinge stiffness is used to compute the elastic torque, and the elastic torque

is a part of the equation of motion used to compute the passive pitching motion. This is explained in Equation 3.27. The elastic torque together with the aerodynamic torque equates to the applied torque, thus studying the influence of the elastic torque along with the various aerodynamic torques induced by additional velocity conditions reveals interesting observations on the computed passive pitching motion. Thus this section observes and analyses the influence of the elastic hinge stiffness on the passive pitching motion.

The same flapping frequency of 30 Hz is employed for observations in this section. Figure 7.8 illustrates the passive pitching motion angle comparison for the hovering condition for different elastic hinge stiffness of  $7 \text{ e-}04 \text{ Nm/rad}$ ,  $8.5 \text{ e-}04 \text{ Nm/rad}$  and  $10 \text{ e-}04 \text{ Nm/rad}$ . It can be inferred from Figure 7.8 that a lesser value of elastic hinge stiffness allows for higher pitching angles.

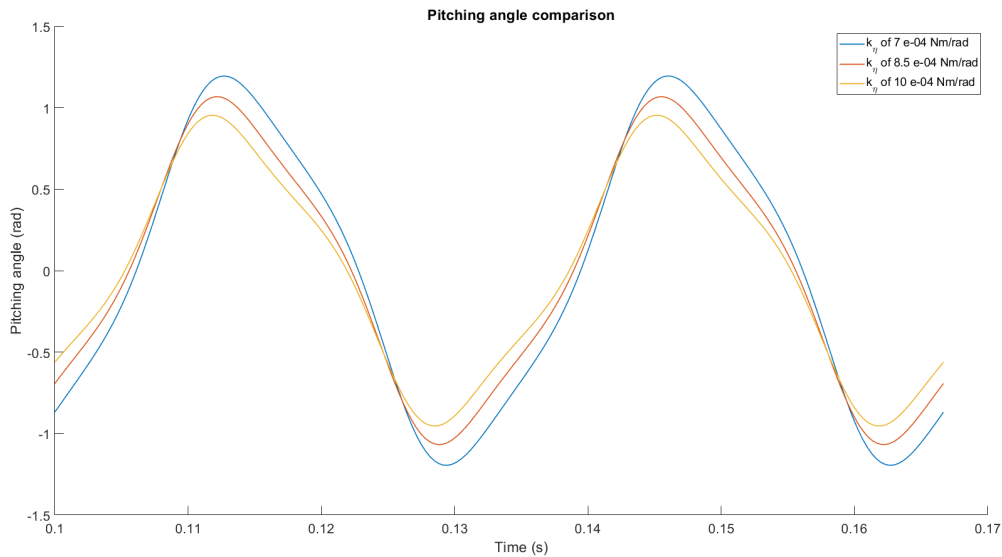


Figure 7.8.: Pitching angle comparison for different  $k_\eta$  for hovering condition

The aerodynamic torque produced during the kinematic cycle is influenced by the additional velocity condition, and the produced aerodynamic torque is asymmetric as explained in Sections 7.2, 7.1, 7.3. Having different elastic hinge stiffness means the elastic torque computed is different, thus leading to different applied torques which is a combination of elastic torque and aerodynamic torque. Thus the effect of the same additional velocity on the passive pitching motion is different for different elastic hinge stiffness, as illustrated in Figures 7.9, 7.10 and 7.11, where the additional velocity case used is an additional velocity of 3 m/s in the inertial y-axis.

#### 7.4. OBSERVATIONS ON THE ELASTIC HINGE STIFFNESS DEPENDENCE

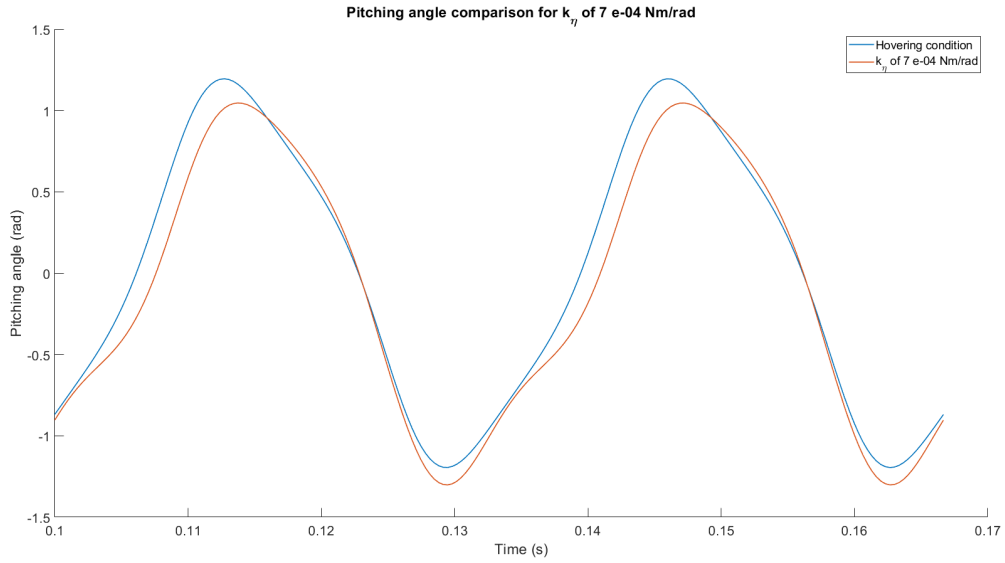


Figure 7.9.: Pitching angle comparison for  $k_\eta$  of 7 e-04 Nm/rad

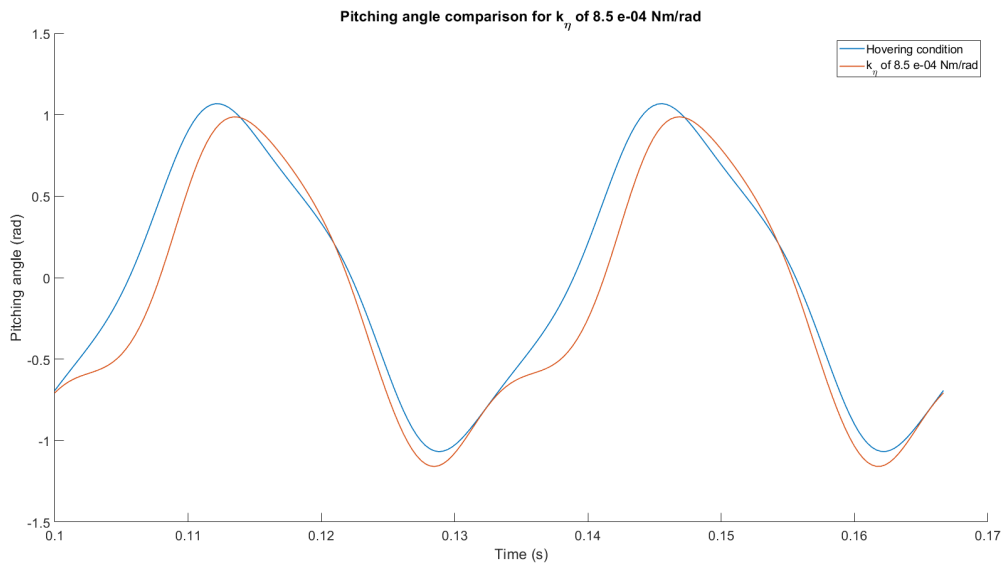


Figure 7.10.: Pitching angle comparison for  $k_\eta$  of 8.5 e-04 Nm/rad

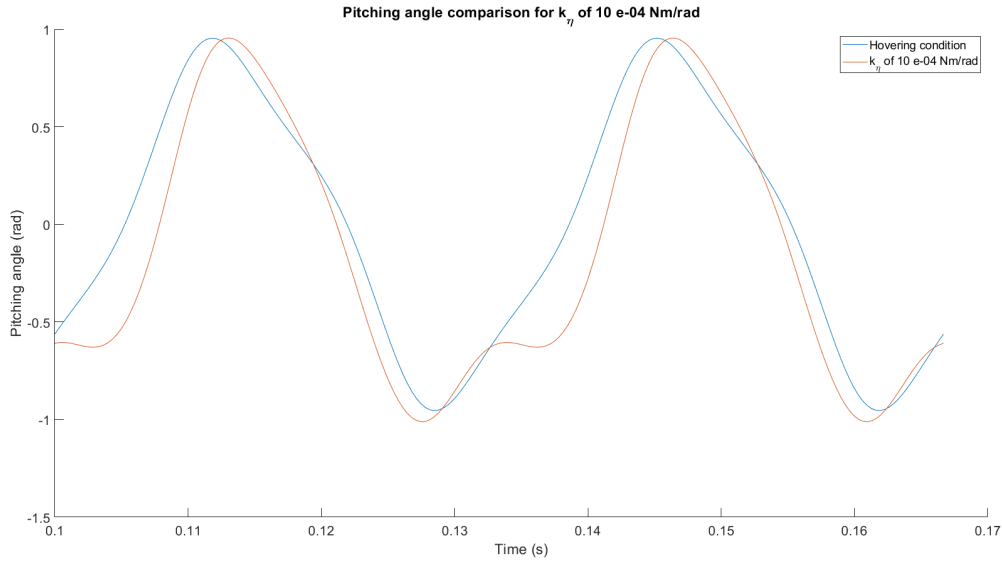


Figure 7.11.: Pitching angle comparison for  $k_\eta$  of  $10 \text{ e-}04 \text{ Nm/rad}$

From Figures 7.9, 7.10 and 7.11 it is evident that the effect of temporary stalling as explained in Section 7.3 is lesser at lesser values of  $k_\eta$  and this effect increases as the value of  $k_\eta$  increases for the same magnitude of additional velocity. This is attributed to the low values of elastic torques produced by lesser  $k_\eta$  values thus the applied torque value is not extremely high in the Equation of motion 3.27 when the pitching stroke reversal happens at the time the sweeping motion is along the additional velocity direction, leading to no stalling in computed passive pitching angle. This effect of temporary stalling in the pitching angle increases for increasing magnitudes of additional velocity in the inertial y-axis, and the significance of influence is higher for higher elastic hinge stiffness values.

Thus it can be concluded that the value of chosen elastic hinge stiffness for a given flapping frequency influences the effect of temporary stalling produced in the pitching angle, and lesser values of elastic hinge stiffness are better to avoid this effect being present in additional velocity conditions.

## 7.5. Observations on the influence of flapping frequency

As explained in section 4.3, a fixed flapping frequency of 30 Hz is used for all the observations made in this research work. But the aerodynamic loads produced on the wing are highly dependent on the flapping frequency of the wing, as evident while comparing the lift and drag produced in hovering condition for different flapping frequencies. Figures 7.12, 7.13 and 7.14 illustrate the influence on lift, drag and pitching angles for different flapping frequencies, for a given elastic hinge stiffness.

## 7.5. OBSERVATIONS ON THE INFLUENCE OF FLAPPING FREQUENCY

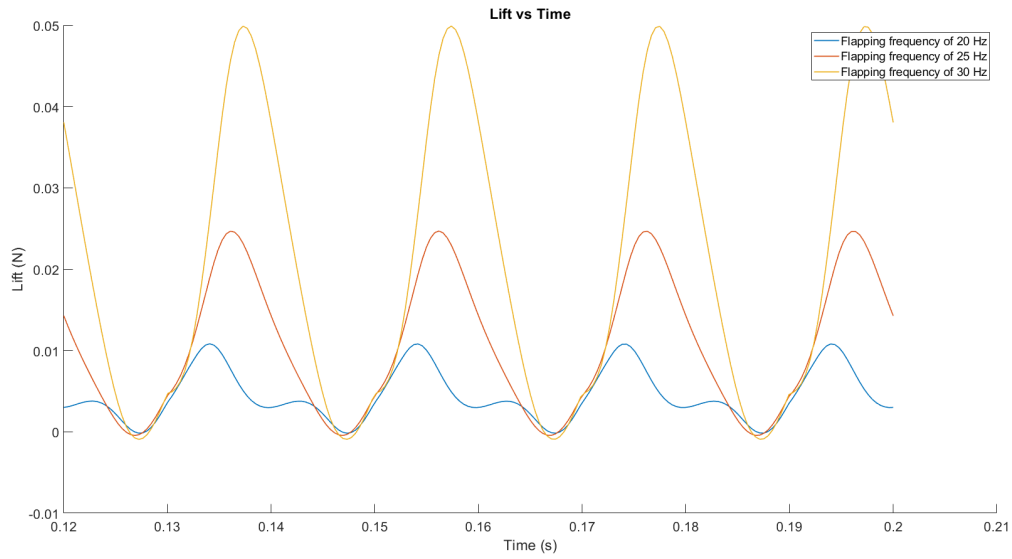


Figure 7.12.: Lift produced for different flapping frequencies in hovering condition

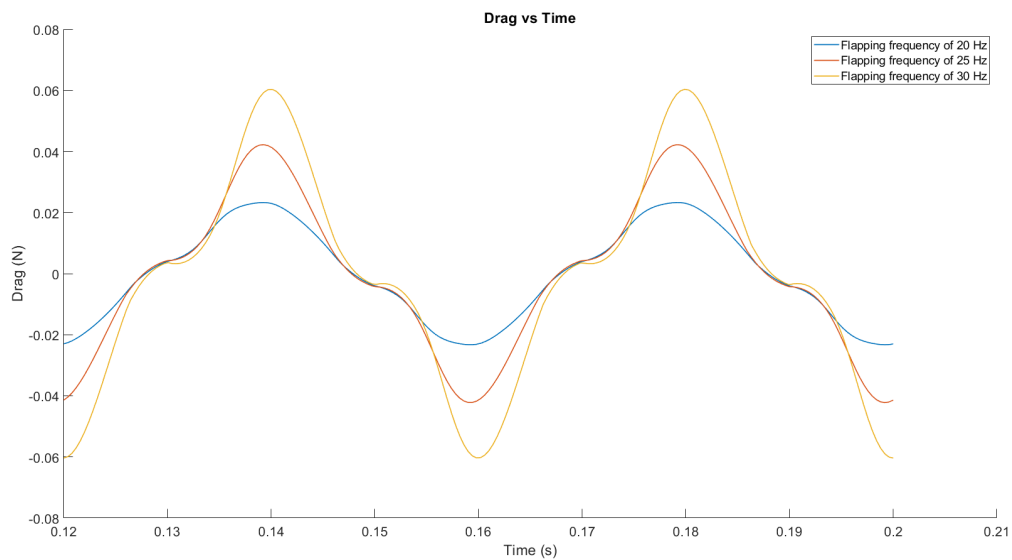


Figure 7.13.: Drag produced for different flapping frequencies in hovering condition

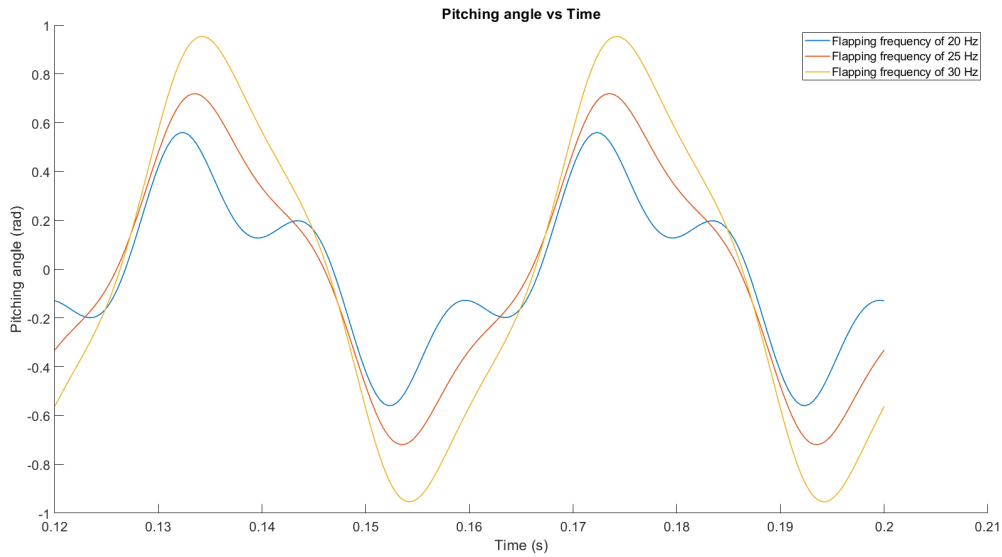


Figure 7.14.: Pitching angles for different flapping frequencies in hovering condition

It can be seen that, for lesser values of flapping frequency and for the same elastic hinge stiffness, the lift and drag values produced are lesser compared to the values produced by higher flapping frequencies for the same elastic hinge stiffness. This is because of the lesser values of kinematic velocities produced by the wing in lesser flapping frequency conditions, leading to lesser aerodynamic loads on the wing. This observation can also serve as a method for validation of the updated model, where the concept of more aerodynamic loads on the wing when the resultant velocities on the wing are higher hold true, when the wing travels along with the direction of the additional velocity.

Looking at the pitching angles for different flapping frequencies, it is clear that the pitching angles are higher and more stable when the flapping frequency increases for the same elastic hinge stiffness value. It is to be noted that, as explained in section 4.3, the selected elastic hinge stiffness value is the maximum of the range used by Q. Wang[1], which might affect the lower flapping frequency results.

For additional velocity conditions, depending on the flapping frequency and the selected elastic hinge stiffness, the influence of the additional velocity on the resultant translational velocity, and thus the total aerodynamic loads vary, since for lesser flapping frequencies the kinematic velocities produced by the wing are lesser. An additional velocity of 3 m/s in the inertial y-axis is used to observe the influence of various flapping frequencies on the generated aerodynamic lift and drag. Three flapping frequencies of 20 Hz, 25 Hz and 30 Hz were employed to make the observations on the influence of the said additional velocity condition. Figures 7.15 and 7.16 compare the lift produced between the hovering condition and the additional velocity condition of 3 m/s for flapping frequencies of 25 Hz and 30 Hz. Graphs that compare the hovering condition and the additional velocity condition of 3 m/s for the three above mentioned flapping frequencies for the results of lift, and drag produced are illustrated in the appendix section.

## 7.5. OBSERVATIONS ON THE INFLUENCE OF FLAPPING FREQUENCY

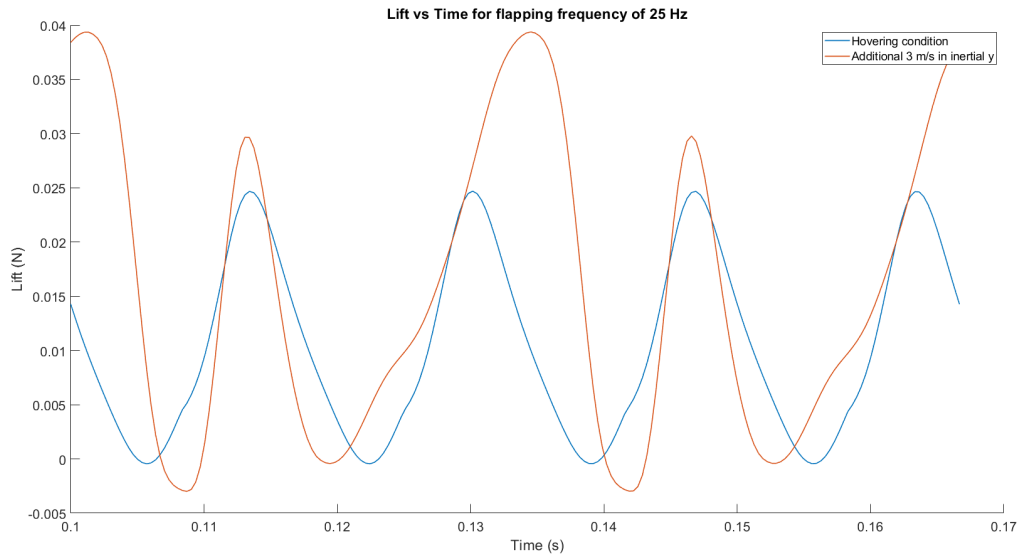


Figure 7.15.: Lift vs time for flapping frequency of 25 Hz

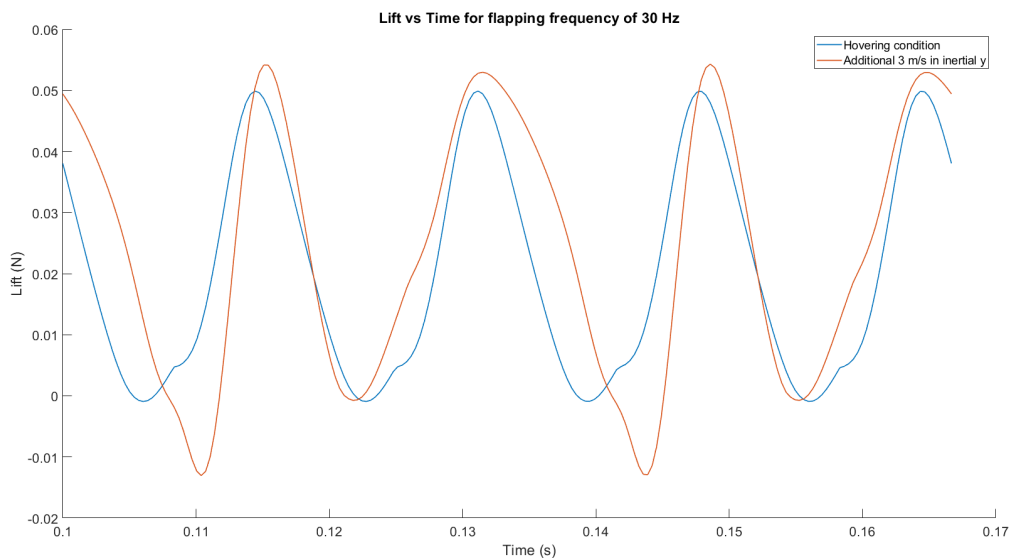


Figure 7.16.: Lift vs time for flapping frequency of 30 Hz

Figures 7.15 and 7.16 clearly indicate that the significance of the influence of the same additional velocity is higher when the flapping frequency is lower, because of the lesser kinematic velocities produced at lesser flapping frequencies. This can be observed by looking at the comparison of average lift and drag produced between hovering and additional velocity conditions for different flapping frequencies, given by Tables 7.6, 7.7 and 7.8

Thus it can be concluded that the significance of influence of the additional velocity on the aerodynamic lift and drag of the flapping flight increases as the flapping frequency reduces for a given high value of elastic hinge stiffness.

Average lift and drag values		
Flapping frequency of 20 Hz	Average lift (N)	Average drag (N)
Hovering condition	0.0045	-1.1528 e-04
Additional velocity of 3 m/s in inertial y-axis	0.0094	-0.0109
% variation compared to hovering condition	208.8%	9455.23%

Table 7.6.: Average lift and drag produced for flapping frequency of 20 Hz

Average lift and drag values		
Flapping frequency of 25 Hz	Average lift (N)	Average drag (N)
Hovering condition	0.0105	-2.0691 e-04
Additional velocity of 3 m/s in inertial y-axis	0.0158	-0.0087
% variation compared to hovering condition	150.47%	4204.72%

Table 7.7.: Average lift and drag produced for flapping frequency of 25 Hz

Average lift and drag values		
Flapping frequency of 30 Hz	Average lift (N)	Average drag (N)
Hovering condition	0.0205	-3.0193 e-04
Additional velocity of 3 m/s in inertial y-axis	0.024	-0.0078
% variation compared to hovering condition	117.07%	2583.38%

Table 7.8.: Average lift and drag produced for flapping frequency of 30 Hz

## 7.6. Observations on translational force and translational velocities

As explained in the section 6.2, the presence of an additional velocity opposing the kinematics of the wing motion produces asymmetric resultant translational velocity between both strokes, thus resulting in asymmetric translational force production. The translational force in the  $y_c$  equation is set up such that depending on the direction of the velocity in the  $y_c$  direction, the translational force has a direction opposite to it, refer Equation 5.13. This variation in the rate of change of the resultant translational velocity when the wing travels along with the additional velocity or against it leads to an asymmetry in the rate of change of translational force on the wing during the phases of the kinematic cycle. This can be visualized in Figure 7.17.

## 7.6. OBSERVATIONS ON TRANSLATIONAL FORCE AND TRANSLATIONAL VELOCITIES

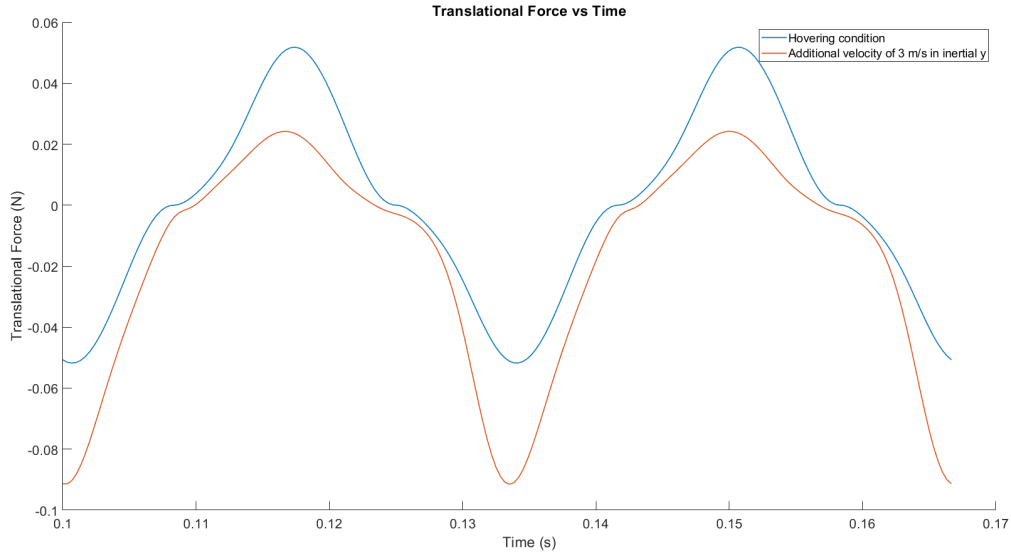


Figure 7.17.: Changes in the rate of change of translational force

Figure 7.17 shows that the rate of change of translational force, thus the rate of change of translational velocity is higher when the wing travels along with the additional velocity and the opposite in the other phase of kinematic cycle. This effect of reduced resultant translational velocity against the flow increases with increase in magnitude of the additional velocity. Thus at a certain magnitude of additional velocity in the inertial  $y$ -axis, the peak translational force observed in the co-rotating frame on the wing when moving opposite to the additional velocity direction is about zero, and the entire translational force profile in the co-rotating frame for this magnitude always has one sign, meaning the direction of  $v_{y_c}$  remains same for the entire kinematic cycle since the sign of the translational force produced depends on the sign of the velocity component  $v_{y_c}$ .

For the selected wing parameters as explained in section 4.3, this magnitude of additional velocity when the entire translational force profile has only one sign is found to be about 5.75 m/s when purely in the inertial  $y$ -axis. This implies that the sign of the translational velocity component  $v_{y_c}$  always remains the same, which theoretically should imply that the sweeping motion should not be possible for additional velocities greater than this magnitude. The resulting translational force graph for an additional velocity of 5.75 m/s purely in the inertial  $y$ -axis is given in Figure 7.18.

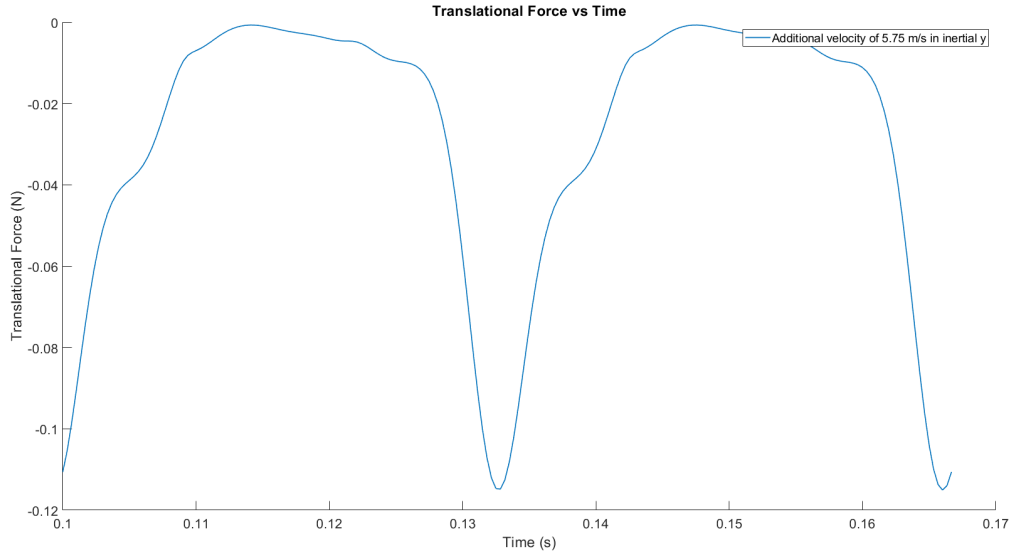


Figure 7.18.: Translational force for an additional velocity of 5.75 m/s in inertial y-axis

### 7.7. Observations along wingspan strips

The presence of additional velocities impact the translational velocities and forces along the wingspan strips, compared to the hovering condition, since depending on the position of the strip in the wingspan, the magnitude of the impact of additional velocity is different. This is because the kinematic velocities at the tip are very high compared to the kinematic velocities of the strips along the wingspan that are near the root. Thus the impact of the additional velocities will be different near the root and at the tip. This leads to translational velocity and force direction differences along the wingspan strips in additional velocity cases, which is not the case in hovering conditions, where at all strips along the wingspan, the direction of translational velocity and translational force are the same. At the extreme cases, this effect can be visualized in Figure 7.19, where the translational force differences along the wingspan strips can be seen.

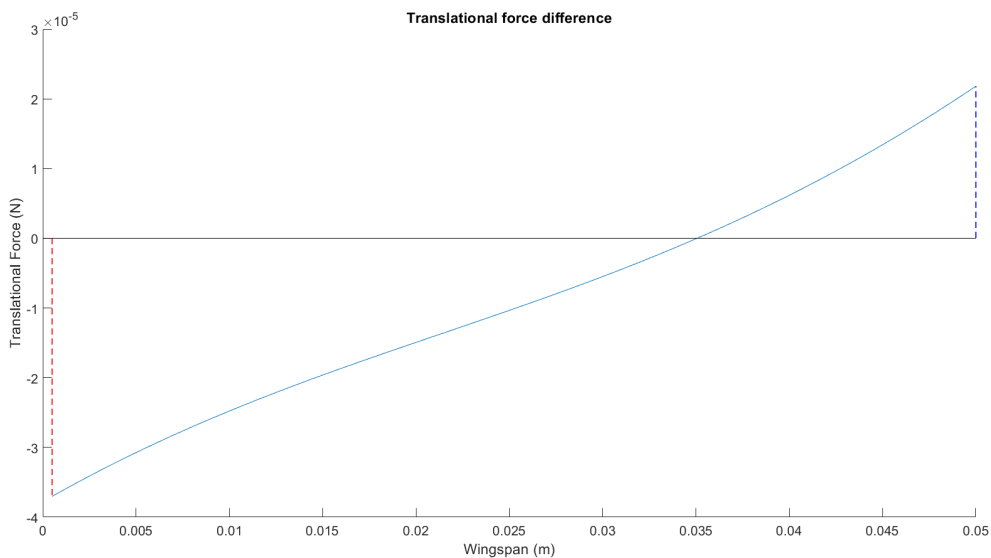


Figure 7.19.: Translational force differences illustration along the wingspan strips

This also leads to the analytical angle of attack differences along the wingspan strips, which is not the case in hovering conditions. The analytical angle of attack discrepancy is due to the varied effect of velocities  $v_{z_c}$  and  $v_c$  at each strip along the wingspan, and also the direction of the resultant translational velocity at each strip along the wingspan, thus the analytical angle of attack varies along the wingspan. The analytical angle of attack difference increases as the magnitude of the additional velocity increase. The reason behind this observation is that the updated model and Q.Wang's model[1] compute the analytical angle of attack from the Equation 3.1, thus individual strips along the wingspan have different ratios of translational velocity leading to the analytical angle of attack changes along the wingspan.

The main reason for these observations are to highlight the importance of calculating the load equations and angle of attack at each wingspan strip by calculating all variables inside the integration loop, explained in Section 5.3 and thus to use the blade element method in the correct manner, rather than to incur physical meanings from these observations. This is because, finally the total load on the wing is computed for aerodynamic load calculations since the wing travels as a whole and not as individual strips.

## 7.8. Observations on computational time

A minor observation is made on the computational time of the updated model versus the computational time of Q. Wang's model to observe the effect of load calculations at each strip along the wingspan by calculating all variables inside the integration loop as explained in Section 5.3. This is done so since Q. Wang's model was aimed for use in optimization problems, thus an increase in computational time works against that idea. But, as explained in section 5.3, it is necessary to make calculations at each strip along the wingspan using the updated method. Thus a trade-off on the computational time has to be made while updating the model. The observed computational time differences between the two models for the hovering condition, when both models use the same input parameters are given below. It is to be noted that these observations were done to include an iteration of different flapping frequencies and elastic hinge stiffness to highlight the computational differences in a better way.

- Computational time for Qi Wang model - 115.04 s
- Computational time for updated model (hovering condition) - 550 s
- Computational time for updated model (additional velocity case) - 520 to 630 s, depending on the velocity condition

It can be seen that for the hovering condition, the computational time for the updated model is almost 5 times the computational time for Qi Wang model that produces the same results. Thus it is very inefficient to use the updated model for the hovering case, but the trade-off in computational time has to be done to calculate for additional velocity conditions. A potential future work could involve optimizing this updated model to reduce computational time.



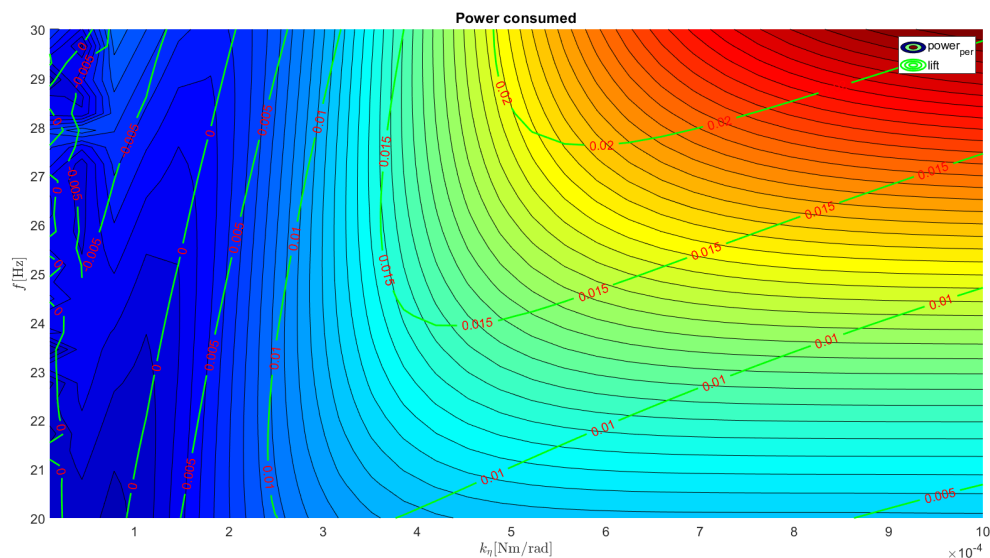
## 8. Discussions

This section discusses on the observations that were made in the updated model but those which were not analyzed in detail since these were outside the scope of this thesis work. These discussions mainly build on ways to improve the model to eliminate the hard bound constants that were employed in this research work, such as using a fixed flapping frequency and elastic hinge stiffness, weight of the wing etc., These discussions provide valuable information on potential future work that can be done as a continuation of this thesis work.

### 8.1. Discussions on the power calculations

One of the important research work of Q. Wang[1] was to design power efficient flapping wings for the hovering condition. This involved computing the power during the flapping cycle by considering three components: Aerodynamic power to overcome aerodynamic drag, inertial power to accelerate the wing and surrounding fluid, and elastic power due to the resistance from the elastic spring.[1] Then by analyzing for different conditions, such as different flapping frequencies while varying elastic hinge stiffness, the optimum power was calculated for the hovering condition, and the corresponding flapping frequency and elastic hinge stiffness were found as the optimum values to have for efficient power consumption.

For hovering condition, the power consumed for different flapping frequencies and elastic hinge stiffness is given by the Figure 8.1, which illustrates the lift produced at those flapping conditions as well. Thus theoretically, for a required lift value, an optimum flapping frequency and elastic hinge stiffness can be found such the resulting flapping flight under hovering condition is the most power efficient.



**Variation in power consumed during the phases of the kinematic cycle:**

As discussed, a component in the power consumption calculation during the kinematic cycle is the aerodynamic power, which takes into account the aerodynamic drag. And as discussed from the observations in Chapter 7, the aerodynamic drag is higher during the phase when the wing travels along with the additional velocity, and the aerodynamic drag is lower during the phase when the wing travels against the additional velocity. Thus in the presence of additional velocity, the aerodynamic drag produced is asymmetric during the phases of the kinematic cycle, leading to asymmetric power consumed during the kinematic cycle. Future work may study the difference in power consumed during the kinematic cycle for various additional velocity conditions, which may provide insights on the control required for maintaining flight for these additional velocity conditions and for forward flight.

**Power efficient flight for additional velocity conditions**

Chapter 7 observes that the presence of additional velocities influence the average lift and drag produced, and that the orientation of the additional velocity also play a huge influence on the produced lift and drag. Thus theoretically for different additional velocity conditions and the different orientations, the amount of power consumed and the optimum conditions for power efficient flight varies depending on the additional velocity and its orientation. Thus different graphs, like Figure 8.1 can be made for different velocity conditions, from which the resulting power consumed can be studied. Future work might study the power consumed and the power efficient flight conditions for different additional velocity conditions.

**8.2. Discussions on optimal pitching axis**

Q. Wang's work[1] also works on finding the optimal pitching axis for the passive pitching motion during the hovering condition. This was done by setting up an optimization model to investigate the influence of the pitching axis location on the power efficiency. This was done by optimizing the parameters  $\hat{d}_r$  and  $\hat{d}_t$ , where these parameters defined the pitching axis location. The objective of this optimization model was to find the optimum values of  $\hat{d}_r$  and  $\hat{d}_t$ , so that the power consumed was the least to produce the same lift requirement. It was concluded in that work [1] that the amount of power that can be saved was at least 21% for QE-wings.

For this research work, to reduce complexity, the  $\hat{d}_r$  and  $\hat{d}_t$  parameters were set as zero, meaning the straight leading edge (LE) is used as the pitching axis. Thus a potential future work would involve using the same optimization to optimize the parameters  $\hat{d}_r$  and  $\hat{d}_t$ , to find the optimal pitching axis for different additional velocity conditions. Since this optimization model works on finding the least power consumed to produce the same lift requirement, and as discussed in section 8.1, the power consumed and the optimum flight conditions on the power consumed may depend on the additional velocity conditions, it is interesting to study the influence of the optimal pitching axis on the power consumption. Interestingly, it is fair to assume that the optimal pitching axis location would be different during the phases of the kinematic cycle in additional velocity conditions, since the aerodynamic drag and hence the aerodynamic power consumed would be different during the phases. Hence a detailed study on this topic would provide huge insights on obtaining the most power-efficient flight for different additional velocity conditions.

# 9. Conclusions and Recommendations

## 9.1. Conclusions

This research aimed at updating the aerodynamic quasi-steady model of Q.Wang[1] for additional velocity conditions and to make observations of the updated model for various additional velocity conditions to incur insights on the load changes for varied additional velocity conditions. This work proposes a method to update the model and analyses the observations made. The research answers the following sub-questions as:

*1. How to update the quasi-steady aerodynamic model for additional velocity conditions?*

To incorporate the additional velocities in the quasi-steady aerodynamic model, the resultant translational velocity on the wing is computed by the proper vector addition of the additional velocity with the kinematic velocity of the wing. This is done by transforming the additional velocity in the inertial frame of reference to the co-rotating frame of reference by using the inverse of the total rotation matrix. After the transformation, the additional velocity components ' $v_{y_c,add}$ ' and ' $v_{z_c,add}$ ' are added with kinematic velocity components ' $v_{y_c}$ ' and ' $v_{z_c}$ ' to compute the resultant translational velocity ' $v_{c,res}$ ' on the wing. The updated translation-induced loads uses ' $v_{c,res}$ ' and the updated coupling-induced loads uses ' $v_{z_c,res}$ '. The setting up of the updated quasi-steady aerodynamic model equations are explained in Chapter 5 in detail.

The updated quasi-steady aerodynamic model computes the aerodynamic loads at all wingspan strips individually, by using all variables inside the integration loop and then the sum of these individual loads would give the total (global) aerodynamic load on the wing. This is done to account for the varied influence of the additional velocity at different strips along the wingspan on all variables in the aerodynamic equations. This is explained in detail in Sections 5.3 and 7.7. The updated model was verified to produce logical results and affirmed with literature conclusions as explained in Chapter 6.

*2. What observations are made from the updated quasi-steady aerodynamic model for various additional velocity conditions?*

A plethora of observations were made from the updated quasi-steady aerodynamic model for various additional velocity conditions with different orientations in the inertial frame of reference and the observations were analysed to incur valuable insights on the behaviour of the resulting aerodynamic loads and the passive pitching motion, which are explained in detail in Chapter 7. The major observations found are:

- The average lift and drag produced are highly influenced by the magnitude and orientation of the additional velocity with respect to the kinematic motion. An additional velocity in the inertial y-axis affects the symmetry of the kinematic motion, thus the average drag values produced in these conditions are considerably higher than the hovering condition, while the average lift value is also higher for increasing magnitudes of additional velocity in the inertial y-axis. An additional velocity in the inertial z-axis influences the average lift generated the most, but does not affect the symmetry of kinematic motion thus the average drag values remain close to the hovering condition. An additional velocity oriented in both axes influence the average lift and drag values depending on the magnitude of the individual components in the respective axis.
- An additional velocity in the inertial y-axis produces asymmetric peak lift/ drag ratios during the phases of the kinematic cycle, depending on whether the wing travels with or against the additional velocity direction. An additional velocity in the inertial z-axis increases the peak lift/ drag ratio in both phases of the kinematic cycle, but the ratio remains symmetric. An interesting observation made is that for certain orientations of the additional velocity in both the inertial y-axis and z-axis,

peak lift is more in one phase of the kinematic cycle and peak drag is more in the other phase, which makes the peak lift/ drag highly asymmetric which is not the case in the hovering condition.

- For a flapping frequency of 30 Hz and a fixed elastic hinge stiffness of  $10 \times 10^{-4}$  Nm/rad, the presence of additional velocities in the inertial y-axis appears to produce an effect of temporary stalling on the passive pitching angle, evident from observing the calculated passive pitching angle, when the pitching stroke changes during the period at which the wing travels along with the direction of additional velocity.
- For a fixed flapping frequency, the influence of chosen elastic hinge stiffness value for additional velocity conditions is observed in this work. It is observed that the value of chosen elastic hinge stiffness influences the effect of temporary stalling produced in the pitching angle for additional velocities in the inertial y-axis, and higher values of elastic hinge stiffness produce a more temporary stalling effect. This effect increases for increasing magnitudes of additional velocities in the inertial y-axis.
- For a fixed elastic hinge stiffness, the significance of influence of the additional velocity on the aerodynamic lift and drag of the flapping flight increases as the flapping frequency reduces, since the kinematic velocities produced by low flapping frequencies are lesser.
- For an additional velocity purely in the inertial y-axis, the rate of change of translational force is asymmetric between the phases of the kinematic cycle, meaning the rate of change of translational velocity is asymmetric in this additional velocity condition. Moreover, it is observed that for a magnitude of about 5.75 m/s in the inertial y-axis, the entire translational force profile has only one sign, meaning the sign of the translational velocity component ' $v_{yc}$ ' always remains the same for magnitudes above 5.75 m/s in the inertial y-axis.
- The computational time for the updated quasi-steady aerodynamic model is about 5 times more than that of Q. Wang model[1] for computing the same results in the hovering condition. This is because of computing the aerodynamic loads at each wingspan strip by calculating all the variables inside the integration loop to account for the proper definition of all analytical equations in additional velocity conditions, as explained in Section 5.3.

## 9.2. Limitations of the updated model

Observations in Section 7.6 reveal that the rate of change of translational velocity (from the rate of change of translational force) is different between the phases of the kinematic cycle depending on whether the wing is with or against the direction of the additional velocity. This theoretically means that there is an induced stroke acceleration variation between the phases of the kinematic cycle due to the interaction of the additional velocity with the kinematic velocity and this effect is not captured in the updated quasi-steady aerodynamic model for added mass induced load calculations.

Calculating the induced stroke acceleration variation would mean that the resultant translational velocity history has to be considered in the quasi-steady model since the rate of change of the resultant translational velocity would give the induced stroke acceleration variation. This is a huge update from the current model which computes all the aerodynamic loads and the passive pitching motion at each timestep and does not consider the history of the velocity values. Future work might work on including this induced stroke acceleration variation in the calculation of the added mass induced loads. Thus it can be observed that this updated quasi-steady aerodynamic model for additional velocity conditions slightly overestimates the added mass loads when the wing travels against the direction of additional velocity and slightly underestimates the added mass loads when the wing travels with the direction of additional velocity.

## 9.3. Recommendations

As with any research work, there is always room for further improvements and investigations. This section gives some recommendations for potential future work in updating the quasi-steady aerodynamic model.

- As explained in the Limitation section 9.2, future work might work on including the induced stroke acceleration variation in the calculation of the added mass induced loads and then study the resulting changes in the aerodynamic loads and the passive pitching motion.
- Experimental validation and CFD validation of the updated quasi-steady model for the analyzed additional velocity conditions would provide valuable insights on the validity of the proposed model and is a possible potential future research work.
- As explained in Chapter 8, the study on the power calculations and the power asymmetry between the phases of the kinematic cycle for additional velocity conditions, and the study on the optimal pitching axis for additional velocity conditions can be a potential research work that can be studied as a continuation of this work.



# A. Appendix

## A.1. Different ways to compute center of pressure, and coefficients of lift, drag, and force

Section 3.3 explains that Q. Wang's model[1] uses different methods to compute the center of pressure, and coefficients of lift, drag, and force. All these different ways can also be used in this updated model since no new variables or new empirical variables are added in the updated quasi-steady aerodynamic model. The updated model uses the analytical method to compute the center of pressure, and the State-space method from Taha et.al.,[22] was used to compute the coefficients of lift, drag, and force, and these are explained in Section 3.3. This appendix section explains the other methods that were also employed in Q. Wang work[1].

**Method from Dickson et.al.,[20] to compute center of pressure:**

$$\hat{d}_{cp}^{trans} = (0.82/\pi) * AOA + 0.05 \quad (A.1)$$

**Method from Han et.al.,[21] to compute center of pressure:**

$$\hat{d}_{cp}^{trans} = 0.005008 * AOA/\pi * 180 + 0.06238 \quad (A.2)$$

**Method of using empirical force coefficients to compute coefficient of lift, drag, and force:**

$$C_L^{trans} = 1.8 * \sin(2 * AOA) \quad (A.3)$$

$$C_D^{trans} = 1.9 - 1.5 * \cos(2 * AOA) \quad (A.4)$$

$$C_{F_{yc}}^{trans} = \sqrt{(C_L^{trans})^2 + (C_D^{trans})^2} \quad (A.5)$$

## A.2. Global peak lift and drag graphs

This section illustrates the graphs that were utilized for the description of the section 7.2. These graphs represent the Lift and Drag vs Time for various additional velocity conditions that were observed in Section 7.2. Figures A.1, A.2 and A.3 illustrate the produced lift and drag values for increasing magnitudes of additional velocities in the inertial y-axis. It is to be noted that the drag values are mentioned as absolute values.

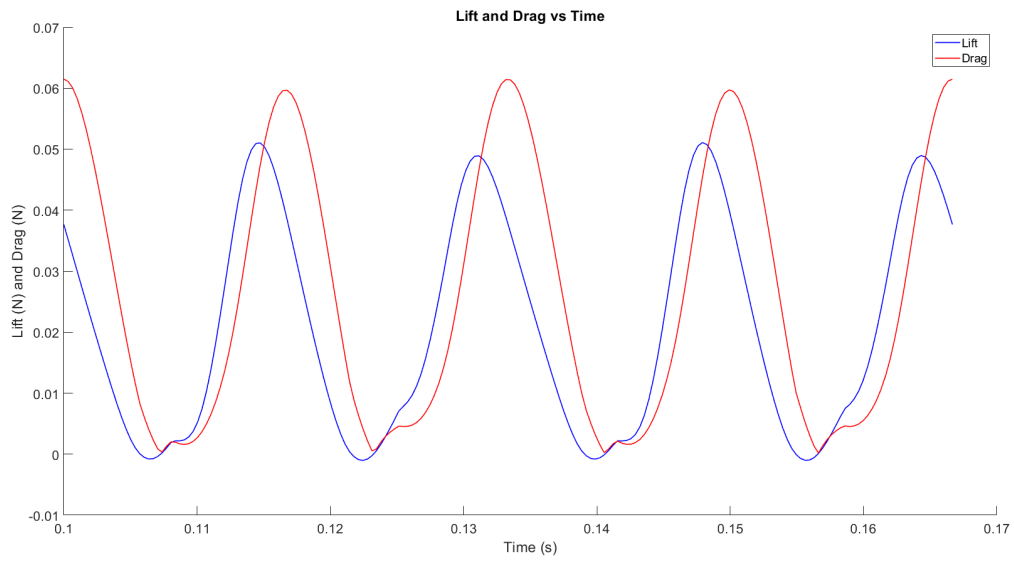


Figure A.1.: Lift and Drag vs Time for additional 0.5 m/s in inertial y-axis

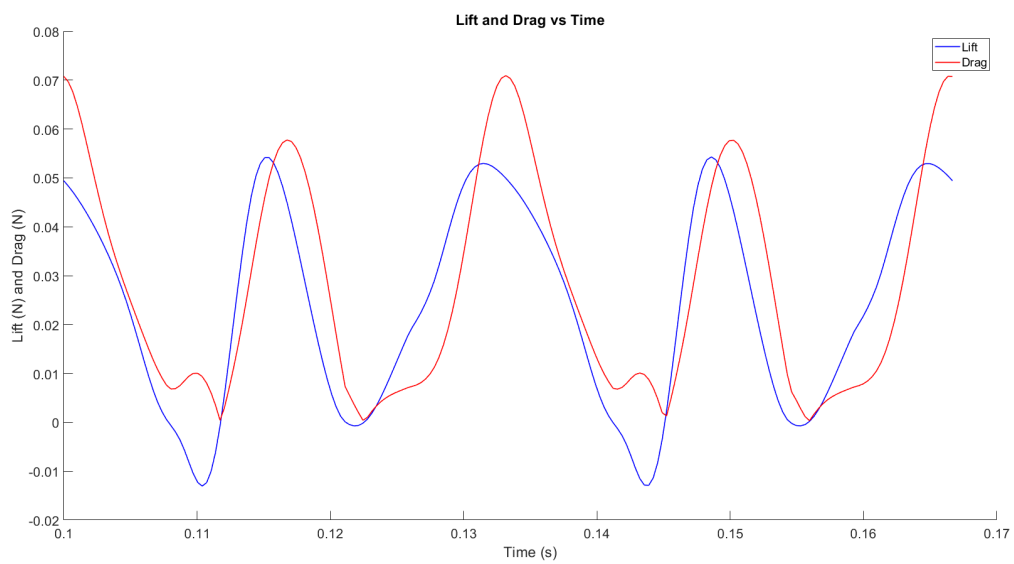


Figure A.2.: Lift and Drag vs Time for additional 3 m/s in inertial y-axis

## A.2. GLOBAL PEAK LIFT AND DRAG GRAPHS

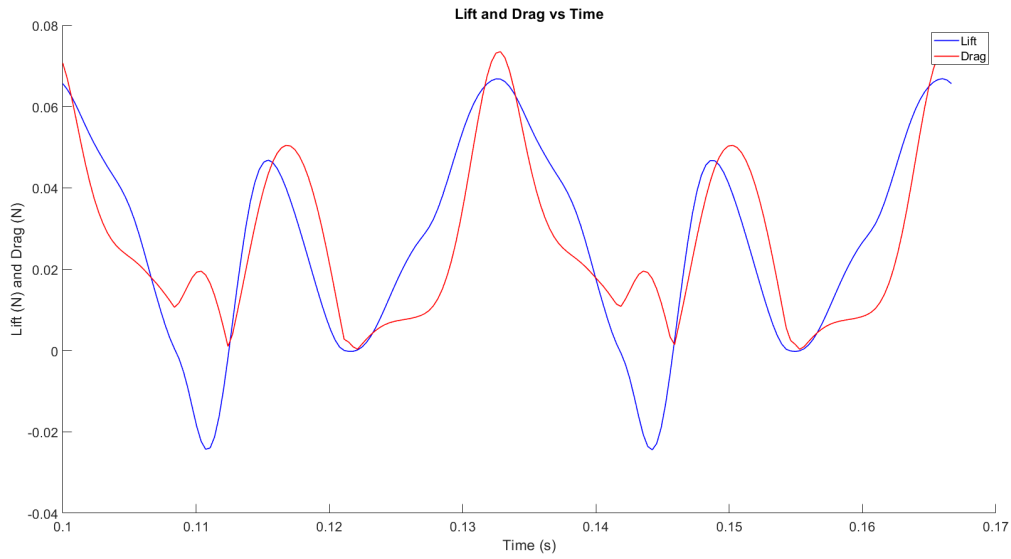


Figure A.3.: Lift and Drag vs Time for additional 5 m/s in inertial y-axis

Figures A.4, A.5 and A.6 illustrate the produced lift and drag values for increasing magnitudes of additional velocities in the negative inertial z-axis. These graphs illustrate that the peak lift/ drag ratio increases for increasing magnitudes of additional velocities in the negative inertial z-axis.

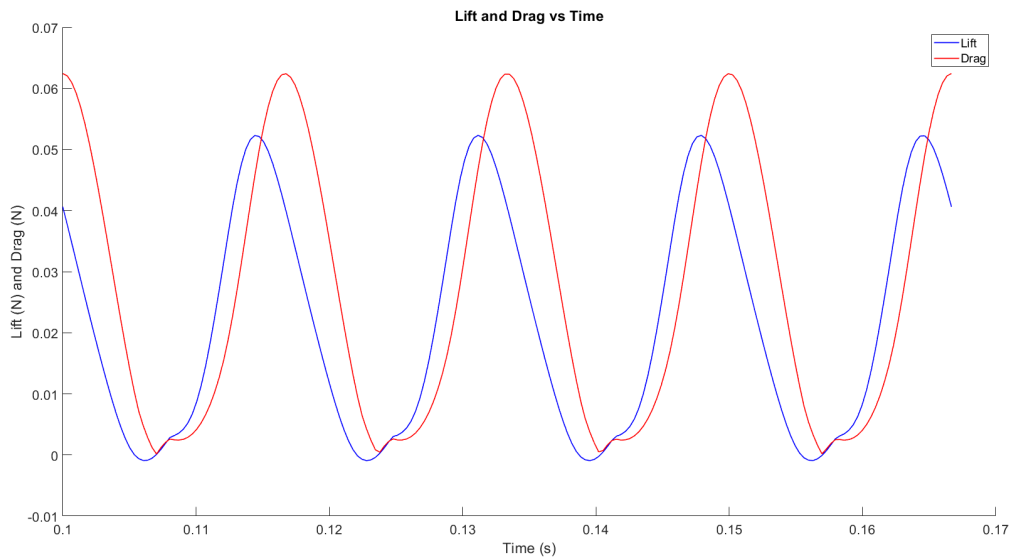


Figure A.4.: Lift and Drag vs Time for additional 0.2 m/s in inertial -z-axis

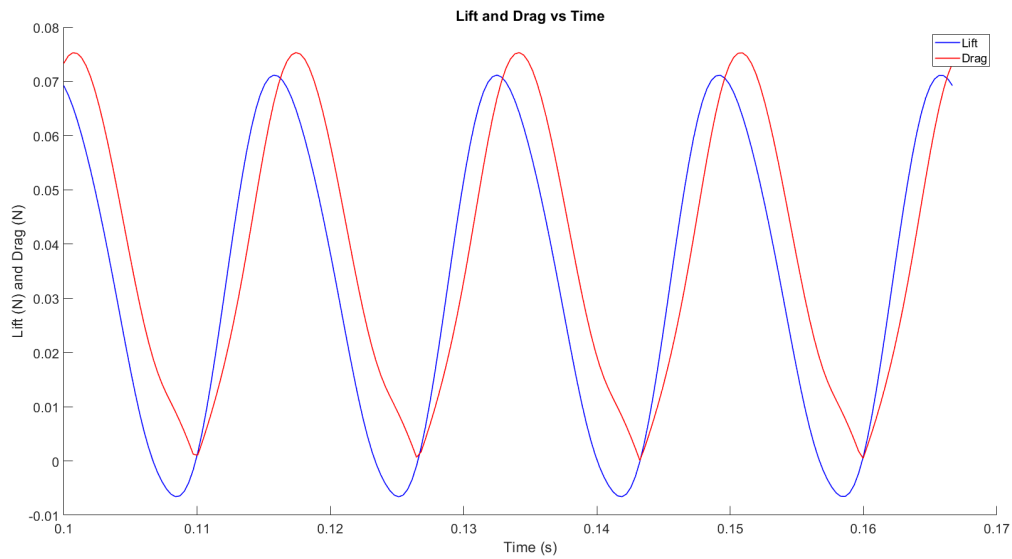


Figure A.5.: Lift and Drag vs Time for additional 2 m/s in inertial -z-axis

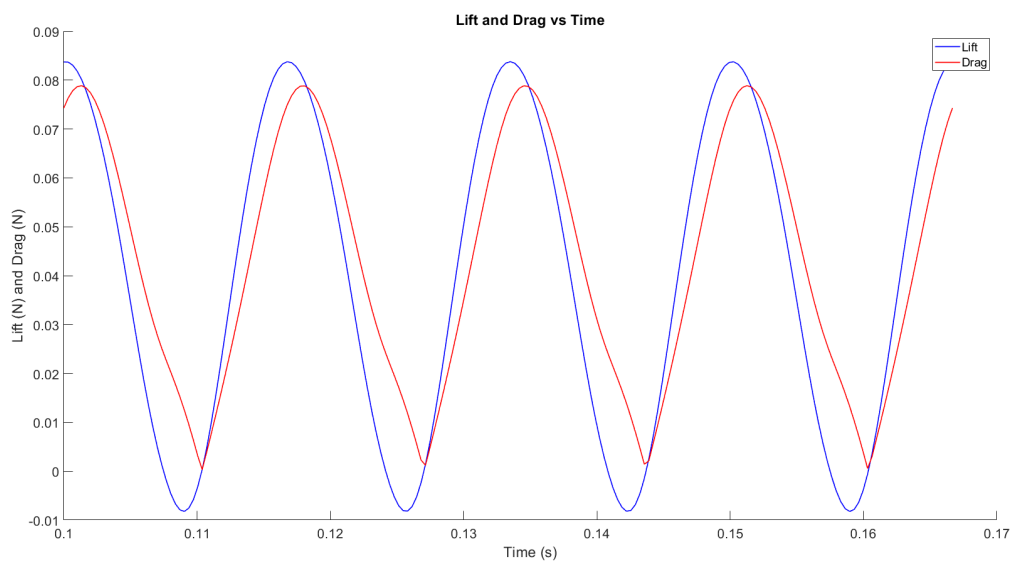


Figure A.6.: Lift and Drag vs Time for additional 3 m/s in inertial -z-axis

Section 7.2 describes that the peak lift/ drag ratio for an additional velocity of 3 m/s generated for the phases of the kinematic cycle depends on the orientation of the velocity with respect to the inertial y-axis and z-axis. This is illustrated in Figures A.7, A.8, A.9, and A.10

A.2. GLOBAL PEAK LIFT AND DRAG GRAPHS

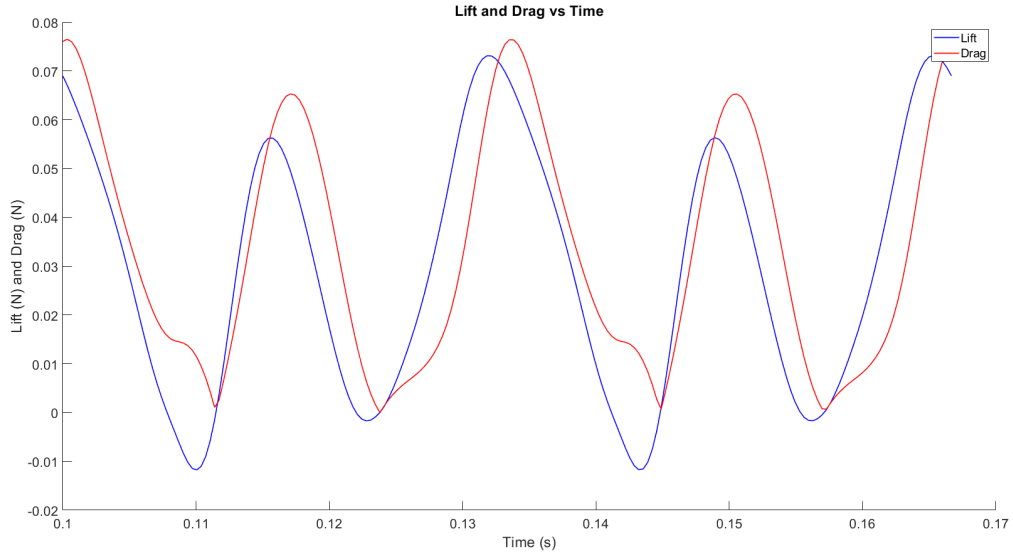


Figure A.7.: Lift and Drag vs Time for additional 3 m/s oriented 25% to the inertial y-axis

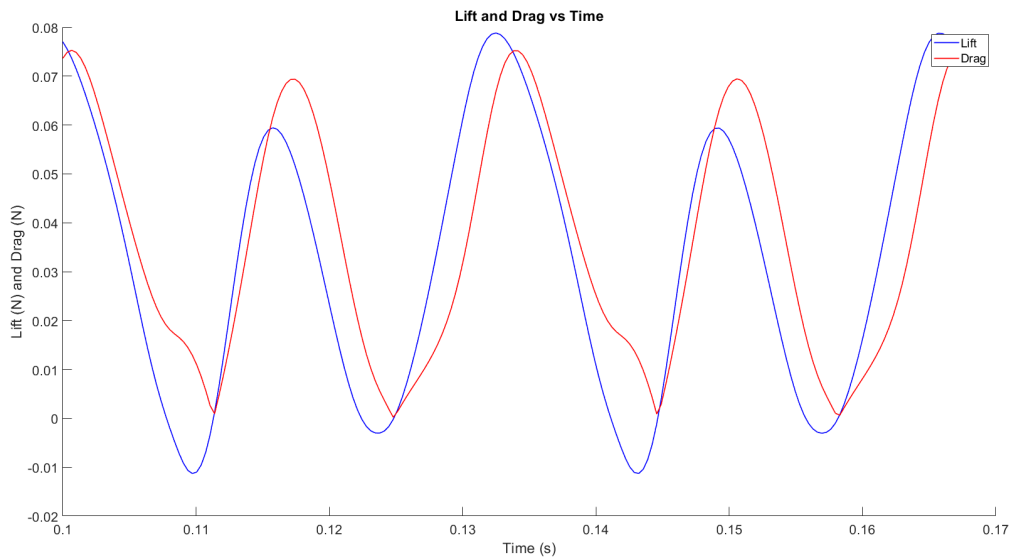


Figure A.8.: Lift and Drag vs Time for additional 3 m/s oriented 37% to the inertial y-axis

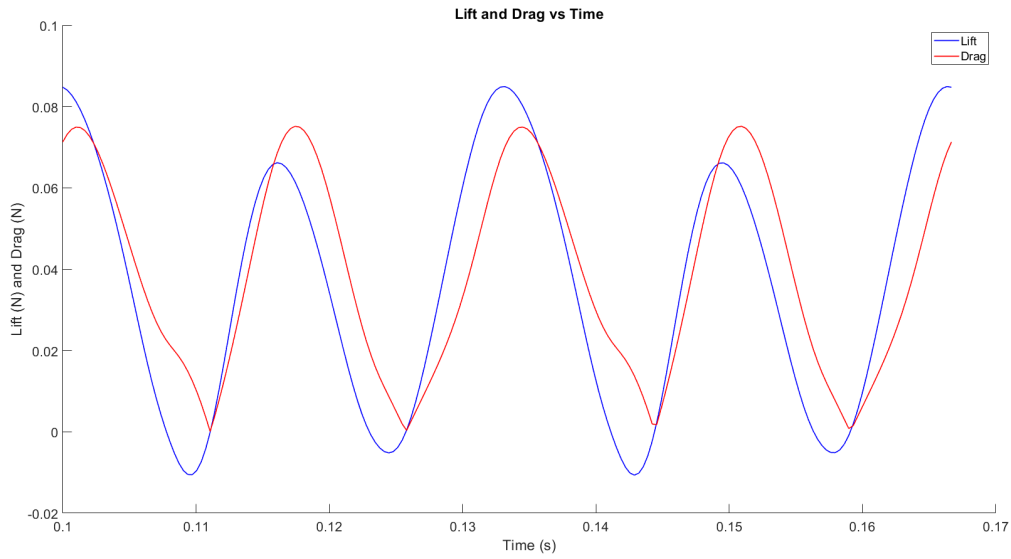


Figure A.9.: Lift and Drag vs Time for additional 3 m/s oriented 53% to the inertial y-axis

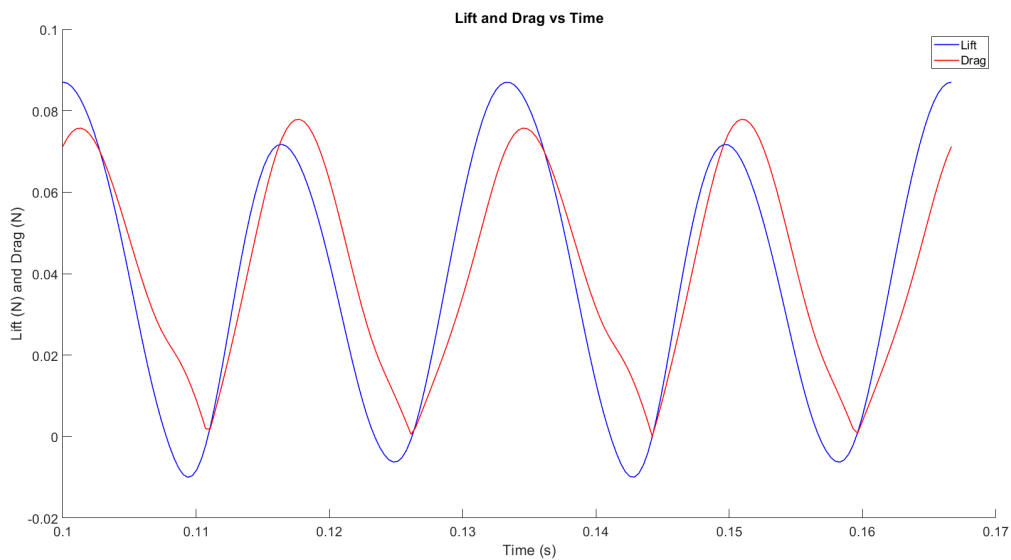


Figure A.10.: Lift and Drag vs Time for additional 3 m/s oriented 65% to the inertial y-axis

### A.3. Passive pitching motion variation graphs

Section 7.3 describes that the increase in the magnitude of additional velocity in the inertial y-axis increases the effect of temporary stalling observed in the passive pitching motion angles. Figure A.11 illustrate that effect.

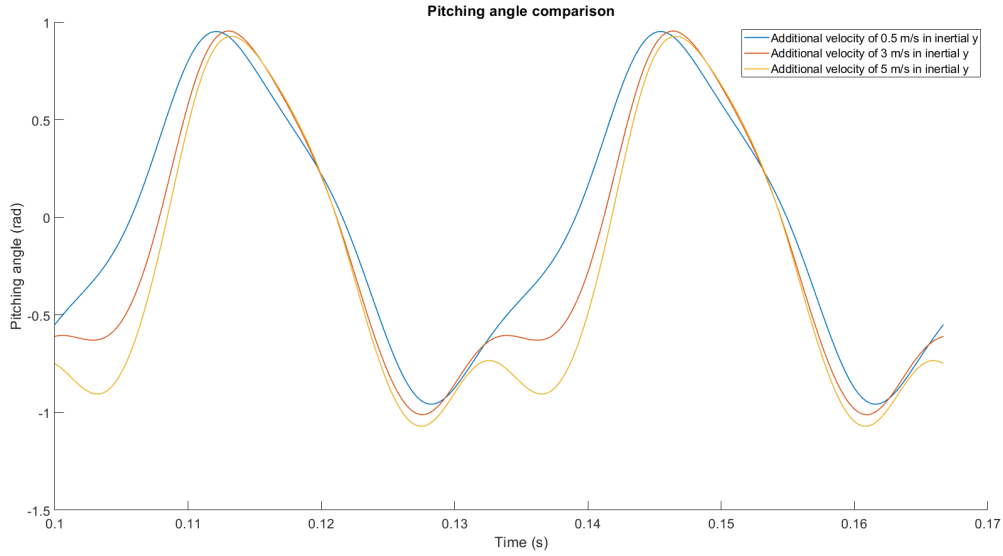


Figure A.11.: Pitching angle comparison for increasing additional velocity in inertial y-axis

Figure A.12 represents the pitching angle computed for the same additional velocity of 3 m/s oriented to have components in both the inertial y-axis and z-axis.

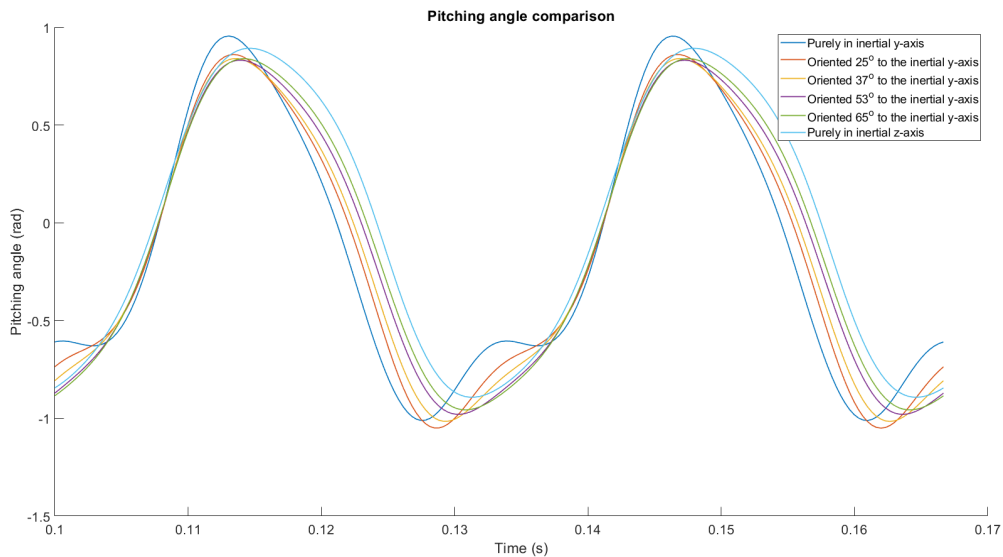


Figure A.12.: Pitching angle comparison for various orientations of 3 m/s additional velocity in inertial y-axis

### A.4. Influence of elastic hinge stiffness graphs

Section 7.4 states that even for increasing magnitudes of additional velocity, the significance of the influence of the additional velocity on the temporary stalling of pitching angle is higher for higher elastic hinge stiffness values. Figures A.13, A.14 and A.15 illustrate the above-mentioned observation, where the additional velocity of 5 m/s in the inertial y-axis is considered.

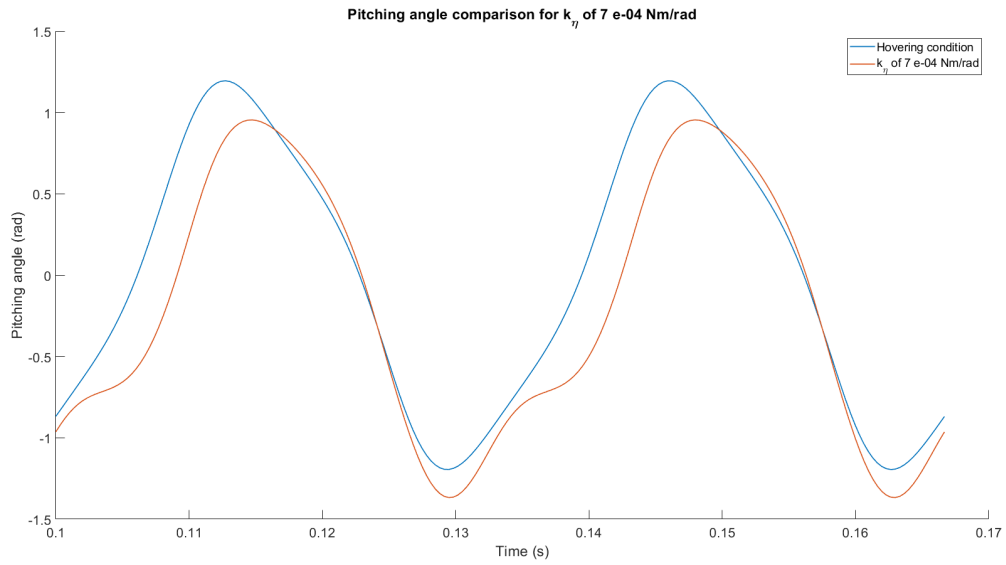


Figure A.13.: Pitching angle comparison for  $k_\eta$  of 7 e-04 Nm/rad for 5 m/s in inertial y-axis

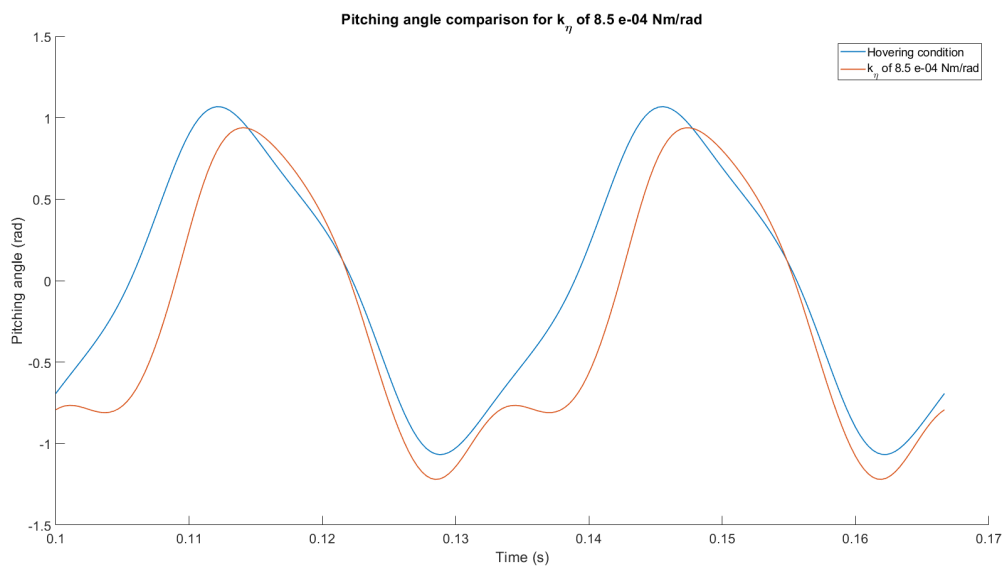


Figure A.14.: Pitching angle comparison for  $k_\eta$  of 8.5 e-04 Nm/rad for 5 m/s in inertial y-axis

## A.5. INFLUENCE OF FLAPPING FREQUENCY GRAPHS

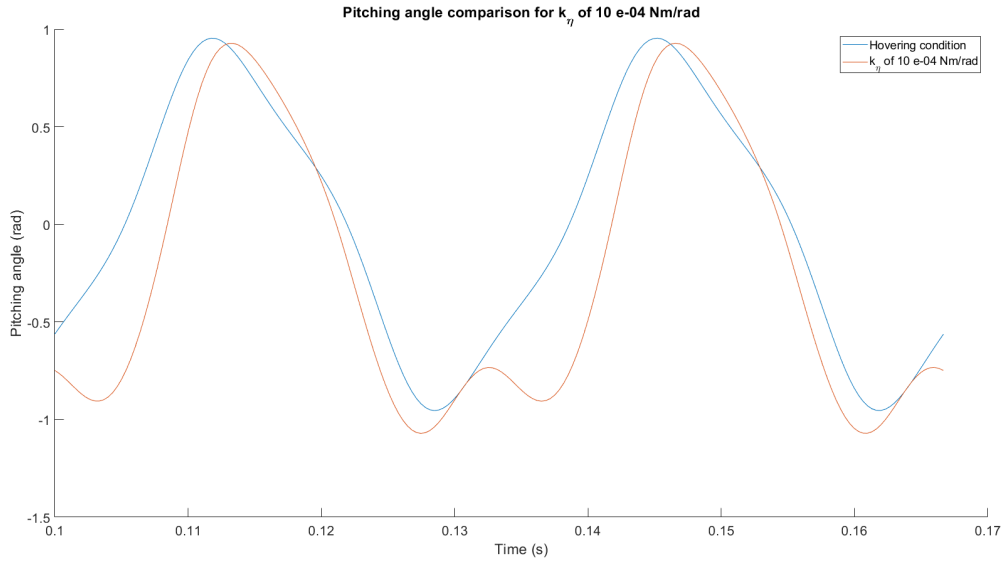


Figure A.15.: Pitching angle comparison for  $k_\eta$  of  $10 \text{ e-}04 \text{ Nm/rad}$  for  $5 \text{ m/s}$  in inertial y-axis

### A.5. Influence of flapping frequency graphs

The graphs illustrated in this Section explain the influence of the flapping frequency on the computed aerodynamic drag. Section 7.5 states that the significance of the influence of additional velocity on the aerodynamic lift and drag increases as the flapping frequency reduces for a given value of elastic hinge stiffness. Figures A.16 and A.17 illustrate this observation for the observed aerodynamic drag for flapping frequencies of  $25 \text{ Hz}$  and  $30 \text{ Hz}$ , and it is clear that the significance of the influence of the same additional velocity is higher when the flapping frequency is lower.

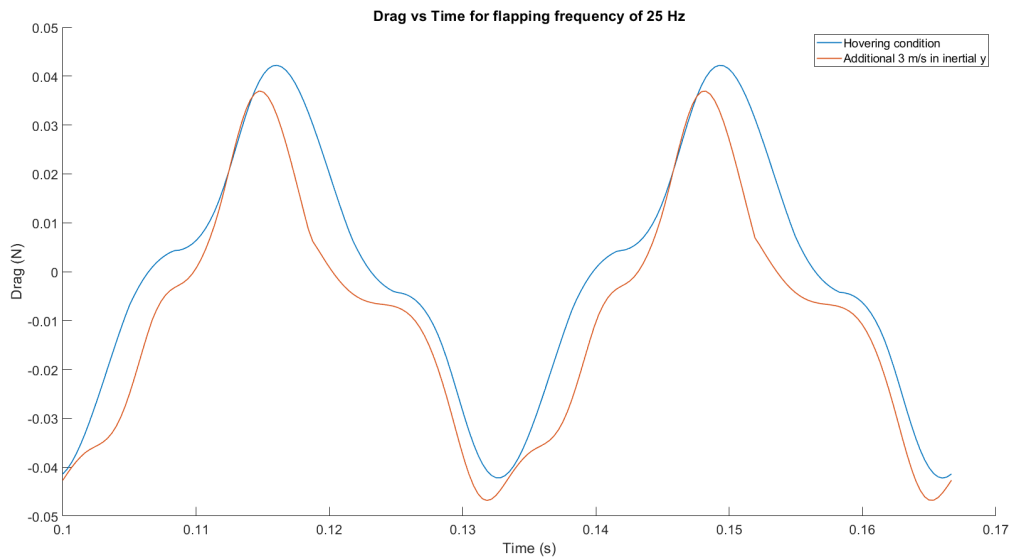


Figure A.16.: Drag vs Time for flapping frequency of  $25 \text{ Hz}$

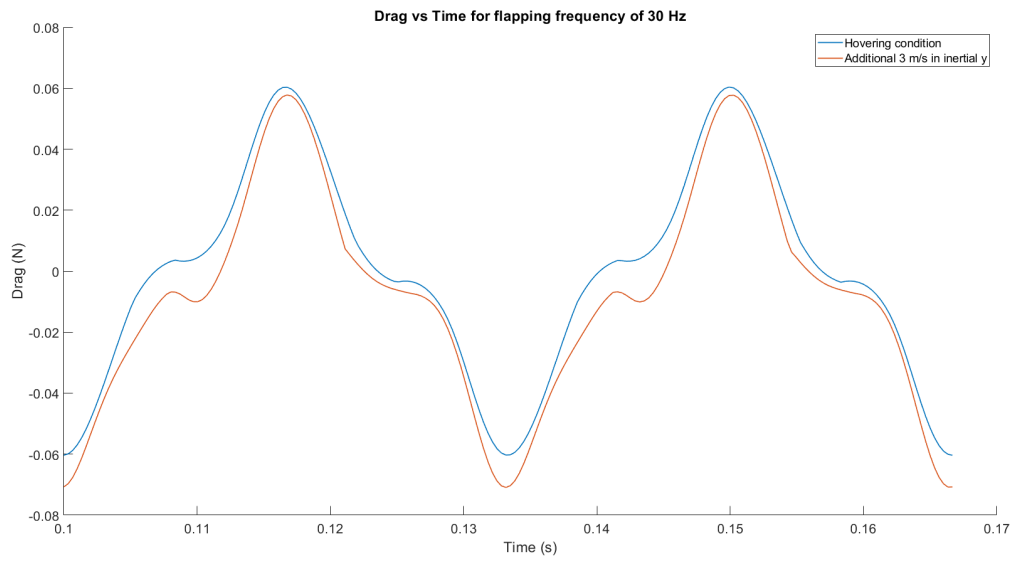


Figure A.17.: Drag vs Time for flapping frequency of 30 Hz

# Bibliography

- [1] Qi Wang. Modeling, design and optimization of flapping wings for efficient hovering flight. 2017.
- [2] C.T. Bolsman. Flapping wing actuation using resonant compliant mechanisms: An insect-inspired design. 2010.
- [3] W. Veerhoek S.P. Aarts B.L. van Gaalen, H.K. Bijlsma. Out-of-plane motions of insects for fwmav. 2014.
- [4] John P Whitney and Robert J Wood. Aeromechanics of passive rotation in flapping flight. *Journal of fluid mechanics*, 660:197–220, 2010.
- [5] Torkel Weis-Fogh. Energetics of hovering flight in hummingbirds and in drosophila. *Journal of Experimental Biology*, 56(1):79–104, 1972.
- [6] Moh Syaifuddin, Hoon Cheol Park, and Nam Seo Goo. Design and evaluation of a lipca-actuated flapping device. *Smart Materials and Structures*, 15(5):1225, 2006.
- [7] Robert J Wood. Liftoff of a 60mg flapping-wing mav. In *2007 IEEE/RSJ International Conference on Intelligent Robots and Systems*, pages 1889–1894. IEEE, 2007.
- [8] Matthew Keennon and Joel Grasmeyer. Development of two mavs and vision of the future of mav design. In *AIAA International Air and Space Symposium and Exposition: The Next 100 Years*, page 2901, 2003.
- [9] Adam Cox, Daniel Monopoli, Dragan Cveticanin, Michael Goldfarb, and Ephrahim Garcia. The development of elastodynamic components for piezoelectrically actuated flapping micro-air vehicles. *Journal of Intelligent Material Systems and Structures*, 13(9):611–615, 2002.
- [10] Hugo Jacobus Peters. A controllability approach for resonant compliant systems: applied to a flapping wing micro air vehicle. 2016.
- [11] R. Diekerhof. Resonating structures with flapping wings: Numerical modelling and validation. 2016.
- [12] A Roland Ennos. The kinematics and aerodynamics of the free flight of some diptera. *Journal of Experimental Biology*, 142(1):49–85, 1989.
- [13] Attila J Bergou, Sheng Xu, and Z Jane Wang. Passive wing pitch reversal in insect flight. *Journal of Fluid Mechanics*, 591:321–337, 2007.
- [14] Robert T Jones. The unsteady lift of a wing of finite aspect ratio. Technical report, 1940.
- [15] Jong-seob Han, Jae-Hung Han, and Jo Won Chang. Effects of advance ratios on the aerodynamic characteristics of an insect wing in forward flight. In *AIAA Atmospheric Flight Mechanics Conference*, page 0018, 2016.
- [16] K Mazaheri and A Ebrahimi. Experimental investigation on aerodynamic performance of a flapping wing vehicle in forward flight. *Journal of Fluids and Structures*, 27(4):586–595, 2011.
- [17] A Muniappan, V Duriyanandhan, and V Baskar. Lift characteristics of flapping wing micro-air vehicle (mav). In *AIAA 3rd "Unmanned Unlimited" Technical Conference, Workshop and Exhibit*, page 6331, 2004.
- [18] Jong-Seob Han, Jo Won Chang, and Jae-Hung Han. An aerodynamic model for insect flapping wings in forward flight. *Bioinspiration & biomimetics*, 12(3):036004, 2017.
- [19] William B Dickson and Michael H Dickinson. The effect of advance ratio on the aerodynamics of revolving wings. *Journal of Experimental Biology*, 207(24):4269–4281, 2004.

## Bibliography

- [20] William Dickson, Andrew Straw, Christian Poelma, and Michael Dickinson. An integrative model of insect flight control. In *44th AIAA Aerospace Sciences Meeting and Exhibit*, page 34, 2006.
- [21] Jong-Seob Han, Joong-Kwan Kim, Jo Won Chang, and Jae-Hung Han. An improved quasi-steady aerodynamic model for insect wings that considers movement of the center of pressure. *Bioinspiration & biomimetics*, 10(4):046014, 2015.
- [22] Haithem E Taha, Muhammad R Hajj, and Philip S Beran. State-space representation of the unsteady aerodynamics of flapping flight. *Aerospace Science and Technology*, 34:1–11, 2014.
- [23] Sanjay P Sane and Michael H Dickinson. The aerodynamic effects of wing rotation and a revised quasi-steady model of flapping flight. *Journal of experimental biology*, 205(8):1087–1096, 2002.
- [24] AHM Faisal and Antonino Filippone. Aerodynamic model for insect flapping wings with induced flow effect. *Journal of Aircraft*, 53(3):701–712, 2016.